UNIVERSIDADE ESTADUAL DE CAMPINAS
Faculdade de Engenharia Mecânica e Instituto De Geociências

ELOISE CRISTINA SANTOS

Classification of fault connectivity zones in pre-salt reservoirs, Santos Basin

Classificação de zonas de conectividade de falhas nos reservatórios do pré-sal, Bacia de Santos

CAMPINAS
2025

ELOISE CRISTINA SANTOS

Classification of fault connectivity zones in pre-salt reservoir, Santos Basin

Classificação de zonas de conectividade de falhas nos reservatórios do pré-sal, Bacia de Santos

Dissertation presented to the School of Mechanical Engineering andd Institute of Geosciences of the University of Campinas in partial fulfillment of the requirements for the degree of Master in Petroleum Science and Engineering, in the area of Reservoirs and Management.

Dissertação apresentada à Faculdade de Engenharia Mecânica e Instituto de Geociências da Universidade Estadual de Campinas como parte dos requisitos exigidos para a obtenção do título de Mestra em Ciências e Engenharia de Petróleo, na área de Reservatórios e Gestão.

Orientador: Prof. Dr. Alexandre Campane Vidal

ESTE TRABALHO CORRESPONDE À VERSÃO FINAL DA DISSERTAÇÃO DEFENDIDA PELA ALUNA ELOISE CRISTINA SANTOS, E ORIENTADA PELO PROF. DR. ALEXANDRE CAMPANE VIDAL

CAMPINAS
2025

Ficha catalográfica
Universidade Estadual de Campinas (UNICAMP)
Biblioteca da Área de Engenharia e Arquitetura
Vanessa Evelyn Costa - CRB 8/8295

	Santos, Eloise Cristina, 1996-
Sa59c	Classification of fault connectivity zones in pre-salt reservoirs, Santos Basin / Eloise Cristina Santos. – Campinas, SP : [s.n.], 2025. Orientador: Alexandre Campane Vidal. Dissertação (mestrado) – Universidade Estadual de Campinas (UNICAMP), Faculdade de Engenharia Mecânica. Em regime multiunidades com: Instituto de Geociências. 1. Modelagem geológica. 2. Reservatórios (Carbonáticos). 3. Reservatórios - Fratura. 4. Falhas (Geologia). 5. Pré-sal - Brasil. 6. Reservatórios - Bacia de Santos. 7. Modelagem tridimensional. I. Vidal, Alexandre Campane, 1969-. II. Universidade Estadual de Campinas (UNICAMP). Faculdade de Engenharia Mecânica. III. Título.

Informações complementares

Título em outro idioma: Classificação de zonas de conectividade de falhas nos reservatórios do pré-sal, Bacia de Santos
Palavras-chave em inglês:
Geological modeling
Reservoirs (Carbonates)
Reservoirs - Fractured
Faults (Geology)
Pre-salt – Brazil
Reservoirs - Santos Basin
Three-dimensional modeling
Área de concentração: Reservatórios e Gestão
Titulação: Mestra em Ciências e Engenharia de Petróleo
Banca examinadora:
Alexandre Campane Vidal [Orientador]
Ulisses Miguel da Costa Correia
Gerardo Gaitan
Data de defesa: 27-02-2025
Programa de Pós-Graduação: Ciências e Engenharia de Petróleo

Objetivos de Desenvolvimento Sustentável (ODS)
Não se aplica

Identificação e informações acadêmicas do(a) aluno(a)
- ORCID do autor: https://orcid.org/0009-0005-5240-7667
- Currículo Lattes do autor: https://lattes.cnpq.br/4065228715600949

Prof. Dr. Alexandre Campane Vidal, Presidente
Departamento de Geologia e Recursos Naturais / Instituto de Geociências / Unicamp

Dr. Ulisses Miguel da Costa Correia
CGG do Brasil Participações

Dr.Gerardo Gaitan
S&P Global

A Ata de Defesa com as respectivas assinaturas dos membros encontra-se no SIGA/Sistema de Fluxo de Dissertação/Tese e na Secretaria do Programa da Unidade.

ACKNOWLEDGEMENTS

This work would not have been possible without the support of my family. I am truly grateful to have my mom and dad as my guides, my friends, and my deepest source of inspiration. Many things can be achieved and conquered when the people around you genuinely wish the best for you and themselves. I am very grateful to come from a loving home that was built for my younger sister and me.

I would like to thank my advisor, Prof. Alexandre Vidal, and the entire team of the "Modelagem Geológica de Reservatórios" (MGR) laboratory for their academic, professional, and personal support throughout the two years in which this research was conducted. A special thanks to the co-authors of my articles and project colleagues: Leonardo, Stefanie, Erik, Juan, Marcus Vinicius, Leticia, Oton, and Michelle, for sharing knowledge, collaboration, and continuous encouragement.

This research was financially carried out in association with the ongoing R&D project registered as ANP n23259-5, “Modelagem e Simulação Avançada de injeção de água, injeção alternada água-gás, injeção de espumas em reservatórios fraturados e carstificados no pré-sal (SIMFRAC2)”, sponsored by Shell Brasil Petróleo Ltda under the ANP R&D levy as “Compromisso de Investimentos com Pesquisa e Desenvolvimento”. Special thanks are given to the Centro de Estudos de Energia e Petróleo (CEPETRO) at the Universidade Estadual de Campinas (UNICAMP) for their support throughout this research.

I also thank ANP for providing research data, as well as Geoactive, Eliis, Emerson, and SLB for providing the academic licenses of Interactive Petrophysics, PaleoScan, RMS, Petrel, and Techlog, respectively.

RESUMO

Compreender a conectividade das falhas em reservatórios carbonáticos fraturados é fundamental para modelar com precisão o fluxo de fluidos e a compartimentalização deste reservatório. A Formação Barra Velha, localizada no pré-sal da Bacia de Santos, apresenta redes complexas de falhas e fraturas, influenciadas pela evolução tectônica e por processos hidrotermais. Modelos tradicionais frequentemente simplificam as interações entre falhas, resultando em incertezas na previsão do comportamento do reservatório. O principal objetivo deste estudo é classificar e analisar os padrões de conectividade das falhas, integrando interpretação sísmica, análise estrutural e topologia de falhas. Utilizando um volume sísmico 3D, as falhas foram interpretadas, classificadas e analisadas para definir zonas de conectividade. Foi aplicada a topologia para quantificar as interações entre as falhas, categorizando-as com base na conectividade de nós e ramos. O estudo identificou quatro principais tipos de conectividade de falhas: *splay, linkage, relay-ramp* e *radial*. Os resultados mostram que a conectividade do tipo *splay* melhora as conexões laterais entre falhas, enquanto a conectividade *linkage* associa-se com crescimento e o tamanho das falhas. A conectividade *relay-ramp* facilita caminhos verticais para o fluxo de fluidos, e a conectividade *radial*, associada à atividade hidrotermal, apresenta um padrão distinto que influenciou a formação dos montes carbonáticos locais. Um modelo 3D de conectividade de falhas foi desenvolvido, demonstrando que as avaliações convencionais de falhas em 2D podem subestimar o papel da conectividade na continuidade vertical e lateral do reservatório. A evolução tectônica da área de estudo desempenhou um papel crucial na configuração da conectividade das falhas. A transição do rifteamento inicial para a reativação e inversão tectônica influenciou a segmentação e a conexão das falhas, modificando a compartimentalização do reservatório ao longo do tempo. O estudo conclui que a integração da topologia das falhas e modelagem estrutural 3D oferecem uma metodologia robusta para aprimorar estratégias de gerenciamento de reservatórios. Ao identificar zonas de alta conectividade, essa abordagem permite uma modelagem e gridagem do reservatório mais precisas, especialmente em regiões com heterogeneidades significativas, que exigem discretização detalhada. Os próximos passos incluem aplicar a delimitação das zonas de conectividade ao grid do reservatório, comparando os resultados com modelos tradicionais. A simulação de reservatório poderá validar os achados com dados de produção e comportamento dinâmico dos fluidos.

Palavras-Chave: Conectividade de falhas, Modelagem de reservatórios, Carbonatos do Pré-Sal, Análise Estrutural 3D, Bacia de Santos, Reservatórios Naturalmente Fraturados.

ABSTRACT

Understanding fault connectivity in fractured carbonate reservoirs is essential for accurately modeling fluid flow and reservoir compartmentalization. The Barra Velha Formation, located in the pre-salt of the Santos Basin, features a complex network of faults and fractures that are influenced by tectonic evolution and hydrothermal processes. Traditional reservoir models often oversimplify fault interactions, leading to uncertainties in predicting reservoir behavior. The main objective of this study is to classify and analyze fault connectivity patterns, integrating seismic interpretation, structural analysis, and topological network modeling. Using a 3D seismic volume, fault networks were interpreted, classified, and analyzed to define connectivity zones. A topological framework was applied to quantify fault interactions, categorizing faults based on node and branch connectivity. The study identified four main connectivity types: splay, linkage, relay-ramp, and radial. The results show that splay connectivity enhances lateral fault connections, linkage connectivity influences fault growth and size, relay-ramp connectivity facilitates vertical fluid pathways, and radial connectivity, associated with hydrothermal activity, exhibits a distinct radial pattern that influenced the formation of local carbonate mounds. A 3D fault connectivity model was developed, demonstrating that conventional 2D fault assessments may underestimate the role of fault connectivity in the vertical and lateral continuity of the reservoir. The tectonic evolution of the study area played a crucial role in shaping fault connectivity. The transition from early rifting to strike-slip reactivation and inversion influenced the segmentation and linkage of faults, modifying reservoir compartmentalization over time. The study concludes that integrating fault topology, seismic interpretation, and 3D structural modeling offers a robust methodology for enhancing reservoir management strategies. By identifying high-connectivity zones, this approach ensures more accurate reservoir modeling and gridding, particularly in regions with significant fault-related heterogeneities that require detailed discretization. Future steps include applying the fault connectivity zone delimitation to reservoir gridding and comparing the results with those obtained from traditional modeling techniques. Reservoir simulation could validate the findings by comparing them with field production data and dynamic fluid behavior.

Key Word: Fault connectivity, Reservoir modeling, Pre-Salt Carbonates, 3D Structural Analysis, Santos Basin, Natural Fractured Reservoirs.

LIST OF FIGURES

TABLE OF CONTENTS

1. INTRODUCTION

The 3D geological modeling of reservoirs, such as those in the pre-salt layer, presents significant challenges in accurately representing the porosity and permeability of the matrix, fractures, and vugs. Studies indicate that pre-salt carbonates possess fracture porosity and permeability that significantly exceed those of the surrounding matrix, highlighting the importance of developing a robust fracture model (Correa et al., 2019; Fernández-Ibáñez et al., 2022).

However, constructing models such as the Discrete Fracture Network (DFN) and Dual-Porosity Dual-Permeability (DPDK) is often hindered by the limited availability and spatial distribution of well data. These data are crucial for enabling multi-scale reservoir analysis and providing the necessary inputs for modeling and the statistical distribution of model attributes (Cherpeau et al., 2010).

Geology is inherently an interpretative science, and even high-resolution 3D datasets cannot entirely eliminate uncertainties. In practice, modeling is often constrained by the scarcity and incompleteness of well data within the study area. Frequently, the spatial distribution of data is not representative, which increases model uncertainty and leads to reservoir management decisions that may lack precision due to time constraints (Deutsch, 2005; Cherpeau et al., 2010). Seismic surveys, despite operating at a much larger scale than methods such as borehole imaging (BHI), core analysis, and plug studies, generally provide broader coverage of the area of interest.

Although seismic resolution and noise limit interpretation, fault throw mapping is a routine modeling activity that provides valuable insights into the geometry, length, strike, and dip of key structures, which may act as hydrocarbon traps or fluid flow pathways (Yang & Eacmen, 2003; Fernández-Ibáñez et al., 2022). Another limitation of models like DFN is that populating the grid with well data can make the model computationally demanding, thereby complicating the simulation process. (Richard et al., 2015; Karatalov et al., 2017).

To enhance geological representation and address challenges in fault modeling, we propose a method that uses the topology of fault networks to define connectivity zones. This approach complements traditional 2D reservoir studies, which often emphasize horizontal fault distribution, by introducing a 3D connectivity model that captures vertical and horizontal interconnections.

The proposed method of this study integrates topological analysis, structural characterization, and fault growth theories to understand fault interactions better while minimizing reliance on subsismic data. This approach enables a more precise identification of areas where Discrete Fracture Network (DFN) modeling should be applied, thereby optimizing efficiency and enhancing geological accuracy. By capturing the structural complexity of fault networks, the model improves fault connectivity representation, reduces propagation uncertainties, and supports more robust and reliable reservoir modeling.

Specific objectives:

- To interpret four seismic horizons (Itapema, Lower Barra Velha – LBV, Intermediate Barra Velha – IBV, and Upper Barra Velha – UBV) across the reservoir interval.
- To classify fault systems (F1–F4) and quantify fault displacement magnitudes and segmentation trends.
- To define and describe connectivity typologies, including splay, linkage, relay-ramp, and radial fault interaction patterns.
- To construct a 3D connectivity model integrating structural interpretation and topological parameters.

1.1. Motivation

Reservoir modelers operate under persistent constraints: the resolution limits of seismic data obscure critical small-scale fractures, while sparse well coverage biases spatial interpretations. These gaps lead to an over-reliance on geostatistical extrapolations, which amplifies uncertainties in fault continuity and hydraulic behavior, thereby directly compromising flow simulations and development decisions.

To address these challenges, our methodology leverages fault topology to identify high-impact connectivity zones, focusing computational effort where fracture complexity dictates flow. By implementing systematic connectivity classification, we reduce interpretation bias and replace geometric assumptions with more accurate representations.

Furthermore, the approach balances geological fidelity with efficiency through targeted Discrete Fracture Network (DFN) application, avoiding uniform upscaling that obscures critical heterogeneities. This integrated strategy explicitly links topological analysis to computational optimization and uncertainty reduction, creating a structured framework that minimizes redundant data limitations while enhancing predictive reliability for reservoir management.

Given these challenges, the motivation behind this work is to develop a structured approach to fault connectivity modeling that:

- Maximizes the use of available data by integrating fault topology and connectivity analysis rather than relying solely on direct geometric interpretations.
- Reduces uncertainty by classifying and delineating connectivity zones, helping to refine where higher-detail modeling is needed and where a simplified representation is sufficient.
- Optimizes computational efficiency, ensuring that reservoir models remain geologically meaningful without exceeding computational limitations.

1.2. Key questions and study organization

This study addresses three fundamental questions regarding fault connectivity and reservoir compartmentalization in the Barra Velha Formation:

1. What are the primary connectivity patterns, and how do they influence horizontal and vertical connections that might impact potential fluid pathways?

2. How do different fault sets interact within the reservoir to control fault connections and structural compartmentalization in the Barra Velha Formation?

3. How can connectivity zones be integrated into reservoir modeling to improve geological representation and simulation accuracy?

To systematically answer these questions, the research was structured into key sections, each building upon the previous to develop a comprehensive understanding of fault connectivity and its implications for reservoir modeling.

- **Chapter 1: Introduction** – Presents the research motivation, objectives, and key questions, outlining the relevance of fault connectivity in reservoir characterization.

- **Chapter 2: Theoretical Background** – To understand the importance and challenges of reservoir characterization and modeling, it is essential to consider the historical evolution of the techniques applied. Today, various approaches to reservoir characterization and modeling are available, each with its own advantages and limitations, which should be carefully aligned with the study's objectives.

- **Chapter 3: Geological and Tectonic Framework** – Provides an overview of the Santos Basin and the Barra Velha reservoir, discussing the regional tectonic evolution and faulting history to establish the geological context.

- **Chapter 4: Methodology** – Details the workflow used to classify faults, analyze connectivity, and develop the 3D connectivity model. The integration of structural mapping, fault topology, and simulation grid discretization directly addresses the need for improving geological representation.

- **Chapter 5: Results** – Presents the fault classification, displacement analysis, and connectivity patterns, providing key insights into the structural configuration of the study area. The identification of splay, linkage, relay-ramp, and radial connectivity types clarifies how different fault sets interact and control reservoir compartmentalization, while also introducing a new consideration for classifying fault damage zones.

- **Chapter 6: Discussion** – Examines the structural evolution and its impact on reservoir architecture. The analysis of connectivity dynamics provides insights into horizontal and vertical connections and their implications for fluid pathways.

- **Chapter 7: Conclusion and Future Work** – Summarizes the main findings, emphasizing how connectivity zones enhance reservoir modeling and simulation accuracy.

2. THEORETICAL BACKGROUND

This chapter provides an integrated overview of geological reservoir characterization and modeling, highlighting historical advances from early empirical relationships to modern techniques. It discusses the importance of fractures and faults in controlling fluid flow, explains both explicit and implicit modeling approaches, and details the anatomy, geometry, and relationships of faults. Together, these concepts form the foundation for building realistic and practical reservoir models that capture structural complexity and guide production strategies.

2.1. Reservoir characterization and modeling

Reservoir geological characterization and modeling play a fundamental role in hydrocarbon exploration and production, providing a three-dimensional representation of the subsurface to guide decision-making in field development and reservoir management. By integrating geological, geophysical, petrophysical, and engineering data, these models allow for a better understanding of reservoir heterogeneity, fluid distribution, and production potential (Surguchev et al., 1992; Kompanik et al., 1993; Tariq et al., 2012; Treffeisen & Henk, 2019).

Historically, studies in petroleum geology began in the 1940s, with foundational contributions, such as those of Archie (1942), who introduced the empirical relationship now known as Archie’s Law, enabling porosity estimates from well resistivity logs. During the 1950s and 1960s, the foundations of geostatistics emerged, notably with the introduction of kriging by Krige (1951) and the development of geostatistical theory and the variogram by Matheron (1963). In parallel, reservoir studies advanced through the integration of geological, geophysical, and well-logging data, culminating in the first two-dimensional (2D) descriptions of reservoir heterogeneity (Jahns, 1966; Ringrose & Bentley, 2021).

The 1970s brought significant advancements in geophysical applications and the use of seismic attributes for reservoir characterization. Gardner and Gregory (1974) proposed an empirical relationship between seismic velocity and rock density, while Taner and Sheriff (1977) introduced the concept of complex seismic trace analysis. Lindseth (1979) introduced the concept of recursive inversion, which enables the automated generation of stratigraphic sections from seismic transit-time data.

The 1980s and 1990s marked significant advancements in geostatistical modeling, including the introduction of the corner-point grid (Wadsley, 1980; Ding & Lemonnier, 1995), multiple-point simulation techniques (Guardiano & Srivastava, 1993), and transition-probability-based indicator geostatistics (Carle & Fogg, 1996). The release of Geostatistical Software Library and User's Guide **(**GSLIB) by Deutsch and Journel (1998) further standardized geostatistical workflows in reservoir characterization (Bjørlykke, 2015; Ringrose & Bentley, 2021).

Over the years, advancements in reservoir modeling techniques have significantly improved accuracy and efficiency, notably through the application of upscaling and downscaling methods, as well as the integration of artificial intelligence and machine learning approaches. However, balancing geological detail with computational efficiency remains a major challenge in reservoir modeling.

High-resolution models, while providing detailed and accurate representations of reservoirs, can be computationally prohibitive for fluid flow simulations. To overcome this issue, upscaling techniques are employed to simplify fine-scale geological features while preserving essential reservoir characteristics (**Figure 1**). These approaches include arithmetic, harmonic, and geometric averaging methods for estimating permeability and porosity, as well as flow-based upscaling, which assigns equivalent reservoir properties to maintain accurate macroscopic flow behavior. Additionally, representative volume methods are used to determine the minimum volume required to capture geological heterogeneity effectively while ensuring computational feasibility (Maschio & Schiozer, 2003; Qi & Hesketh, 2005; Zhang et al., 2005; Santos et al., 2022).

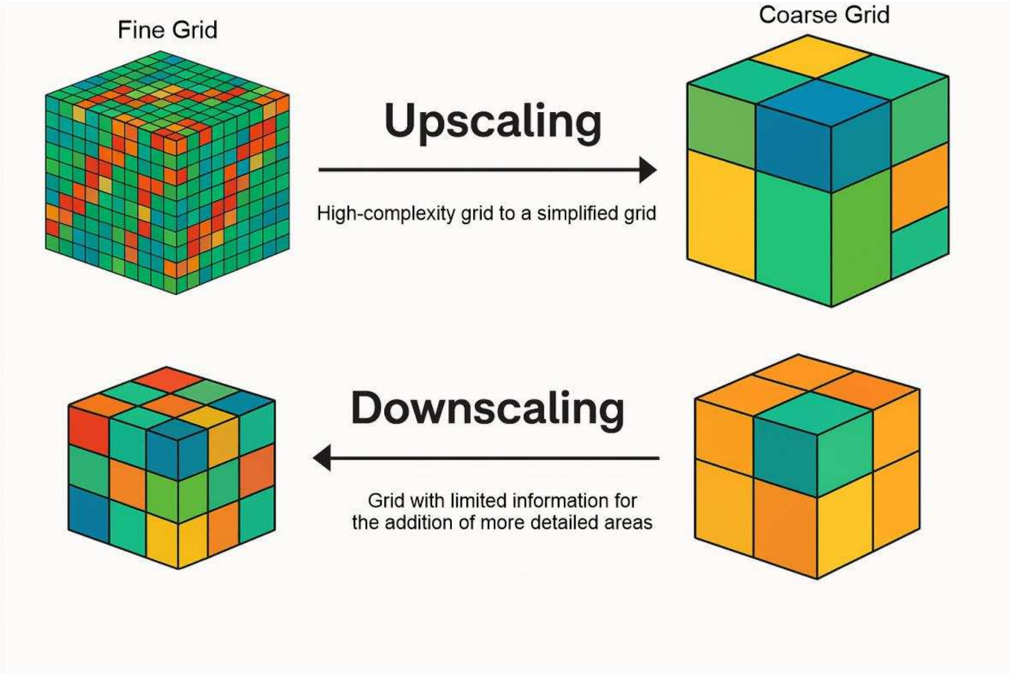

Figure 1: Schematic representation of upscaling and downscaling processes. Upscaling reduces fine-grid complexity into coarse models for computational efficiency, while downscaling enhances coarse grids with finer geological detail.

Conversely, downscaling methods refine coarse reservoir models by introducing finer geological details, enhancing the accuracy of predictions in localized areas. This process is crucial for modeling fractured reservoirs, thinly bedded formations, and other highly heterogeneous environments. Techniques such as geostatistical interpolation, including kriging and stochastic simulations, allow for the redistribution of properties at finer scales. Seismic attribute analysis provides additional refinement by integrating high-resolution seismic data to enhance geological features. Hybrid approaches that combine deterministic and stochastic methods are also commonly used to represent heterogeneity more effectively in localized reservoir regions (Babaei & King, 2012; Nunna & King, 2017).

Recent advances in artificial intelligence and machine learning have revolutionized reservoir geological modeling by enabling faster and more accurate characterization of reservoirs. AI-driven models enhance prediction capabilities, optimize simulation efficiency, and significantly reduce uncertainty. (Hong et al., 2020; Tang et al., 2020; Kuang et al., 2021).

In seismic interpretation, deep learning models have been utilized to extract geological features, thereby enhancing stratigraphic and structural interpretations. Machine learning algorithms have also proven effective in predicting key reservoir properties such as porosity, permeability, and saturation by analyzing well logs and core data. Additionally, automated history matching, which traditionally requires extensive manual calibration, has benefited from AI optimization techniques that adjust reservoir parameters to align with historical production data. These innovations accelerate the modeling process while improving accuracy (H. Li & Misra, 2020; Tariq et al., 2021; J. X. Li et al., 2024;)

2.2. Natural fractured reservoir modeling

Fractured reservoirs are those in which fractures have a significant influence on fluid circulation. In many instances, these fractures dominate fluid flow, particularly when the host rock matrix exhibits low permeability. Often initially considered negligible, fractures become evident throughout production and subsequently complicate reservoir modeling, as they require methodologies extending beyond traditional sedimentary characterization (Ringrose & Bentley, 2021).

In structural geology, the term "fracture" is broadly applied to any mechanical discontinuity or break within a rock, without necessarily implying significant displacement between adjacent blocks (Twiss & Moores, 1992). Pollard & Aydin (1988) further classify fractures based on their mode of opening, distinguishing Mode I (extension), Mode II (shear), and Mode III (anti-plane shear). Additionally, Scholz (1990) identifies subclasses within fractures, including joints, which are openings without displacement; veins, defined as fractures filled with minerals; and faults, characterized by components of both opening and shear displacement.

Considering that the seismic structures interpreted in this study involve displacement and throw mapping, the fractures analyzed here are classified as faults. Faults entail physical displacement along a fracture surface, typically resulting from shear deformation (Fossen, 2016). Rather than being simple planar features, faults consist of multiple fractures and deformation zones, characterized by an internal compartmentalization into a fault core and a surrounding damage zone, each containing its subordinate structural elements (Caine et al., 1996; Wibberley & Shipton, 2010).

Thus, when modeling naturally fractured reservoirs, it is essential first to develop a robust conceptual model that defines the tectonic context of the study area and classifies the faults and available data. This foundation guides the choice of modeling approach—whether to adopt explicit methods, such as Discrete Fracture Networks (DFNs), or implicit methods, dual porosity/dual permeability (DPDP) models, for example.

Explicit models, particularly Discrete Fracture Networks (DFNs) (**Figure 2**), provide detailed digital representations of actual fractures, explicitly incorporating their geometry, orientation, and spatial extent (Jing & Stephansson, 2007). This method is especially suitable for near-wellbore regions where high-resolution data, such as FMS imaging and core samples, are available. After establishing the static fracture model, specialized simulators are required to simulate fluid flow through these fracture planes accurately (Elmo et al., 2010, 2015; Karatalov et al., 2017; Ringrose & Bentley, 2021).

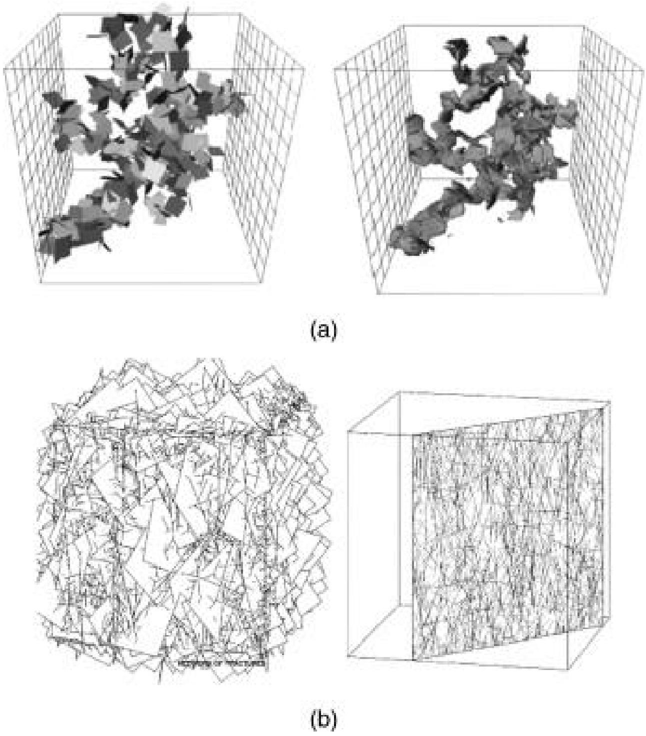

Figure 2: Examples of Discrete Fracture Network (DFN) models. (a) Stochastic realization illustrating a complete 3D fracture network (left) and the resulting connected flow pathways within the network (right). (b) 3D DFN model created from borehole logging data, showing the overall fracture system (left) and fracture traces on a vertical cross-section (right) (from Jing & Stephansson, 2007).

However, DFN models present several significant limitations:

- High computational complexity: Modeling all fractures across an entire reservoir is generally impractical due to computational constraints.
- Forced generalizations: Key properties, such as permeability and aperture, are often assumed to be constant or stochastically distributed, neglecting the logical structural connectivity patterns observed in natural fracture systems.

- Limited maturity of algorithms: Compared to traditional reservoir modeling tools, DFN algorithms are relatively underdeveloped, limiting their ability to capture true geological complexity.
- Questionable utility at large scales: The simplifications required to maintain computational feasibility often reduce the model's value primarily to visualization, offering limited benefit for accurate dynamic predictions.

Consequently, DFN models are best suited for local-scale applications, such as calibration to formation tests or short-range simulations. Results derived from these local-scale analyses, particularly effective permeabilities, can subsequently inform implicit models at broader scales.

An alternative to traditional numerical modeling approaches for naturally fractured reservoirs is implicit fracture modeling, which treats fracture networks as continuous properties across the grid, rather than modeling individual fractures explicitly. This method employs the concept of a Representative Elementary Volume (REV), which captures the averaged density, orientation, and permeability of fracture networks within each grid cell (Lee et al., 1999; Cordero et al., 2019).

Implicit models typically employ dual-porosity (Barenblatt et al., 1960) or dual-permeability (Blaskovich et al., 1983; Hill & Thomas, 1985) simulators, which utilize two overlapping grids: one representing the rock matrix and the other representing fractures (**Figure 3**). A critical parameter in these models is the shape factor (sigma), which governs fluid exchange between the matrix and fracture grids, predominantly driven by capillary flow in the matrix and viscous flow in fractures.

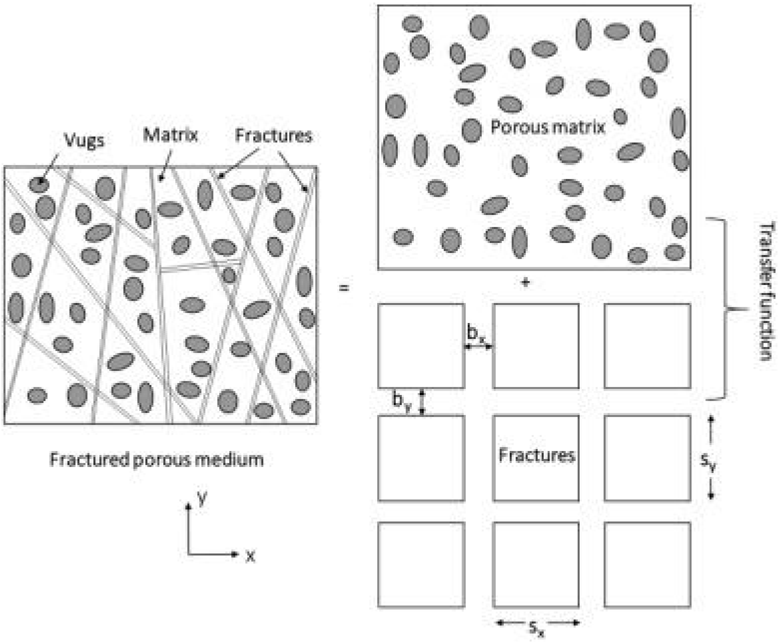

Figure 3: Conceptual representation of a naturally fractured reservoir, illustrating the dual porosity model approach, where the porous matrix and the fracture network are treated as separate but interacting domains. The transfer function represents the exchange of fluid between the matrix blocks and fractures. (from Cordero et al., 2019).

The workflow for implicit modeling involves calibrating parameters such as fracture density, fracture porosity, directional permeability, and associated geometric properties. Initially derived from logs, core analyses, and seismic attributes, these parameters are subsequently refined with dynamic data, including pressure tests, to match actual reservoir behavior more accurately. In contrast to explicit DFN models, implicit models are usually applied at full-field scales.

In summary, explicit DFN models and implicit dual-porosity/dual-permeability approaches each offer unique advantages, making them complementary rather than competing methodologies. DFN models excel in providing detailed, realistic representations of local fracture networks and precise connectivity analysis, making them ideal for near-wellbore studies, albeit with high computational and data requirements. Conversely, implicit models offer a scalable and practical solution suitable for full-field simulations, integrating seamlessly with conventional workflows and production data. However, they sacrifice detailed geometric fidelity and direct connectivity insights. The choice between these methods should ultimately depend on the scale of analysis, data availability, and specific reservoir management objectives.

2.3. Damage zones terminology

A damage zone is a deformed region surrounding a fault, characterized by concentrated stress and strain and composed of internal and subsidiary structures, such as fractures, slip surfaces, and fault rock assemblages (Kim et al., 2003; Fossen, 2010; Choi et al., 2015; Peacock et al., 2017). These zones display distinct fabrics and deformation patterns that differentiate them from the surrounding undeformed rock (Peacock et al., 2016). Structural geology studies often classify damage zones based on fault growth patterns, interactions, and the accommodation of strain and displacement in areas adjacent to and influenced by faults (Wibberley et al., 2008; Wibberley & Shipton, 2010; Choi et al., 2015; Peacock et al., 2017).

Several prominent studies have proposed various classification frameworks. Kim et al. (2003) categorize damage zones based on their position relative to fault segments, identifying three primary types: tip, wall, and linking damage zones. Alternatively, Choi et al. (2015) propose a spatially oriented classification system that focuses on the distribution of cumulative fracture frequency around exposed faults, defining damage zones as along-fault, around-tip, and cross-fault zones. Expanding these frameworks, Peacock et al. (2017) emphasize the kinematic and geometric interactions between faults and address the challenges of limited knowledge regarding the 3D geometries of these structures. Their classification introduces additional categories, including approaching, intersection, fault bend, and distributed damage zones.

Additionally, Nixon et al. (2020) applied topology and graph metrics to describe and quantify the characteristics of fracture networks within damage zones. This approach complements traditional classifications that focus primarily on geometry and architecture by enabling a deeper understanding of the internal connectivity of fracture networks. It enables the objective comparison of fluid flow pathways in low-permeability zones across different scales. The present work will utilize damage zone classifications based on fault interaction and network connectivity to analyze specific structural zones (**Figure 4**).

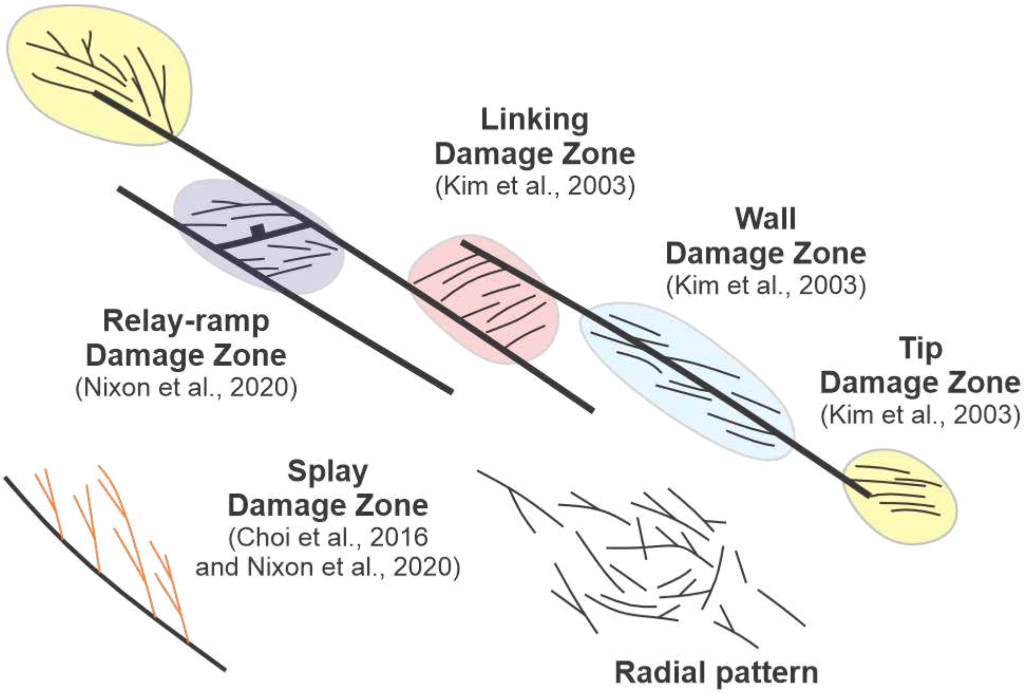

Figure 4: Damage zones terminologies. Linking, wall, and tip damage zones (Kim at. Al, 2003). Relay-ramp damage zone (Nixon et al., 2020). Splay damage zone (Choi et al., 2016, and Nixon et al., 2020). Radial fault pattern.

(i) **Linking fault zones** are structural features formed by secondary deformation between interacting fault segments, enabling displacement and strain transfer (Peacock, 2002; Soliva & Benedicto, 2004; Nixon et al., 2020). These zones arise from stress modifications caused by fault interaction, involving shear, dilation, or contraction depending on slip direction and overlap geometry (Ferrill et al., 1999; Nixon et al., 2014; Peacock et al., 2017)

They often develop at the tips of isolated fault segments, connecting via shear, tearing, or mixed-mode mechanisms (Ferrill et al., 1999; Schlische & Withjack, 2008). This process may involve relay ramps, where displacement transfer occurs through tilting, extension, and breaching by connecting faults (Peacock & Sanderson, 1994; Peacock, 2002). Linking zones commonly exhibit steeper displacement gradients, increased shear stress, and reoriented stress fields, favoring linkage in areas with high overlap-to-separation ratios (Soliva & Benedicto, 2004; Moustafa & Khalil, 2016; Nixon et al., 2020).

(ii) **Splay faults** are secondary structures that branch from a primary fault at an acute angle, often creating a distinctive "Y" shape geometry (Peacock, 2002; Peacock et al., 2017). These faults are crucial in accommodating deformation at the tips of primary faults or along geometric irregularities such as fault tips, transfer zones, or jogs (Scholz et al., 2009; Perrin et al., 2015; Biemiller et al., 2023). The development of splays is closely tied to the interaction between the principal fault and the surrounding regional stress field. Stress concentrations at fault tips can form fractures that grow into cone- or tree-shaped networks (Duffy et al., 2017; Nixon et al., 2020).

(iii) In extensional fault systems, **relay ramps** serve as transfer zones between overlapping fault segments, facilitating displacement and strain transfer (Peacock & Sanderson, 1994; Kim & Sanderson, 2004). They form when initially independent fault segments propagate and interact, creating an overlapping zone. With increased displacement, linking fractures, such as synthetic, antithetic, or oblique-slip faults, develop and may eventually break the ramp, forming a composite fault (Peacock & Sanderson, 1994; Trudgill & Cartwright, 1994; Soliva & Benedicto, 2004; Fossen & Rotevatn, 2015). Remnants of relay ramps often remain as drag folds or fault-bounded blocks. These structures facilitate strain accommodation by transferring displacement, alleviating stress concentrations, and creating smoother displacement profiles. (Peacock & Sanderson, 1994; Henaish & Attwa, 2018).

(iv) **Radial faults** are extensional structures radiating outward from a central point, commonly linked to hydrothermal vents, salt diapirs, or magmatic intrusions (Coleman et al., 2018; Mattos & Alves, 2018). These faults are identifiable on seismic data as linear discontinuities on variance or chaos attribute maps and normal faults on seismic sections (Omosanya et al., 2018). They can be classified based on their origin: roof-stretching faults form near salt-sediment interfaces with limited lateral extent (<200 m) due to diapiric uplift (Coleman et al., 2018); stem-push faults arise from circumferential extension, extending several kilometers with greater height and reach(Rowan et al., 2020); and vent-associated faults develop at hydrothermal vent summits, confined to shallow levels and marked by chaotic or low-amplitude seismic reflectors(Omosanya et al., 2018; Planke et al., 2005).

3. GEOLOGICAL SETTING

The Santos Basin is situated along the southeastern coastal margin of Brazil, covering an area of approximately 350,000 square kilometers. Geologically, it is bounded to the north by the Campos Basin, separated by the Cabo Frio Arc, and to the south by the Florianópolis Structural High, which delineates the boundary with the Pelotas Basin (Moreira et. Al., 2007; Fernandes & Santos, 2017). Its western limit is defined by coastal mountain belts including the Serra do Mar, Maciço Carioca, and Serra da Mantiqueira, while to the east, the basin extends up to the foothills of the São Paulo Plateau (**Figure 5**) (Buckley et al., 2015; Adriano et al., 2022).

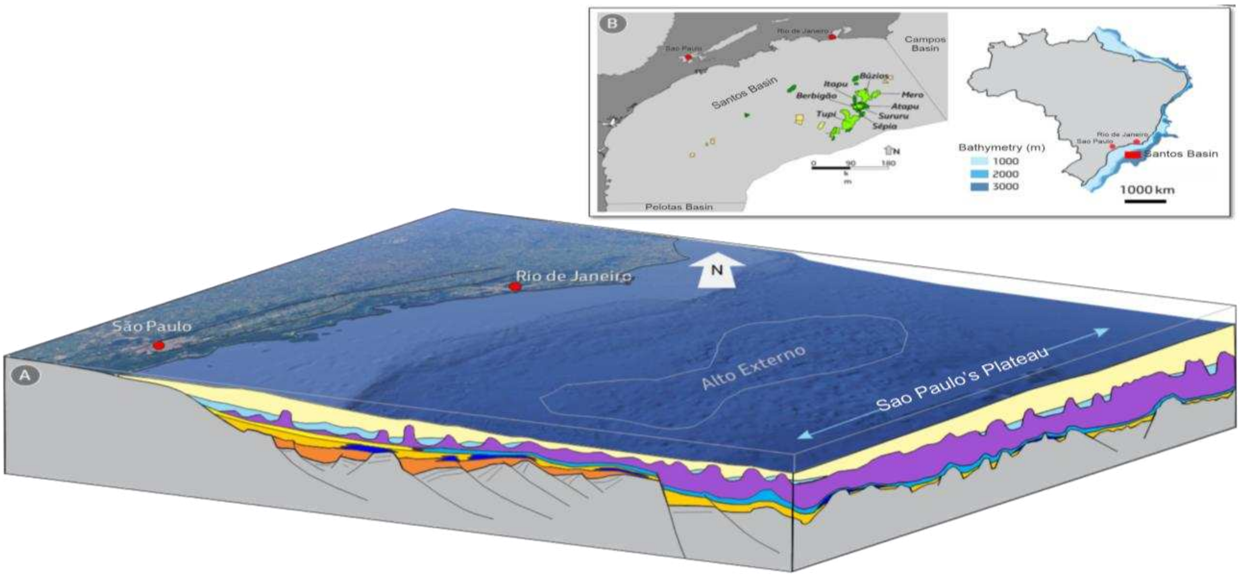

Figure 5: (a)Tectono-stratigraphic framework and structural configuration of the Santos Basin in a regional 3D perspective (b) location map of the Santos Basin with the main pre-salt oil production fields (adapted from Araújo et al. 2024)

The Santos Basin was formed during the Early Cretaceous rifting of West Gondwana and exhibits a complex structural evolution marked by multiple tectonic, sedimentary, and volcanic phases that have significantly influenced its geological architecture (Kiang et al., 1992; Mohriak & Paula, 2005; Stanton et al., 2014).

Several studies have proposed different subdivisions of the tectonic evolution of the Santos Basin. In general, it began with a pre-rift phase, during the initial stages of Gondwana breakup, followed by a rift phase (Moreira et al., 2007), which initiated the deposition of the pre-salt carbonates (Minzoni et al., 2020), forming what is referred to as the Lower Barra Velha Formation (Buckley et al., 2015; Barnett et al., 2018). A third stage, known as the post-rift phase (Moreira et al., 2007) or sag phase (Buckley et al., 2015; Barnett et al., 2018), is characterized by reduced tectonic activity, which led to the deposition of the Upper Barra Velha Formation and the Ariri Formation. Finally, the drift phase (Moreira et al., 2007; Moulin et al., 2013) corresponds to a passive margin setting, during which oceanic crust is established.

In this study, to better characterize the tectonic structures of each stage, we subdivide the evolution into Pre-Rift, Rift Phase I, Rift Phase II, and Post-Rift Phase. The pre-rift phase of the Santos Basin occurred between the Late Jurassic and the earliest Cretaceous (~160–140 Ma) and represents the initial stage of preparation for the breakup of the supercontinent Gondwana. During this period, tectonic processes before the actual rifting established the conditions for future continental fragmentation. The context was marked by the development of paleovalleys and tilting of crustal blocks, resulting from the reactivation of lithospheric weakness zones inherited from Precambrian orogenic cycles.

During the Valanginian–Barremian (~140–130 Ma), Rift Phase I was characterized by intense extensional tectonic activity associated with the continental breakup during the Early Cretaceous. This phase resulted in the formation of N-NE to NW-oriented normal faults and asymmetric grabens, predominantly following these orientations. These structures were segmented by NW-SE-oriented transfer and accommodation zones (Moulin et al., 2012; Buckley et al., 2015; Barnett et al., 2021; Adriano et al., 2022).

These tectonic features controlled the paleorelief and significantly influenced the distribution and thickness of sedimentary facies within the basin. They also played a crucial role in shaping its early structural framework. During this phase, volcaniclastic deposits, including conglomerates, sandstones, and lacustrine shales, were deposited, reflecting the combined influence of tectonic activity and volcanic processes. These deposits are associated with magmatism from the Paraná–Etendeka Large Igneous Province (LIP) (Williams & Hubbard, 1984; Moreira et al., 2007; Rigoti, 2015; Minzoni et al., 2020).

Rift Phase II occurred during the Barremian to Aptian (~130–120 Ma) and marked a transition from active extensional tectonics to a period of reduced tectonic activity, allowing for more stable sedimentation patterns and the development of extensive carbonate platforms (Zwaan & Schreurs, 2017; Péron-Pinvidic & Manatschal, 2019). Although tectonic activity decreased, normal faulting persisted, subtly influencing sedimentation and creating favorable conditions for the formation of transgressive lacustrine environments.

Also in this period, carbonate deposits, including bioclastic grainstones and rudstones, became predominant. This shift in sedimentation marked the onset of a sag basin model, characterized by aggradational and transgressive features in a setting with low tectonic activity (Minzoni et al., 2020; Barnett et al., 2021; Adriano et al., 2022).

The extensive carbonate platforms reflect a period of relative tectonic quiescence and stable accommodation space. However, late-stage volcanic events and localized fault reactivations influenced the deposition of salt from the Ariri Formation and the progradation of carbonate sequences. The basin fill exhibits progradational geometries, as evidenced by grainstone clinoforms prograding from structural highs, indicating a renewed tectonic influence on sedimentation (Garcia et al., 2011; Stanton et al., 2014; Neves et al., 2019)

A significant structural inflection marks the transition from the regional NE/NNE structural trend in the northern pre-salt region to a predominantly NW-oriented trend in the central Santos Basin. This inflection defines the ‘S’-shaped geometry at the center of the pre-salt polygon, which is associated with the Iracema Transfer Zone (Adriano et al., 2022; Araujo et al., 2024; Dehler et al., 2024). Within these zones, N-NE-trending normal faults were reactivated under an E-SE extensional regime, whereas NW-trending faults experienced dextral oblique reactivation, primarily influenced by the structural inheritance of the Proterozoic dextral transpressional Ribeira Belt (**Figure 6**)(Souza, 2008; Matos et al., 2021; Vital et al., 2023; Dehler et al., 2024).

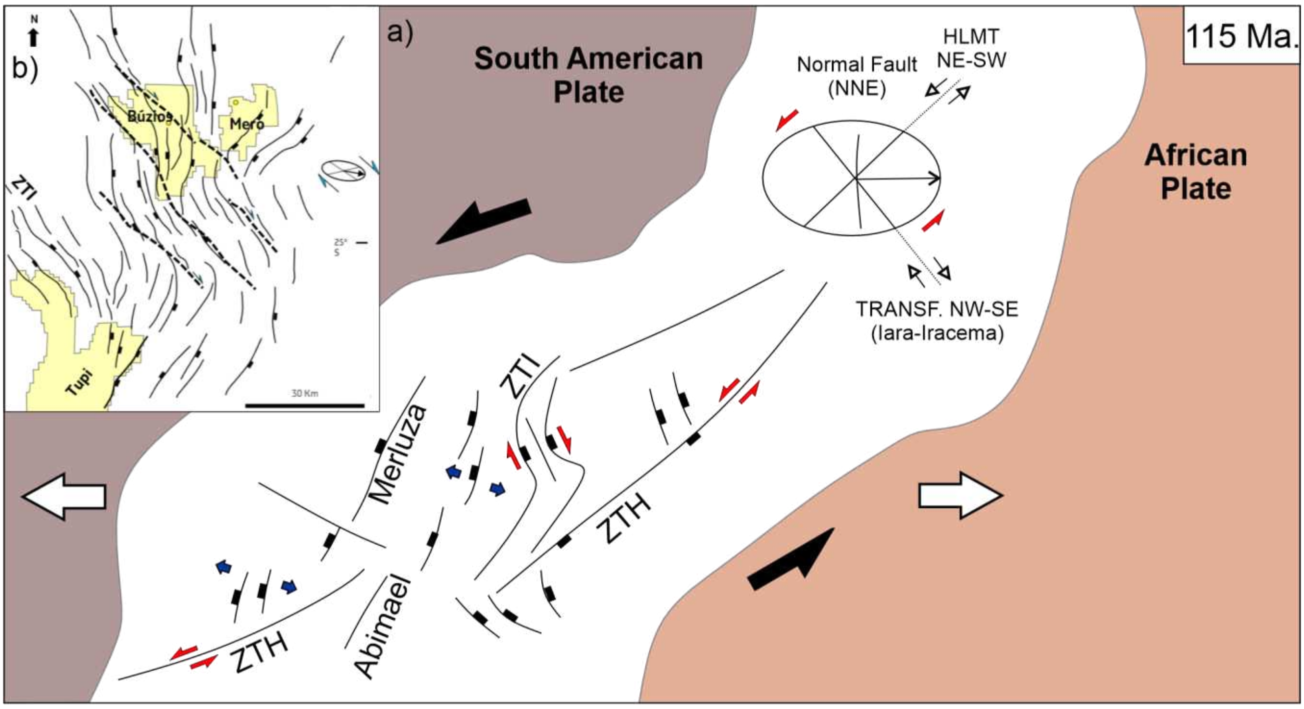

Figure 6: (a) Kinematic schematic illustrating the main regional features and active directions during Rift Phase II, persisting until the breakup. N-NE normal faults were reactivated under E-SE stretching. In contrast, NW-trending faults experienced dextral oblique reactivation (associated with the ‘S’ of Santos and the Iara-Iracema

Transfer Zone – ZTI). The Helmut Transfer Zone (ZTH), oriented E-NE, exhibited sinistral transtensional kinematics. ZTI – Iara-Iracema Transfer Zone and the ‘S’ of Santos (Magnavita et al., 2010); ZTH – Helmut Transfer Zone (Dehler et al., 2016). *(Adapted from Dehler et al., 2024).* (b) Map of transfer zones in the Santos Basin. The ‘S’ of Santos marks the transition of N-NW rift faults in this sector of the Santos Basin, distinct from the regional N-NE fault orientation, which defines the overall structural framework of the basin. The ZTI is subparallel to other NW-SE transfer zones, characteristic of this regional feature (adapted from Dehler et al., 2024).

Following the cessation of rifting, the Santos Basin entered a post-rift phase, during which structural processes continued to shape its architecture and control the evolution of pre-salt sequences. The reactivation of pre-existing faults led to structural inversions, modifying paleotopography and influencing the distribution of sedimentary sequences (Karam et al., 2007). These tectonic movements played a crucial role in redefining trap geometries and reservoir distribution. Furthermore, detachment faults facilitated the development of core complex structures, contributing to the basin's final structural configuration. These features indicate extensional collapse and exhumation processes that affected deeper crustal levels (Moreira et al., 2007; Rodriguez et al., 2021).

Additionally, studies focusing on the structural and depositional characterization of pre-salt reservoirs have revealed evidence of hydrothermal processes. The circulation of hydrothermal fluids, along with post-rift volcanic activity, played a crucial role in diagenetic alteration processes within the reservoir rocks. These processes, including dolomitization and silicification, had a direct impact on reservoir quality by either enhancing or reducing porosity and permeability in the pre-salt carbonates (Lima et al., 2019; Ren et al., 2019).

Hydrothermal fluids interacted with pre-existing rocks through fault systems, facilitating the circulation of hot fluids and driving extensive mineralogical transformations. Evidence of these processes has been observed in the carbonates of the Barra Velha Formation, where hydrothermal alterations have been linked to multi-episodic magmatic activity, with significant events occurring during the Aptian and Santonian-Campanian (Alvarenga et al., 2016; Ren et al., 2019; Vital et al., 2023).

Another significant indicator of hydrothermal activity in the pre-salt is the presence of hydrothermal vent systems. These structures, characterized by pipe-like complexes, form through the fracturing, transport, and extrusion of hydrothermal fluids and sediments (Planke et al., 2005). Such systems are frequently associated with travertine deposits in continental rift settings, as observed in Lake Bogoria, within the Kenya Rift Valley (Renaut & Tiercelin, 1993; Renaut et al., 2012).

Hydrothermal vents are large-scale structures identifiable in seismic data, characterized by their distinctive seismic patterns, which are often linked to intrusive events (Planke et al., 2005; Hansen, 2006). These features have been extensively documented at various stratigraphic levels within sedimentary basins along Brazil's eastern margin, including the pre-salt interval in the Campos and Santos Basins. Hydrothermal vents have been identified in the Aptian interval of the northern Santos Basin, further emphasizing the role of hydrothermal activity in the tectono-sedimentary evolution of the Brazilian pre-salt carbonate systems (Pietzsch et al., 2018; Oliveira et al., 2021).

3.1. Tectonostratigraphy of the Santos Basin

The chronostratigraphy of the Santos Basin reservoirs is defined based on stratigraphic and structural discontinuities identified through geometric, kinematic, stratigraphic, and petrophysical criteria (**Figure 7)** (Moreira et al., 2007; Wright & Barnett, 2020; Gomes et al., 2020; Araujo et.al., 2024).

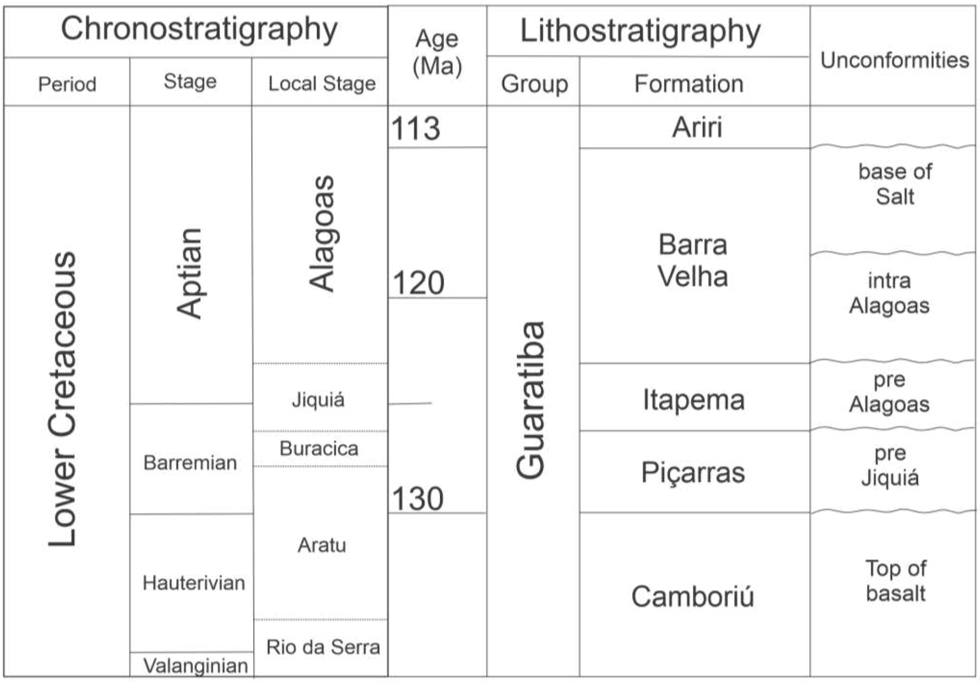

Figure 7: Stratigraphic chart of the Lower Cretaceous in the Santos Basin, showing the chronostratigraphic framework, lithostratigraphic units, and major unconformities that define key tectono-stratigraphic sequences (adapted from Araujo et. al., 2024).

The crystalline basement consists of Precambrian granites, gneisses, and metasediments of the Ribeira Belt, associated with rifting and magmatic events from the South Atlantic Magmatic Province (Rigotti, 2015; Milani, 2016). The base of the pre-salt petroleum system is formed by the Camboriú Formation (Valanginian–Hauterivian), which comprises volcaniclastic sequences of tholeiitic basalts linked to the breakup of Gondwana. Overlying this, the Piçarras Formation (Barremian) records lacustrine and fluvial systems, including alluvial fan deposits and magnesium-rich clays (Moreira et al., 2007).

The pre-Alagoas unconformity, which defines the lower boundary of the Alagoas Group, is an erosive surface representing a phase of mechanical subsidence in the basin. It is directly controlled by the structural framework of the basement and is characterized by continental sedimentation (Guardado et al., 1989; Castro & Picolini, 2016). Above this unconformity lies the Lower Rift Sequence, consisting of lacustrine shales rich in organic matter (Itapema Formation), volcaniclastic siltstones, and fluvial sandstones (Azeredo et al., 2021).

The intra-Alagoas unconformity divides the syn-rift package into two sub-periods: the Lower Rift (early) and Upper Rift (late). It is commonly associated with marked facies changes or internal tectono-stratigraphic events. This surface reflects tectonic reorganization during the Early Aptian (~130–125 Ma), characterized by accelerated subsidence and fault expansion, and may coincide with abrupt variations in stacking patterns or facies transitions (e.g., from fluvial to lacustrine systems). Above this unconformity, the Upper Rift Sequence includes lacustrine carbonates, microbialites of the Barra Velha Formation, and coquinas (Moreira et al., 2007; Wright & Barnett, 2020; Carvalho et al., 2022).

The base of salt unconformity marks the transition from the pre-salt syn-rift sequence to the Aptian evaporites of the Ariri Formation (halite, anhydrite, and other soluble salts), which can reach thicknesses of up to 2,000 m. This discordant surface reflects an abrupt tectonic shift associated with the opening of the South Atlantic, formed under a restricted marine environment and arid climatic conditions. Early halokinesis episodes further deformed this unconformity surface. This interval plays a critical role in the petroleum system as the regional seal for pre-salt accumulations (Moreira et al., 2007; Riccomini et al., 2012; Celini et al., 2024).

3.2. Study area

The study area is located in the central-southern region of the pre-salt polygon, covering approximately 170 km^2. The structural framework is characterized by NW-SE-oriented elongated structural highs alternating with adjacent structural lows. The central structural high features concentric mounds, where wells W01 and W02 are situated. To the north, an elongated mound structure is observed.

In the eastern sector, the topography becomes more irregular, with pronounced structural highs where well W03 is situated. The structural map highlights variations in depth, ranging from approximately -5,000 m to -5,800 m, with shallower regions concentrated near the mounds and deeper areas corresponding to the structural lows. The structural highs and associated mounds are distributed along faulted zones, showing variations in relief and continuity throughout the study area (**Figure *8***).

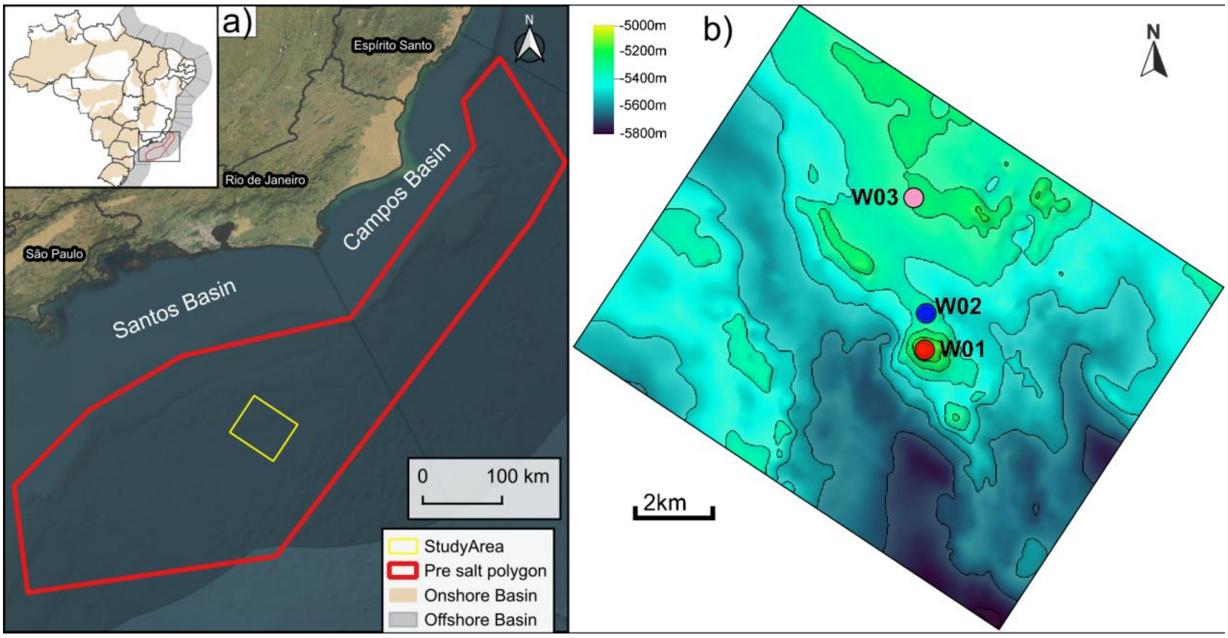

Figure 8: (a) Study area location within the Santos Basin pre-salt polygon. (b) Structural map of the top of the Barra Velha reservoir showing well locations.

4. METHODS

This chapter presents the methodological approach used to analyze fault connectivity within the study area. It includes seismic interpretation, fault classification, topological network analysis, and 3D connectivity modeling. The workflow integrates structural mapping, connectivity metrics, and spatial modeling to assess variations in vertical and horizontal connectivity across reservoir horizons.

4.1. Dataset

A 3D seismic volume covering approximately 290.3 km² was utilized in this study. The dataset, processed using post-stack depth migration, features a spatial resolution of 12.5 × 12.5 meters in both inline and crossline directions. It images subsurface structures at depths ranging from -7,502.50 m to -4,997.50 m, comprising 2,031 inlines and 2,121 crosslines. The vertical sampling interval is 5 m, and the number of samples per trace is 1201. Amplitude values in the volume range from -2.35 to 2.48.

The structural interpretation in this study is based on faults identified within the depth-migrated seismic volume. Given the resolution limitations of the dataset, vertical displacements smaller than 5 m may not be reliably resolved. As such, mapped fault tip-lines and tip-points—defined at locations of "seismic-zero throw"—may correspond to structures with sub-resolution displacements, potentially underestimating their true lateral extent.

While this method enhances the reliability of the interpretation, it remains subject to uncertainties associated with seismic resolution and data noise. Therefore, the conclusions drawn are carefully constrained by the imaging capabilities of the seismic dataset.

4.2. Seismic interpretation workflow

Horizons were initially extracted using the semi-automated 3D seismic interpretation workflow available in Paleoscan software (2022). This process involved applying a model grid to the seismic volume, focusing on the most coherent reflectors, which were highlighted as key horizons within the 3D grid model. The extracted horizons were then cross-validated with formation markers from three available wells (Well 01, Well 02, and Well 03) to ensure accurate identification of the stratigraphic targets.

Four horizons were extracted based on reflector the highlighted by well markers: the Top Itapema, corresponding to the base of the reservoir (Pre-Alagoas Unconformity); the

Lower Barra Velha (LBV), associated with the Intra-Alagoas Unconformity; the Intermediate Barra Velha (IBV); and the Upper Barra Velha (UBV), corresponding to the base of the salt. Manual refinements were applied in regions where interpolation inconsistencies were observed, utilizing both crossline and inline seismic sections to ensure spatial coherence.

Given that post-stack seismic volumes often contain random noise, a dip-steered median filter was applied in OpendTect 7.0 to enhance the continuity of seismic reflectors by filtering along the local structural dip. Following this, the Fault Likelihood and Ant Tracking attributes were generated to improve the detection and visualization of fault orientations and geometries. These attributes served as the basis for subsequent manual fault interpretation on seismic sections oriented perpendicular to the regional fault trends. Fault interpretations were manually conducted in Petrel E&P software (2022), with interpretations made on every 10-intersection plane to ensure consistency and resolution across the seismic volume.

4.3. Structural characterization

4.3.1. Fault set classification

After interpreting the faults from the seismic data, they were classified into four sets (F1 to F4) based on an analysis that considered their orientation, length, tectonic characteristics, and position within the reservoir. Orientation criteria focused on determining the dominant strike directions of faults. Rose diagrams were generated to visually represent the primary fault orientations, facilitating the identification and grouping of fault sets. The length was evaluated by analyzing the spatial continuity of faults across the seismic volume. To support this analysis, histograms of fault trace lengths were created, providing a distribution and facilitating the grouping of faults on the map.

The tectonic characteristics of faults were analyzed to distinguish between normal, reverse, and strike-slip fault types. To achieve this, vertical fault displacement versus distance along the fault (D-L) plots were constructed (**Figure 9**). These plots were generated by calculating the hanging wall cutoff, a curve formed by the intersection points of geological layers on the upper block of the fault plane, and the footwall cutoff, a curve formed by the intersection points of layers on the lower block of the fault plane using the software Petrel (2022). This methodology follows the principles of Allan fault plane diagrams, providing a comprehensive representation of fault displacement and structural behavior.

Additionally, the relationship between fault length and vertical displacement is fundamental for understanding the tectono-structural evolution of fault-dominated systems, such as rift basins (Kim & Sanderson, 2004; Torabi et al., 2018; Fossen, 2020). In isolated faults, D-L profiles typically show displacement starting at zero at the fault tips, increasing progressively toward a maximum value near the fault center, reflecting the fault's propagation and slip history over time (Peacock, 2002).

However, segmented faults exhibit peaks and troughs along the displacement curve, suggesting interaction during their propagation and growth, rather than independent evolution (Walsh et al., 2002). This interaction modifies growth dynamics, meaning the maximum displacement point does not necessarily align with the nucleation point, except in simple or minimally segmented faults. In contrast, highly segmented faults reflect a more complex evolutionary history, influenced by segment linkage and interaction processes (Guomundsson et al., 2013; Lathrop et al., 2022).

Conceptually, a normal fault is characterized by the downward displacement of the hanging wall relative to the footwall. Conversely, in a reverse fault, the hanging wall is displaced upward in relation to the footwall. Therefore, when analyzing the D-L curves, the tectonic regime is considered normal if the difference between the throw of the hanging wall and the throw of the footwall at a given point is positive. If this difference is negative, the fault is classified as reverse (**Figure 9.b**).

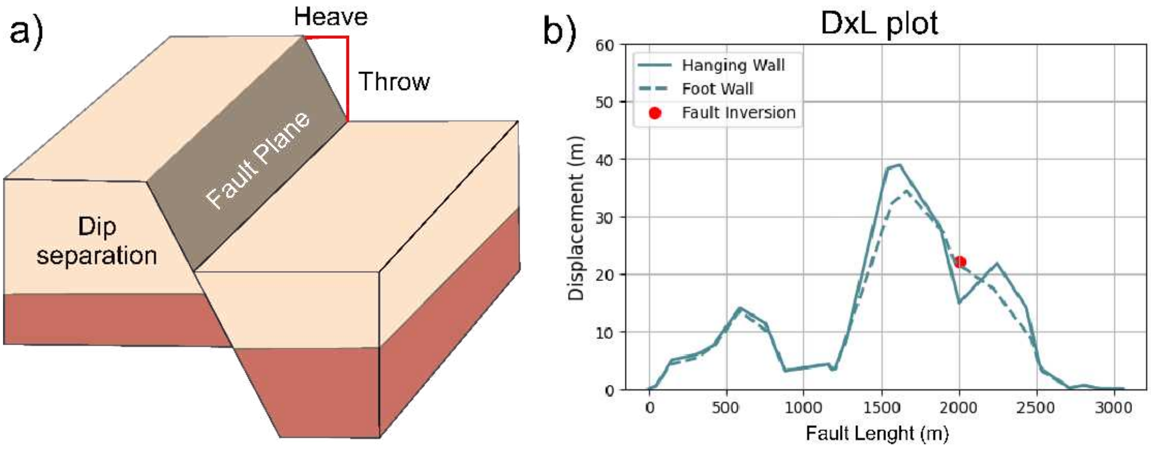

Figure 9: (a) Normal fault block diagram: throw represents the vertical displacement along the fault, while heave measures the horizontal offset between fault blocks. (b) D-L plot showing the curves of the hanging wall and footwall on a fault plane, highlighting the inversion where the hanging wall becomes higher than the footwall.

Furthermore, a fault can be classified as inverted when the following criteria are met: the presence of a preserved syn-extensional sequence in the hanging wall, indicating an original normal faulting regime; discrepancies in marker horizons along the fault, with anomalous elevations either above or below regional levels; a shift in the structural behavior of the fault over time, typically revealed by D–L curves that indicate reversed displacement patterns; evidence of asymmetric folding related to compressional reactivation, such as monoclines facing the footwall; and, potentially, the formation of footwall shortcut faults, which assist in reorienting the fault system to accommodate the new compressional stress regime.

Finally, perpendicular cross-sections to the fault planes were constructed to assess the vertical extent and distribution of faults across stratigraphic intervals within the Barra Velha reservoir. The fault classification was further validated through structural modeling and detailed seismic section analysis.

4.3.1. True vertical thickness maps

True vertical thickness (TVT) isochores were calculated between the interpreted structural horizons of the framework model to represent the stratigraphic thickness intervals. The workflow was based on volume-based modeling (VBM) in depth (TVD).

Initially, four key horizons were interpreted and incorporated into the structural framework. For example, the Lower Barra Velha horizon was selected as the reference for isochore generation. In the Isochore Modeling group of Petrel, the True Vertical Thickness operation was applied, specifying the Itapema Horizon as the base horizon. This procedure generated a point set with a defined XY spacing, where each point carries an attribute representing the TVT calculated between the selected top and base horizons.

The same methodology was subsequently applied to generate additional thickness maps for the Intermedium Barra Velha (top) – Lower Barra Velha (base) interval and the Upper Barra Velha (top) – Intermedium Barra Velha (base) interval.

The generated point sets were configured with the *Restrict to complete zones* option enabled. This ensured that points were created only where the top and base horizons fully overlapped, preventing thickness calculations across truncated, eroded, or fault-displaced intervals.

After generations, the TVT point sets were quality-checked and, when necessary, smoothed or geologically adjusted. Regular surfaces were then created from the TVT attributes and used in Horizon Modeling to regenerate and refine base horizons, ensuring geometric consistency with the structural tops.

4.4. Faults Network Topology

Topological analysis reveals fault interconnectivity and spatial arrangement, utilizing scale-invariant parameters to establish a robust framework. This approach prioritizes connectivity and network interactions, reducing biases and providing deeper insights into the influence of fault networks on flow and permeability (Peacock & Sanderson, 2018; Sanderson & Nixon, 2018).

In topological studies, a 2D fracture network is conceptualized as a system comprising lines, branches, and nodes. Specifically, nodes represent points where fractures intersect and are classified based on the number of fractures they intersect. For instance, I-nodes correspond to isolated fracture tips, Y-nodes denote intersections where one fracture terminates against another (such as abutments or splays), and X-nodes indicate intersections involving three or more fractures (Sanderson & Nixon, 2015; Peacock et al., 2018).

Unlike fracture traces, which can be ambiguous and subjective, branches offer a consistent and reproducible method for representing networks, as they are uniquely defined by their connecting nodes (Sanderson & Nixon, 2015; Peacock et al., 2018). Branches are categorized into three main types: I–I branches, which connect two isolated nodes (I-nodes); I–C branches, which link an isolated node to a connecting node; and C–C branches, which join two connecting nodes, representing doubly connected segments within the network (Hoffman et al., 2006; Sanderson & Nixon, 2015; Peacock et al., 2018).

The proportions of node and branch types provide critical insights into the connectivity and structural organization of fault networks (Sanderson & Nixon, 2015; Meijer et al., 2018). Node counts (NI, NY, NX) and branch counts (BI-I, BI-C, BC-C) are commonly represented in ternary diagrams, effectively visualizing these proportions. The relationship between nodes and branches is expressed through the following equation:

$$NB = \left(\frac{NF + 3NY''}{2} \right) \quad (1)$$

These counts are also used to calculate connectivity metrics, such as connections per branch (CB), which provide a dimensionless measure of network connectivity ranging from 0 (indicating isolated branches) to 2 (fully connected branches) (Sanderson & Nixon, 2015; Sanderson & Nixon, 2018; Nyberg et al., 2018). The equation for calculating CB is shown below:

$$CB = \frac{(3NY + 4NX)}{NB} \quad (2)$$

Another commonly used parameter, the average degree (D), quantifies the connectivity of a fracture network by measuring the ratio between the number of branches (B) and the number of nodes (N) (Sanderson et al., 2019). The equation is expressed as:

$$D = \frac{2B}{N} \quad (3)$$

According to the results, D values range from 1, indicating a poorly connected network with isolated branches, to 4, representing a fully connected system dominated by cross-cutting fractures. Studies on natural fracture networks, particularly in joint and fault systems, indicate that they are typically dominated by Y-nodes and exhibit D values ranging from 1 to 3 (Morley & Nixon, 2016; Duffy et al., 2017).

This study utilized the NetworkGT plugin in QGIS 3.32.3 to digitize fault traces from several 2D depth slices and seismic horizons throughout the 3D volume, extracting geometries, branches, nodes, and topological information from the faults represented (Nyberg et al., 2018). The depth slices and horizons were processed using the ant-tracking seismic attribute, enhancing the visibility of structural features. Faults were manually vectorized in QGIS, resulting in detailed fault trace datasets.

A 2D grid with parameters of 200 m spacing, a 500 m radius, and a 40° rotation was applied to represent horizontal planes for each depth slice and horizon. This grid facilitated the classification of vectorized fault traces into branches and node types, enabling the calculation of critical topological metrics, such as connections per branch (CB) and connections per line (CL), as well as fault intensity. This provided comprehensive insights into the fault network (**Figure 10**).

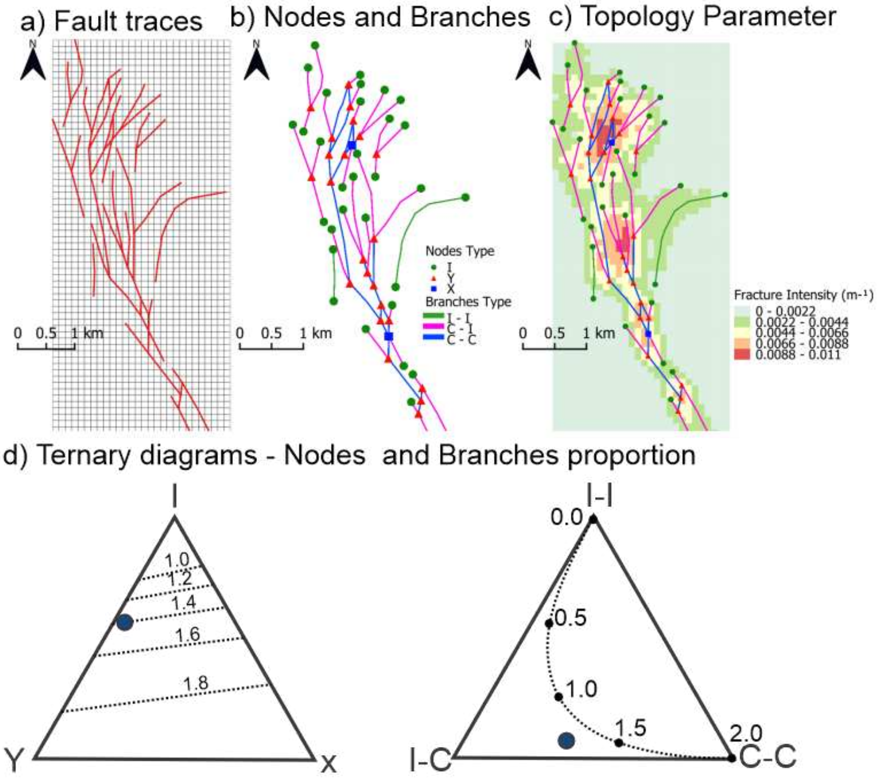

Figure 10: (a) Fault traces mapped in a 2D grid with defined spatial intervals show the faults' arrangement within the study area. (b) Classification of nodes (I, Y, and X) and branches (I-I, I-C, C-C) in the fault network. (c) Spatial distribution of fracture intensity (m $^{-1}$) represented on a color scale, providing insight into fault network density and connectivity. (d) Proportions of node types are represented in a triangular plot, illustrating the relationship between node types (I, Y, X) and connections per branch (CB). Classification of branch types in a ternary plot, showing proportions of branch types (I-I, I-C, C-C) with CB values ranging from 0 to 2.0.

4.5. 3D fault connectivity model

The 3D fault connectivity model was developed by integrating structural maps, fault intensity, and branch connections across different stratigraphic horizons. This approach allowed for a detailed characterization of fault sets, fault geometry, interconnections, and areas with the highest concentration of fault linkages.

To define connectivity zones, polygons were manually delineated based on similar structural characteristics and the overall fault geometry of the study area. Five distinct connectivity classes were assigned to each horizon. These polygons were then imported into Petrel 2022 and incorporated into the structural grid of the study area, which consists of stratigraphic units corresponding to the reservoir horizons.

The grid population process involved vertical interpolation of the connectivity zones, generating a 3D model that captures both vertical and horizontal continuity of fault connectivity patterns. Cross-sections were extracted from the 3D model to analyze the distribution of connectivity zones and their interaction with regional fault structures, providing insights into the spatial organization of fault networks and their potential impact on reservoir compartmentalization.

5. RESULTS

Understanding fault architecture and connectivity patterns is crucial for assessing compartmentalization and fluid flow within carbonate reservoirs. In this chapter, we present a structural and connectivity analysis of the Barra Velha Formation, the reservoir interval of the Santos Basin pre-salt succession. Integrating 3D seismic interpretation, fault classification, displacement analysis, and topological assessment, this study aims to establish a geologic framework that supports reservoir modeling and flow simulation efforts.

5.1. Structural analysis

Four horizons were interpreted within the pre-salt reservoir interval. The basal horizon corresponds to the Pre-Alagoas Unconformity (PAU), also known as the top of the Itapema Formation. A high-amplitude negative reflector characterizes it and is here referred to as the Itapema Horizon. Above it, the second horizon is a high-amplitude positive reflector associated with the Intra-Alagoas Unconformity (IAU), which also corresponds to the top of the Lower Rift phase in the regional structural framework. This surface is called the Lower Barra Velha Horizon (LBV).

The intermediate horizon corresponds to a continuous high-amplitude seismic reflector, characterized by impedance contrast and lateral continuity, and is referred to as the Intermediate Barra Velha Horizon (IBV). Finally, the top horizon is a high-amplitude positive reflector representing the unconformity at the base of the salt layer, which also corresponds to the top of the Barra Velha Formation. This horizon is referred to as the Upper Barra Velha Horizon (UBV).

The structural maps for each horizon show the mapped faults, predominantly oriented NW–SE, as well as the distribution of structural highs and lows (**Figure 11**). Four main structural highs were identified:

- **H1**, located in the western portion of the study area, is bounded by normal faults with opposite dips, forming a classic horst structure. The topographic contrast between H1 and the surrounding areas gradually decreases from the base to the top of the reservoir.

- **H2**, situated in the central part of the area, is also bounded by normal faults and shows structural association with strike-slip faults. In the uppermost horizon, reverse faults occur locally associated with mounded structures.

- **H3** includes faults with less pronounced displacement and throw. From base to top, this structural height evolves into a more tabular geometry and begins to interact with H2.

- **H4**, located at the easternmost portion of the study area, appears to represent a segment of a larger adjacent structure. Normal faults also bound it and show geometric continuity with regional structural trends.

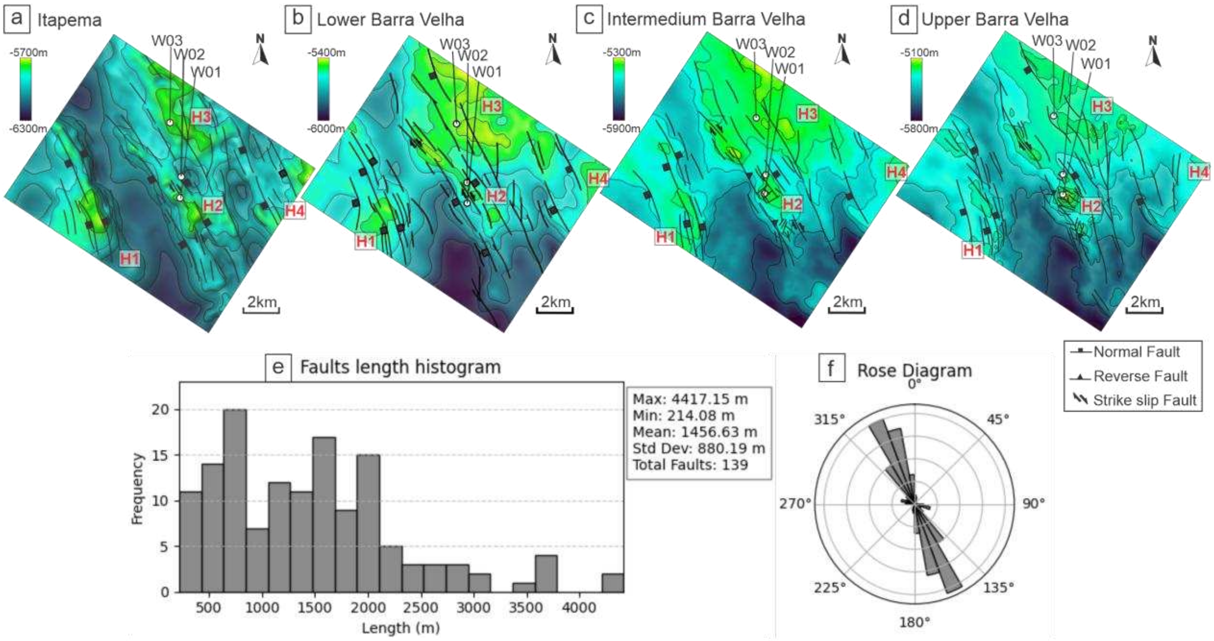

Figure 11: Structural maps showing normal, reverse, and strike-slip faults, as well as structural highs for each horizon. (a) Itapema Horizon; (b) LBV; (c) IBV; (d) UBV. (e) Histogram of fault lengths. (f) Rose diagram showing the dominant strike directions of the main faults.

The thickness maps illustrate the variation in geological unit thickness between two horizons of the structural model (**Figure 12**). Cool colors highlight the areas with greater thickness, ranging from 300 to 500 meters, while warm colors indicate thinner zones. Analyzing the three stratigraphic units of the reservoir from base to top, we observe a general trend of decreasing thickness upward. The bottom interval displays the most significant variability in thickness distribution compared to the intermediate and upper intervals.

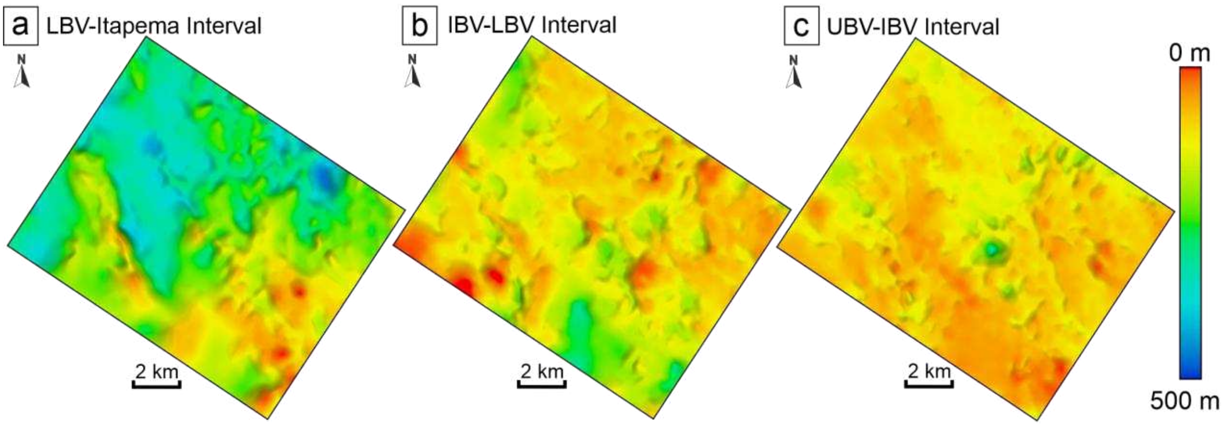

Figure 12: True vertical thickness maps (a) LBV-Itapema interval. (b) IBV-LBV interval (c) UBV-IBV interval.

The lower interval, bounded by the LBV horizon at the top and the Itapema Formation at the base, has an average true vertical thickness of approximately 230 meters. The thickest areas, ranging from 300 to 500 meters, are predominantly located in the northern portion of the field, while thinner regions, ranging from 25 to 200 meters, are concentrated in the south.

Stratigraphically above, the intermediate interval between the IBV and LBV horizons exhibits an average thickness of 120 meters. This interval is characterized by a central, thicker corridor with values ranging from 150 to 320 meters, whereas the eastern and western flanks are thinner, varying in width from 10 to 100 meters.

The upper interval, defined between the UBV and IBV horizons, presents the most homogeneous thickness distribution, with an average of 94 meters and values generally ranging from 5 to 100 meters. Notably, this unit contains a localized, concave-shaped depocenter that reaches a maximum thickness of approximately 100 meters.

5.2. Fault set classification

The faults interpreted along the reservoir horizons exhibit distinct horizontal and vertical dimensions and distributions. The major faults cut through the entire reservoir interval and extend across the study area, defining the structural framework of the field. In contrast, the minor faults are confined to upper stratigraphic intervals, typically concentrated in structural highs and interacting with the major fault systems.

Accordingly, the fault set labeled (F1) comprises 47 identified faults, interpreted as regional structures extending from the Camboriú Formation to the top of the Barra Velha Formation reservoir. These tectonic features predominantly exhibit normal faulting, with a main orientation of NW–SE. Their lengths range from 1,241.94 m to 4,417.15 m, with an average of 2,325.45 m, and they display significant lateral continuity (**Figure 13**).

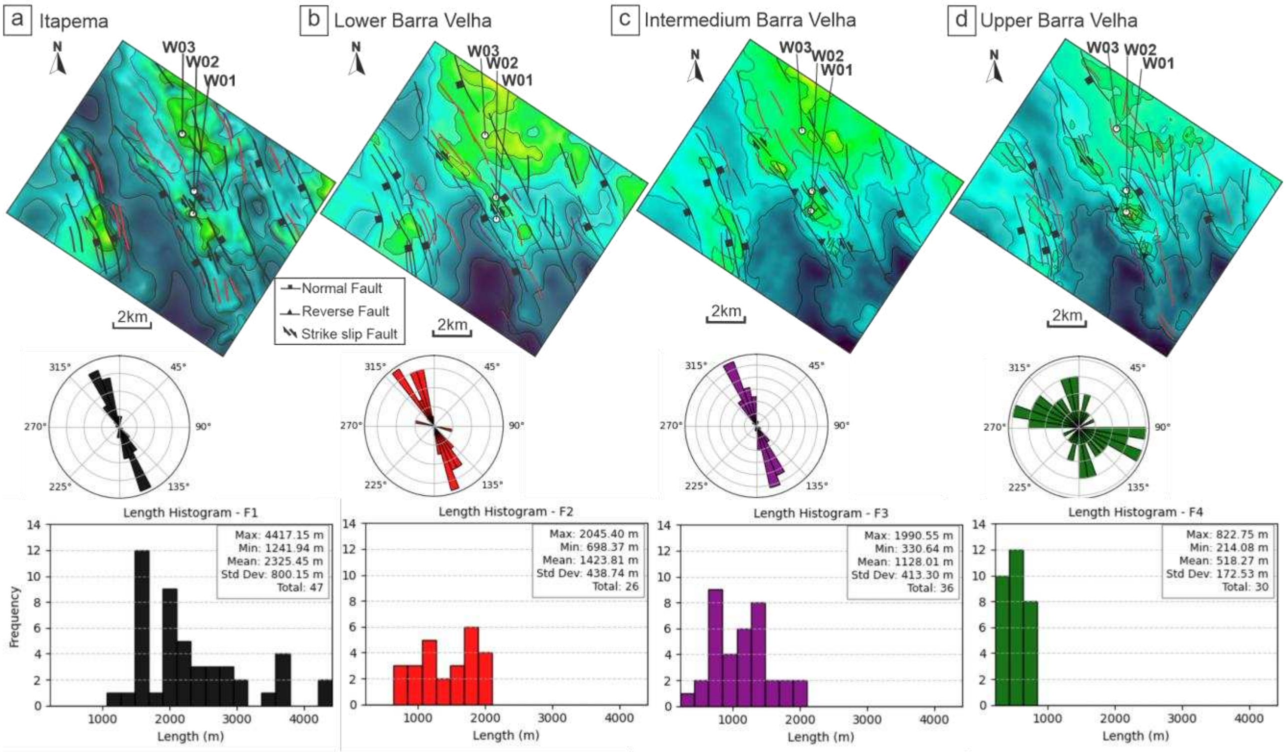

Figure 13: Structural maps and fault sets classification. Frequency histogram and rose diagrams showing the orientations of the fault sets F1 (black), F2 (red), F3 (purple), and F4 (green). (a) Itapema, (b) LBV, (c) IBV, and (d) UBV. Frequency histogram and rose diagrams showing the orientations of the fault sets F1 (black), F2 (red), F3 (purple), and F4 (green).

The second fault set (F2) comprises 26 faults that are positioned parallel to the regional faults (F1) and are confined within the Barra Velha reservoir interval. Their lengths range from 698.37 to 2,045.40 meters, with an average of 1,423.81 meters. Similar to the first set, the F2 faults are predominantly normal and generally oriented NW–SE. A directional variation toward NNE–SSW is observed in the eastern portion of the field. (**Figure 13**).

With 36 interpreted fault segments, the third fault set (F3) consists of secondary abutting faults located adjacent to the regional F1 and F2 sets. These faults typically occur near the top of normal fault planes, where the dip is inclined along slopes formed between structural highs and lows. Smaller in scale than sets F1 and F2, their lengths range from 330.64 to 1,990.55 meters, with an average of 1,128.01 meters. The F3 faults generally follow an NNE–SSW orientation. Their occurrence is more pronounced in the IBV zone and gradually decreases toward the UBV zone (**Figure 13**).

The fourth fault set (F4), comprising 30 fault segments, is characterized by sub-vertical faults located in the southern part of the field. These faults exhibit sub-vertical geometries and are restricted to the tops of the mounds, initiating at the base of the Upper Barra Velha interval. F4 is the shortest fault set, with lengths ranging from 214.08 m to 822.75 m, averaging 518.27 m. The main orientation is NW–SE, though E–W orientations may also occur (**Figure 13**).

Four seismic profiles, representing sections that cross the principal mounds of the study area, were interpreted to observe the vertical fault behavior of the sets (F1 to F4). Profile A–A’ (**Figure 14**) highlights the structural framework of Mound 01. The F1 set extends beyond the reservoir interval and appears to exert primary structural control over the reservoir. F1 is predominantly normal, but becomes sub-vertical with strike-slip components near the center of the mound. F2 originates at the base of the reservoir and tends to terminate near its top. This set inherits the normal kinematics and dip direction of F1, forming a domino-style arrangement that aligns with the regional extension. F3 occurs as abutting structures at the top of major faults such as F1, mainly within the IBV interval. Additionally, F4 consists of minor sub-vertical faults located at the crest of the mound.

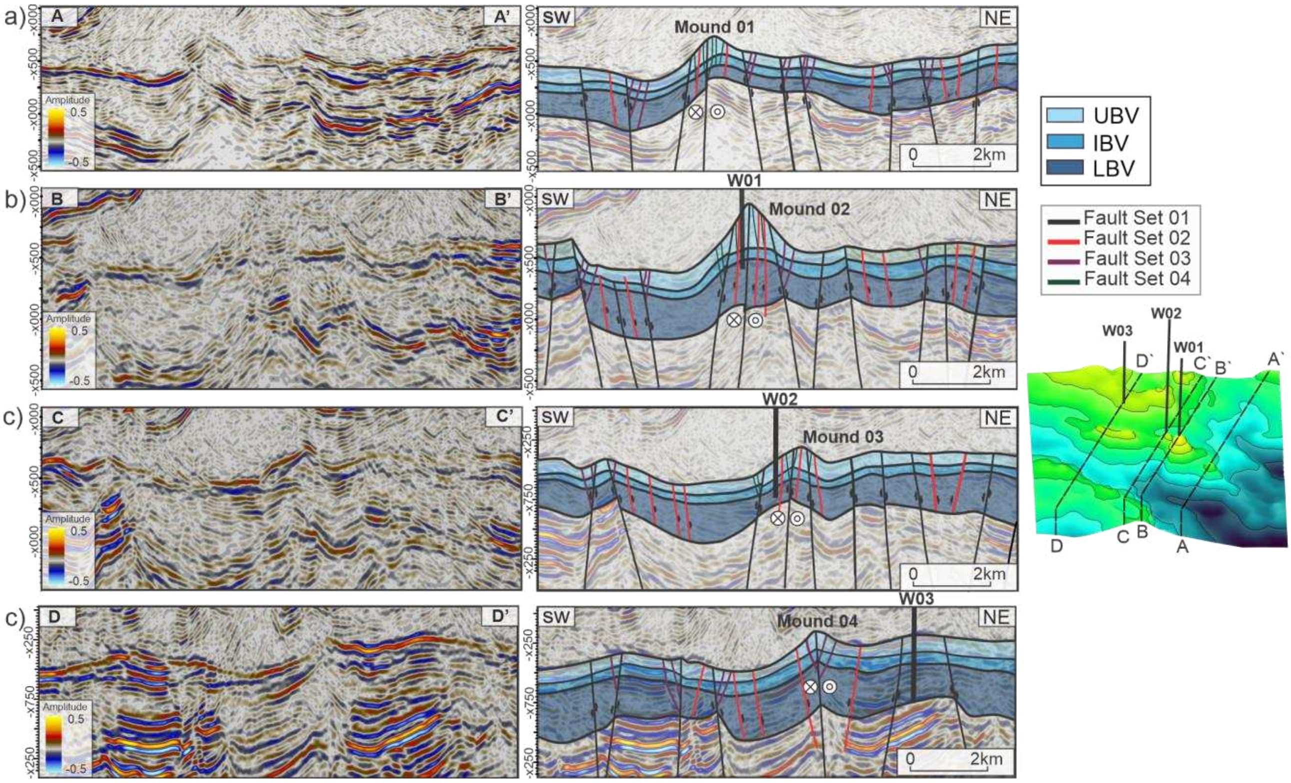

Figure 14: Seismic profiles showing fault interpretation and structural configuration of mounds in the Barra Velha Formation. (a) Section A-A’ Mound 01 profile. (b) Section B-B’ Mound 02 profile. (c) Section C-C’ Mound 03 profile. (d) Section D-D’ Mound 04 profile.

Profile B–B’ (**Figure 14**) focuses on Mound 02, revealing structural characteristics similar to those observed in the previously described profile. Faults F1 and F2 appear to represent the lateral continuation of those from the previous section. The throw of the major faults is more pronounced here, highlighting an increase in stratigraphic thickness, especially adjacent to F1. Mound 02 stands out as the topographically highest feature in the study area. F3 still exhibits abutting behavior against major faults, while the sub-vertical F4 faults are more intense in this mound area.

Profile C–C’ (**Figure 14**) crosses Mound 03 and reveals increased structural complexity. Fault sets F1 and F2 exhibit similar behavior; however, in the southwestern portion of the profile, the concave geometry of the stratigraphic units, shaped by F2 faults, clearly outlines a domino-style extensional pattern. F3 faults are less frequent in this section due to the reduced occurrence of F1, and are mainly localized as abutting faults near the tops of major normal faults. F4 faults remain restricted to the uppermost part of the mound. Profile D–D’ focuses on Mound 04, where the central F1 fault exhibits strike-slip behavior and no occurrence of F4 faults is observed.

The frequency curve analysis based on fault set counts for each interpreted section indicates that F1 remains continuous throughout the LBV and IBV intervals but shows a declining trend in the UBV interval. For fault set F2, the frequency curve initially increases in the LBV interval, reaches a peak in the IBV interval, and subsequently declines in the UBV. Fault set F3 begins to appear near the end of the LBV interval, with its frequency decreasing shortly after the IBV interval. In sections C and D, F3 curves are observed midway through the UBV interval. In contrast, fault set F4 first appears at the end of the IBV interval, forming a conical-shaped frequency curve that peaks in the middle of the UBV interval before declining within the same stratigraphic layer (**Figure 15**).

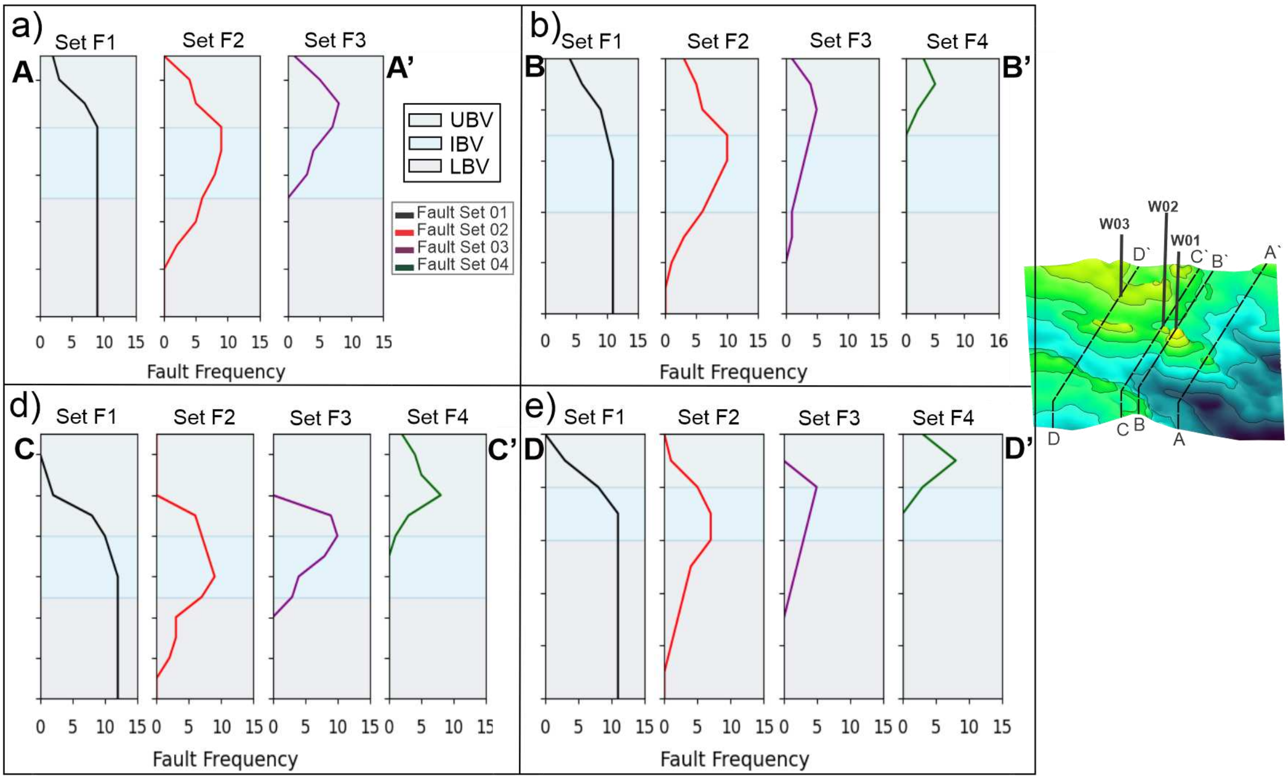

Figure 15: Fault frequency curves plot across Barra Velha stratigraphic intervals: (a) Section A-A', mound 01. (b) Section B-B', mound 02. (c) Section C-C', mound 03. (d) Section D-D', mound 04.

5.3. Fault displacement analysis

To complement the structural analysis of the regional fault set (F1), displacement–length (D–L) plots were generated to illustrate variations in displacement along fault lengths across four stratigraphic horizons (Itapema, LBV, IBV, and UBV). Each fault was analyzed by comparing displacement measurements on both the hanging wall and footwall, with inversion points (highlighted in red) marking locations where hanging wall displacement exceeds that of the footwall. Dashed lines delineate distinct segments along the fault traces, indicating zones of varying maximum displacement within the D–L profiles. For systematic presentation, the faults were grouped into three sectors—western, central, and eastern—based on their spatial distribution within the study area.

The F01 and F02 faults are situated in the western sector of the study area, adjacent to a structural high and a slope that descends into the lower structural region (**Figure 16**). The D-L analysis reveals that F01 exhibits a displacement ranging from 103.5 m in the Itapema horizon to 24.4 m in the UBV horizon, with a relatively simple segmentation pattern, dividing the curve into two segments in the IBV and UBV horizon plots. F02, on the other hand, presents higher displacement values than F01, reaching a maximum of 166.8 m in Itapema and 58 m in

UBV. Additionally, F02 displays greater segmentation in its displacement curves, with three segments in the Itapema, LBV, and IBV horizons, and four segments in UBV.

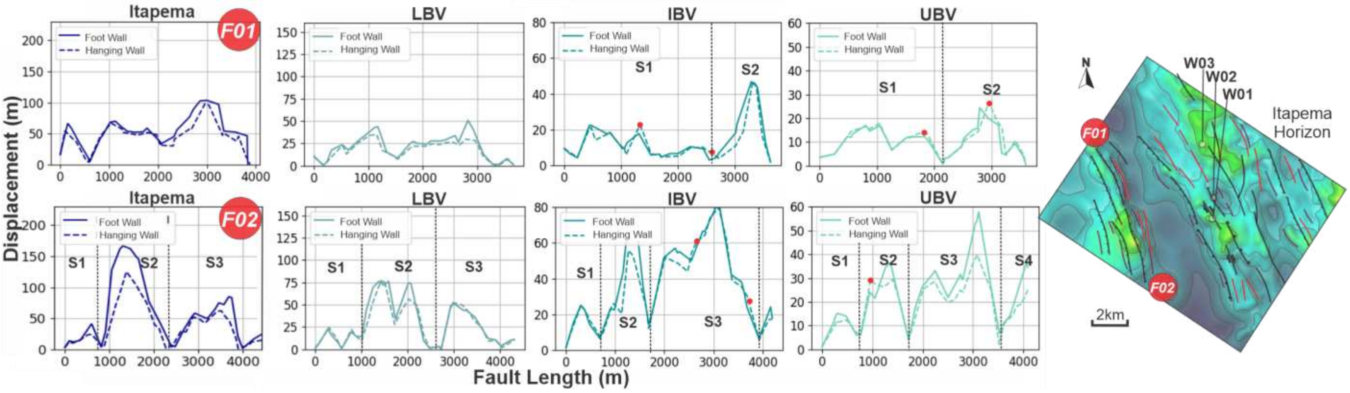

Figure 16: Fault displacement-length (D-L) plots for faults F01 and F02 located in the western sector of the study area. The vertical dashed lines (S1, S2, S3, S4) indicate structural segments along the fault. Red dots highlight specific points where the hanging wall curve exceeds the footwall curve. The right panel shows the structural map of the Itapema Horizon, with fault sets and well locations (W01, W02, W03). The positions of faults F01 and F02 are highlighted in red circles.

The F03, F04, and F05 faults, situated in the central sector of the study area, also occur within a structural high adjacent to the slope leading to the lower structural region (**Figure 17**). The D–L plots for this group reveal a progressive decrease in displacement from the base to the top of the reservoir. Additionally, a northward trend of decreasing segmentation is observed, with faults F03 and F04 exhibiting fewer segments compared to F05. F03, located in the northernmost part of the sector, shows a maximum displacement of 42 m in the Itapema horizon and a minimum of 8.9 m in the UBV horizon, making it the smallest fault in terms of displacement. Segmentation is observed only in the IBV and UBV horizons.

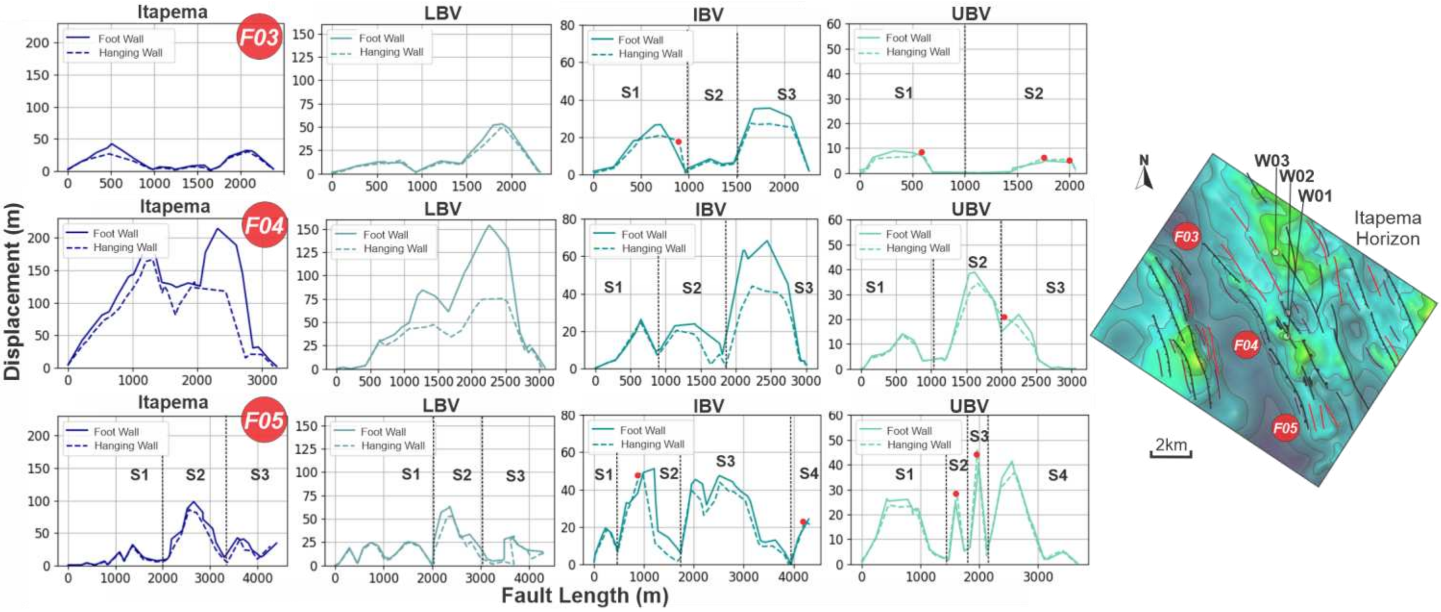

Figure 17: Fault displacement-length (D-L) plots for faults F03, F04, and F05 located in the central sector of the study area. The graphs show the variation in fault displacement along the stratigraphic units: Itapema, LBV, IBV, and UBV. From the south (F05), the faults are more segmented and exhibit higher displacement values, while toward the north (F03), the faults become less segmented and displacement decreases.

F04, situated near the prominent carbonate mounds in the study area, exhibits the highest displacement within this group, reaching 214 m in the Itapema horizon and 39 m in the UBV horizon. It displays three distinct segments exclusively in the IBV and UBV displacement curves. F05, located further south, presents intermediate displacement values of 98.3 m in Itapema and 41.5 m in UBV, with segmentation observed across all horizons. The displacement curves for F05 are divided into three segments in the Itapema and LBV horizons, and four segments in the IBV and UBV horizons.

Faults F06 and F07 are also located in the central area (**Figure 18**) but exhibit different characteristics compared to the fault group (F03, F04, and F05). Fault F06 shows a maximum displacement of 31 m at the IBV horizon and a minimum of 9.3 m at the UBV horizon. In the case of F07, the maximum displacement occurs at the Itapema horizon, reaching 76.7 m, while the minimum displacement is observed at the UBV horizon with 11.8 m. Unlike the other fault groups, no segmentation is observed in the D-L curve; only a single peak of maximum displacement stands out.

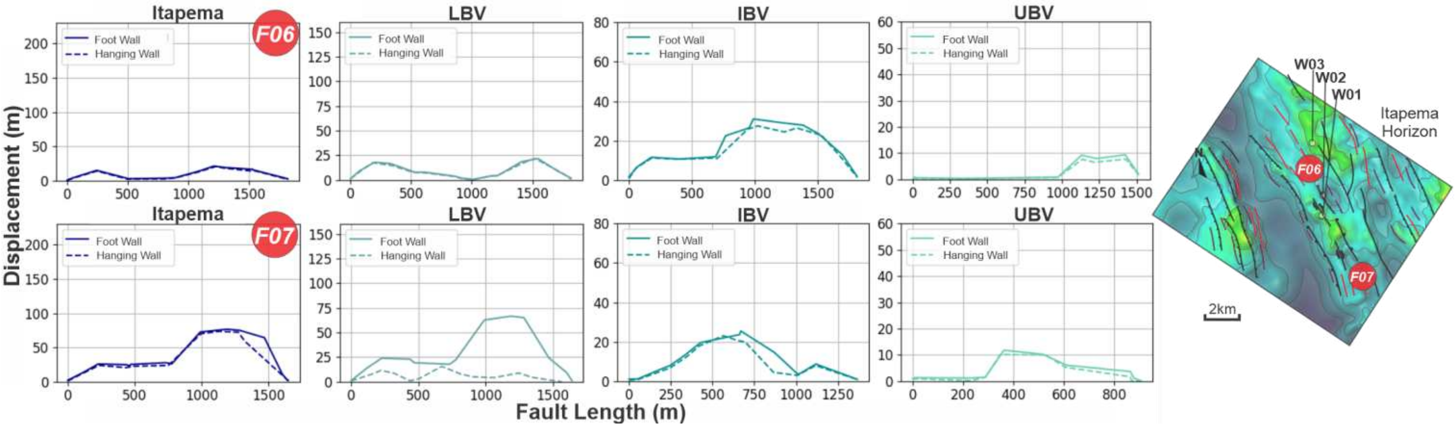

Figure 18: Fault displacement-length (D-L) plots for faults F06 and F07 in the central sector of the study area. D-L curves do not exhibit segmentation, displaying only a single prominent peak of maximum displacement.

Faults F08, F09, and F10, located in the eastern sector of the study area, are associated with a tabular structural high within a relatively smooth topographic setting (**Figure 19**). Overall, the D-L curves indicate that all horizons exhibit segmentation along the fault plane. Fault F08 displays a maximum displacement of 93 m in the LBV horizon and a minimum of 26.7 m in UBV, with segmentation starting from the Itapema horizon and continuing with three segments in LBV, IBV, and UBV, along with inversion points in IBV and UBV.

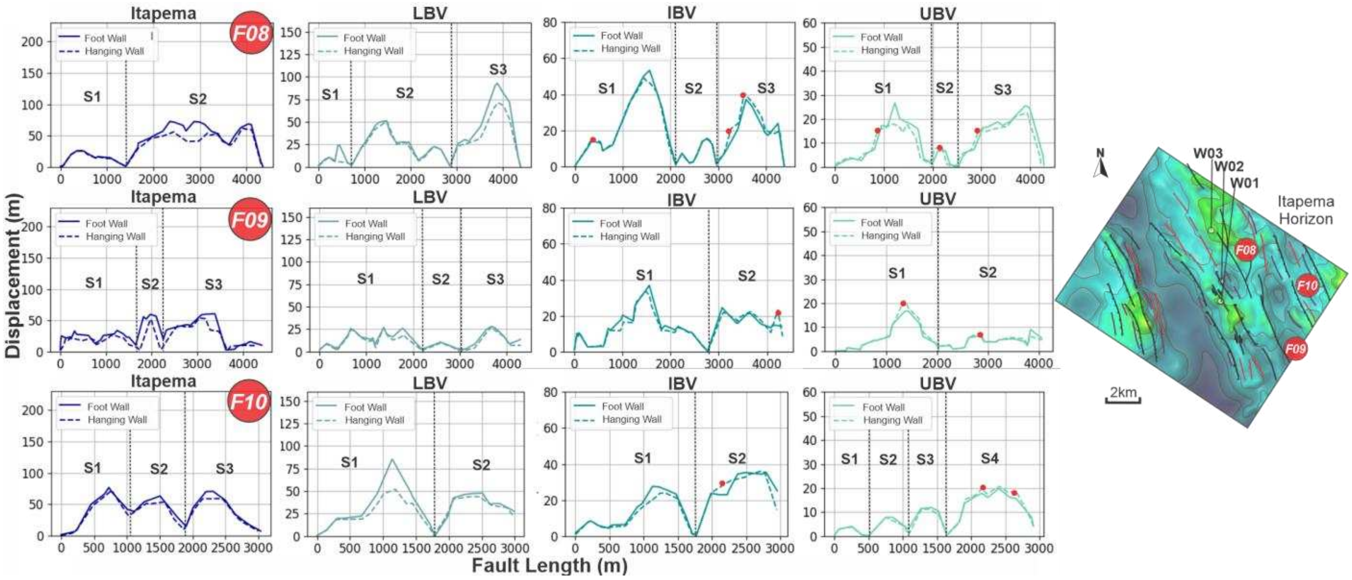

Figure 19: Fault displacement-length (D-L) plots for faults F08, F09, and F10 in the eastern sector of the study area. Segmentation is observed along all D-L curves, with inversion points identified in the IBV and UBV horizons.

Fault F09 reaches a maximum displacement of 60.8 m in Itapema and a minimum of 16.8 m in UBV, exhibiting more pronounced segmentation in Itapema and LBV. This segmentation decreases to two segments in IBV and UBV, where inversion points remain present. Fault F10 records its maximum displacement in LBV (85 m) and its minimum in UBV (19.8 m), exhibiting a strong segmentation pattern with three displacement peaks in Itapema, two in LBV and IBV, and four in UBV. Additionally, inversion points are observed in the IBV and UBV curves for all three analyzed faults.

5.4. Structural characterization of connectivity type

Based on the fault trace patterns digitized across the four horizons using ant tracking and variance attributes, four distinct fault interaction types were identified. These connectivity types were classified according to their geometry, fault length, orientation, topography, and fault intensity. The characteristics of each connectivity type are detailed below.

The **splay connectivity type** represents the largest connectivity zone in the study area and is predominantly located within the eastern structural highs. This type consists of secondary faults (F2 and F3) branching from principal faults (F1) at acute angles ranging from 10° to 45°. Fault intensity maps show the highest fault concentrations at branching points of the principal faults (**Figure 20a**, b).

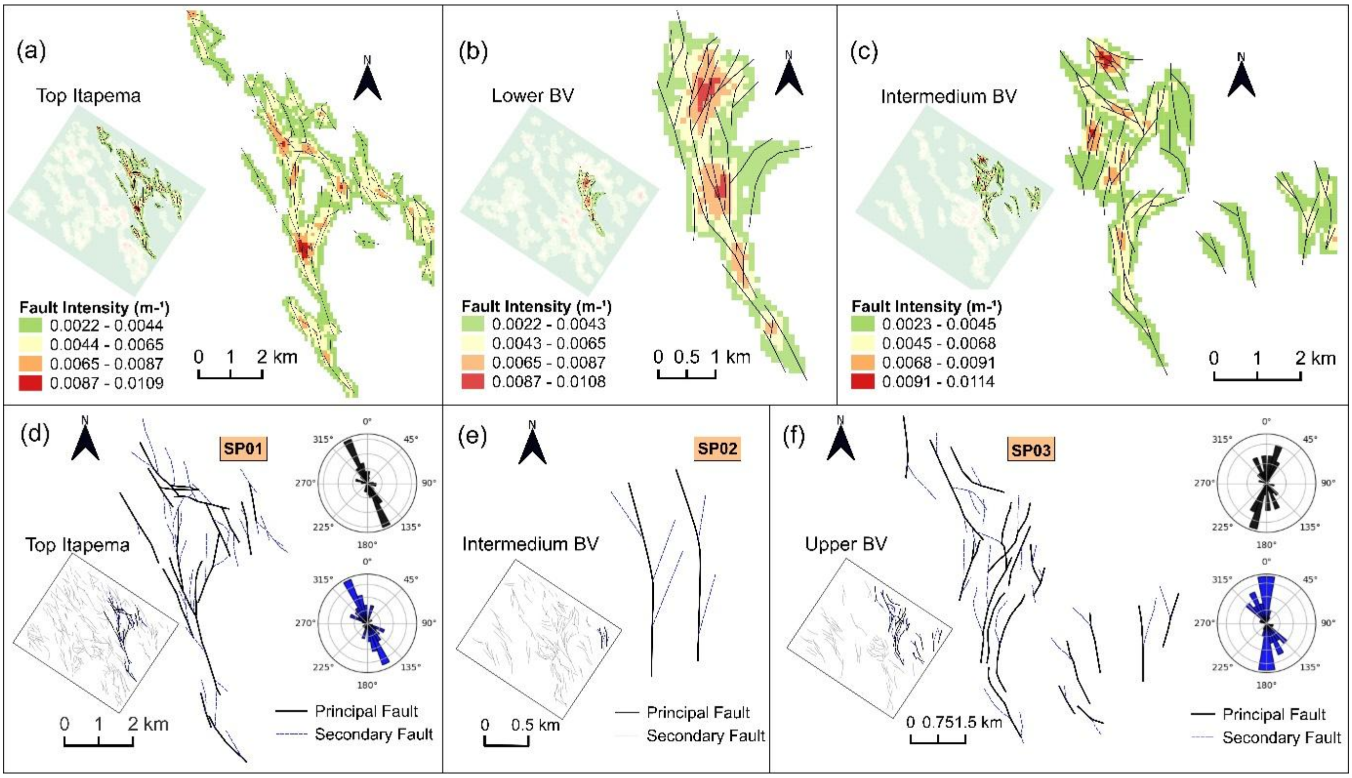

Figure 20: Classification of splay connectivity type. (a) The fault intensity map shows the splay pattern in the Top Itapema Horizon. (b) A tree-shaped splay pattern shows the alignment of high fault intensities on the LBV horizon. (c) Segregation of the splay pattern with less complex structures to the east in the IBV horizon. (d)

Splay pattern SP01: The major principal faults are oriented NW-SE, while secondary faults branch off from the principal fault as smaller segments oriented NNW-SSE. (e) Splay pattern SP02: A less complex structure where two principal faults branch with a Y-shaped geometry. (f) Splay pattern SP03: The principal faults are curved and rotated in the NNE-SSW direction, while the secondary faults remain oriented NW-SE.

The principal faults are primarily oriented NW-SE (**Figure 20**d), while secondary faults display a predominant NNW-SSE orientation, with some NNE-SSW orientations also observed. Branches generally originate at fault tips, forming Y-shaped junctions with the principal faults (SP02) (**Figure 20**e). Additionally, subordinate faults often branch along the walls of the principal faults, interacting with adjacent faults. This interaction enhances structural complexity, resulting in a tree-shaped branching geometry (SP01 and SP03) (**Figure 20**d, f). Toward the eastern portion of the study area, principal faults gradually shift to an NNE-SSW orientation (SP03), paralleling some secondary faults (**Figure 20**f).

The **linkage connectivity type** is predominantly found in structural highs and is characterized by elongated corridors of faults, primarily oriented in the NW-SE direction (**Figure 21**). This type consists of fault segments with similar strikes that are sequentially aligned and converge at connection points near their tips, where minor fault traces (approximately 400 meters long) merge to form a single, continuous fault structure with dimensions ranging from approximately 2 to 4 kilometers in length. In some areas, fault segments remain unlinked but aligned in parallel or subparallel orientations, forming en-echelon patterns (LK02) (**Figure 21e**). These patterns highlight a lateral displacement of faults, contributing to structural complexity. Fault intensity maps emphasize the high-intensity zones around connection points, contrasting with the lower intensity observed in unconnected segments (**Figure 21b**).

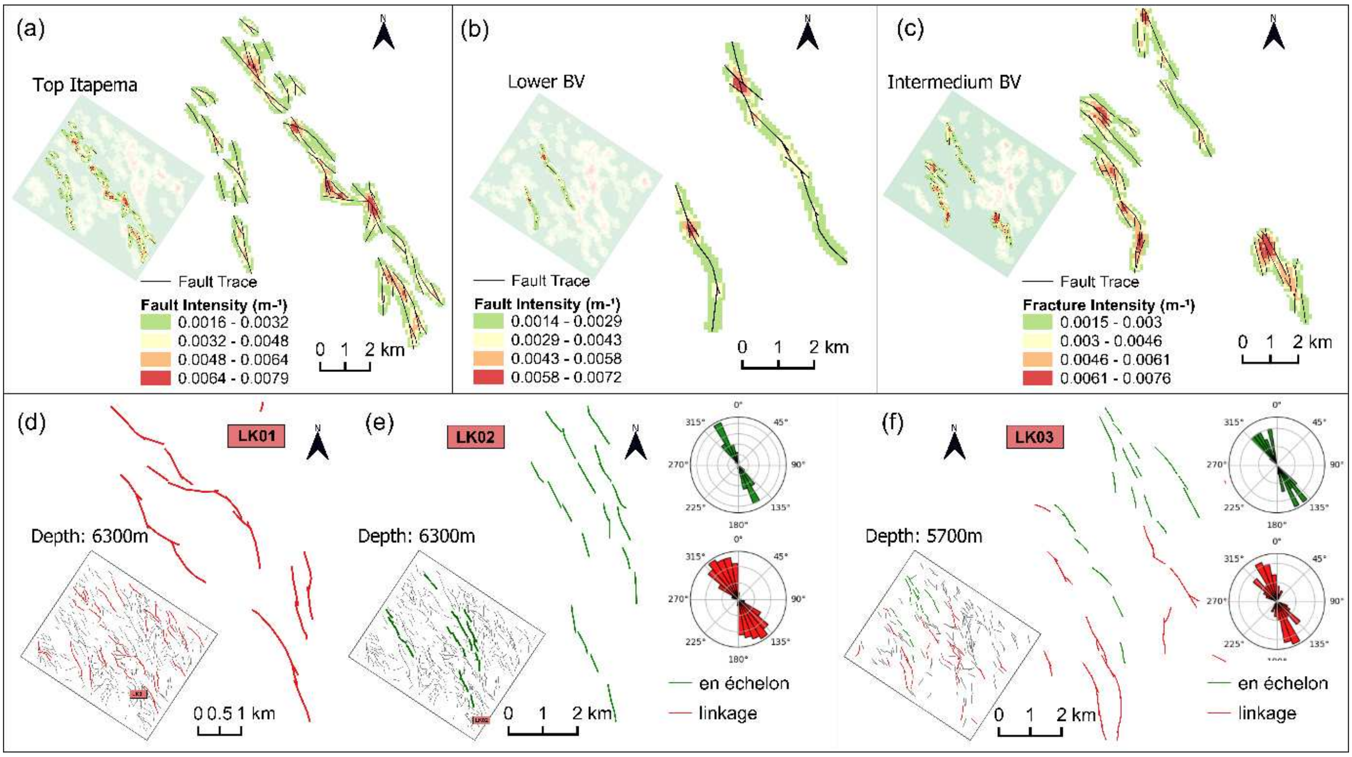

Figure 21: Classification of linkage connectivity type. (a) Linkage fault intensity in the Top Itapema Horizon forms elongated corridors oriented NW-SE. (b) High fault intensity areas surround the connection points where the faults link. (c) Linkage faults that are parallel and laterally interacting, forming zones of higher fault intensity. (d) Linkage pattern (LK01): minor faults linking to form major faults. (e) Unlinked fault segments (LK02) aligned parallel, oriented NW-SE, and slightly offset to the east, forming an en-echelon pattern. (f) Linkage and en-echelon patterns observed at a depth slice of 5700 m.

The **relay-ramp connectivity type** is characterized as an intermediate zone between structural highs and lower structural areas in the footwall and hanging wall of major faults (**Figure 22.a**). The relay pattern is parallel to the linkage connectivity type, which is situated at the top of structural highs. In contrast, the relay-ramp connectivity type is positioned along the inclined surfaces and structural lows of the study area.

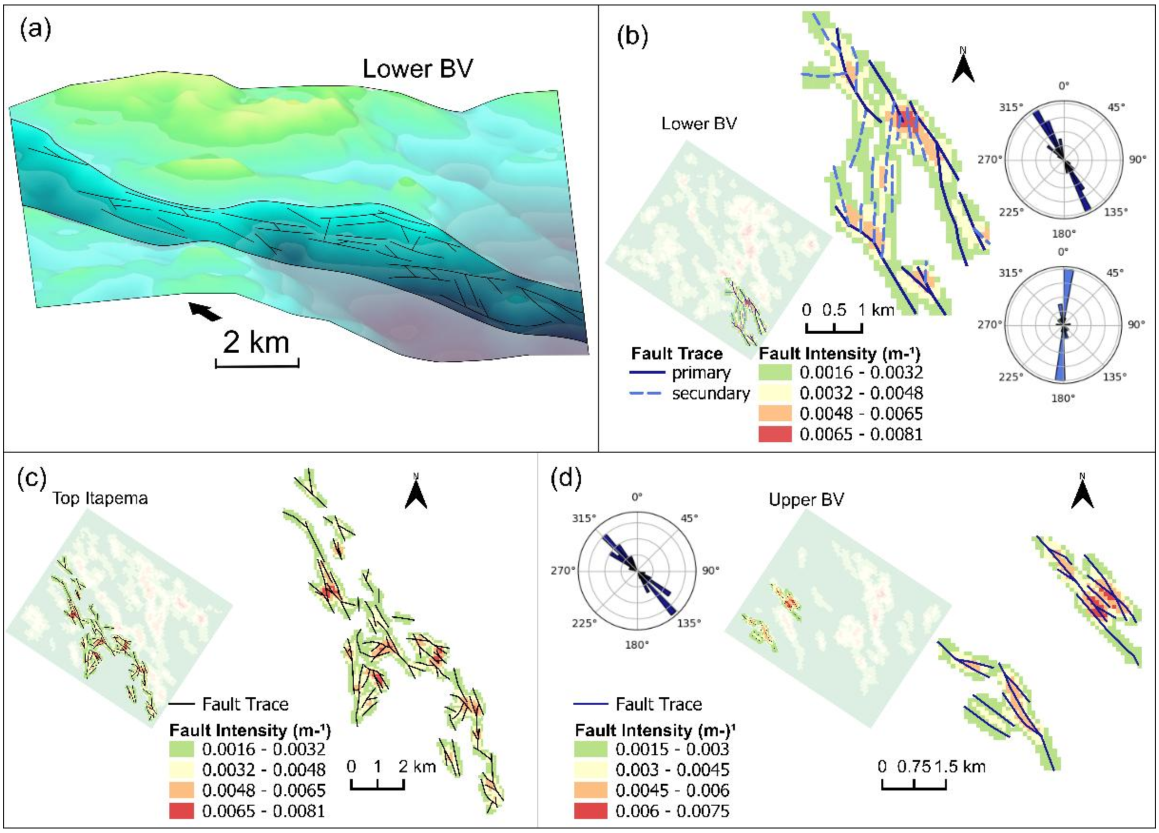

Figure 22: Classification of the relay-ramp connectivity Type. (a) LBV topography map highlighting the inclined region parallel to the structural high, oriented NW-SE. (b) The fault intensity map of the LBV Horizon reveals parallel principal faults in the hanging wall, with branching segments directed toward the top, and secondary faults form angles of 30° to 90° concerning the principal faults. (c) A fault intensity map of the Itapema Horizon highlights areas of high fault intensity and marks regions of fault interaction. (d) A fault intensity map of the UBV Horizon displays parallel principal faults, mostly isolated, with high fault intensity along segments branching in a Y-shaped geometry.

The principal faults (F1) are subparallel and aligned with the regional NW-SE structural trend, while secondary faults branch predominantly in the N-S direction. Fault segments marking the footwall of the principal faults exhibit branching towards the top, whereas in the hanging wall, secondary fault segments branch towards the base (**Figure 22b**). Fault intensity maps highlight the distinct branching patterns of relay ramps compared to the splay pattern. In splay structures, acute branching angles typically range from 5° to 30°, whereas in relay ramps, angles range between 40° and 90°, and can sometimes be obtuse (**Figure 22.b c.**). Despite principal faults generally lacking direct connections, the high density of faults marks a region of significant fault influence (**Figure 22.d**).

The **radial connectivity type** is identified exclusively in the IBV and UBV horizons and is located between the mounds associated with wells W01 and W02. The radial geometry consists of fault segments that are initially curvilinear and either isolated or display simple connectivity at the outer edges. Progressively, these segments become more rectilinear and exhibit increasingly complex connectivity towards the interior. The predominant orientation is NW-SE, but subordinate segments vary in multiple directions (**Figure 23.a. b**).

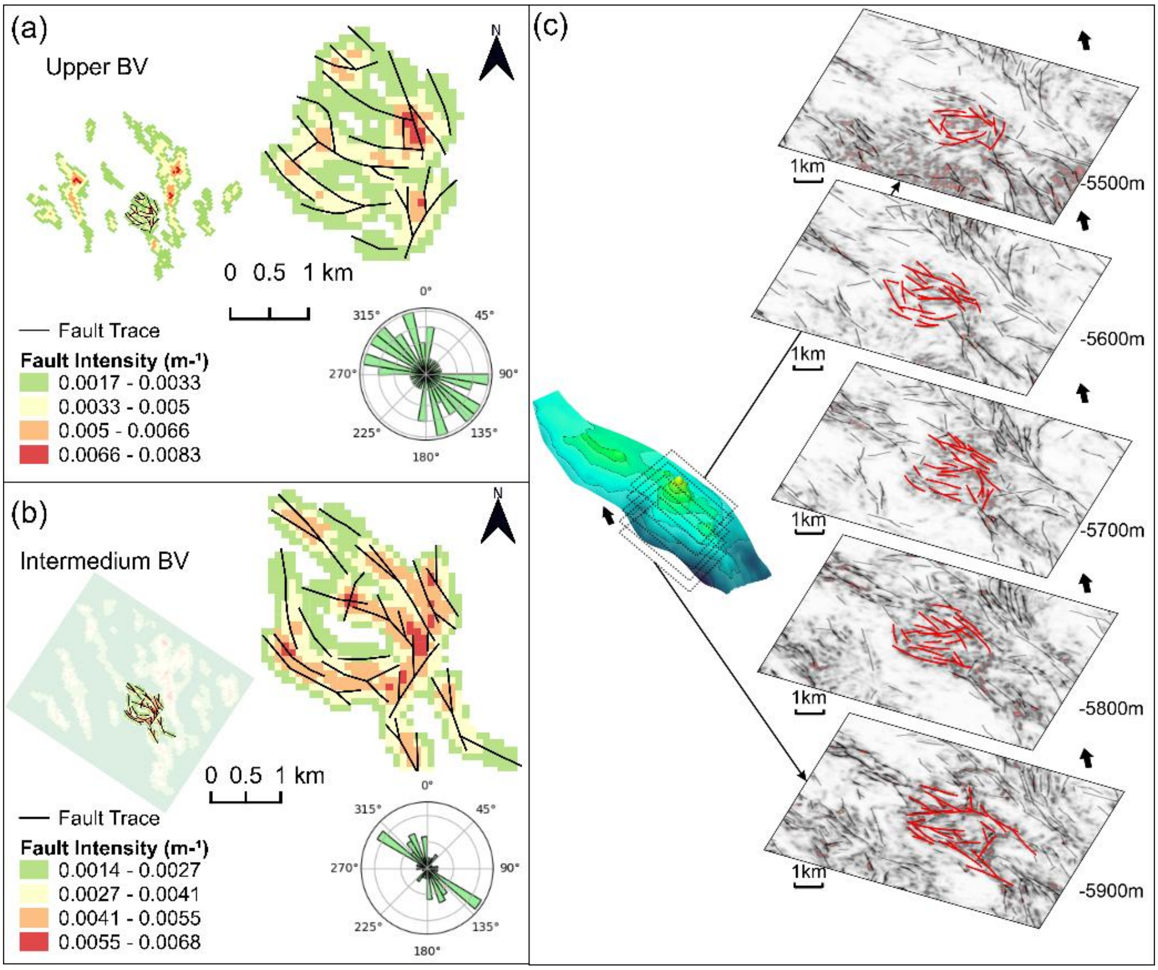

Figure 23: Classification of the radial connectivity type. (a) A faulty fault intensity map of the UBV Horizon shows a radial fault geometry with a predominant NW-SE orientation and multiple subordinate orientations. (b) Fault intensity map of the IBV Horizon, where fault segments transition from curvilinear at the outer edges of the radial geometry to more rectilinear with Y-shaped patterns toward the center. (c) Vertical representation with a depth slice illustrating the behavior of fault segments in the central portion of the study area. The basal depth slice reveals rectilinear segments that become progressively more complex and curvilinear as they approach the top.

A progressive change in fault segment patterns is observed from the base to the top of the reservoir. Initially, the faults are more rectilinear and interact, forming Y-shaped or linkage-type structures toward the center of the study area. As they approach the mound, the faults appear to deflect, creating inward and outward curves laterally. Towards the top, the remaining fault segments extend as rectilinear tails within the radial geometry. At the very top, these tails disappear, leaving the radial center isolated (**Figure 23.c**).

5.5. Connectivity types topology

From the results for topology parameters — nodes and branches proportion, connection per branch (CB) and average degree (D) —across four horizons: Itapema, Lower Barra Velha (LBV), Intermediate Barra Velha (IBV), and Upper Barra Velha (UBV), the following observations were made (***Table 1***):

Table 1: Topology analysis – node and branch count, proportions, average degree (D), and connections per branch (CB) for each horizon and connectivity zone.

Horizon	Node Count			Node Proportions			Branch Count			Branches Proportions			Connectivity	
	Count I	Count Y	Count X	I (%)	Y (%)	X (%)	Count I-I	Count I-C	Count C-C	I-I (%)	I-C (%)	C-C (%)	CB	D
GENERAL														
Itapema	360	104	4	76.92	22.22	0.85	70	220	54	20.35	63.95	15.70	0.95	1.47
LBV	389	123	5	75.23	23.79	0.99	62	264	62	15.98	68.04	15.98	1.00	1.50
IBV	224	38	3	84.53	14.34	1.13	37	149	33	16.89	68.04	15.07	0.72	1.65
UBV	146	56	2	71.57	27.45	0.98	17	111	32	10.63	69.38	20.00	1.09	1.57
SPLAY														
All Horizons	375	114	6	75.71	23.02	1.27	63	279	77	12.40	65.99	21.61	0.99	1.69
Itapema	154	44	4	76.38	21.82	1.80	49	126	36	20.65	61.13	18.23	0.98	2.09
LBV	89	25	2	76.93	21.61	1.46	6	45	22	6.64	56.53	36.82	0.96	1.26
IBV	63	20	1	75.00	23.81	1.19	2	14	4	1.00	73.52	26.48	1.01	0.48
UBV	69	25	0	73.40	26.60	0.00	6	94	15	4.33	79.19	16.48	1.04	2.45
LINKAGE														
All Horizons	419	102	3	79.96	19.47	0.61	68	208	35	16.50	69.88	13.61	0.86	1.19
Itapema	114	22	0	83.82	16.18	0.00	30	108	19	17.83	69.88	12.29	0.73	2.31
LBV	90	25	1	77.59	21.55	0.57	17	54	8	18.23	68.56	13.21	0.93	1.37
IBV	175	46	3	78.13	20.54	1.13	12	24	4	19.73	64.86	15.41	0.92	0.36
UBV	40	9	0	81.63	18.37	0.00	9	22	4	24.51	63.98	11.51	0.81	1.43
RELAY-RAMP														
All Horizons	254	79	4	75.41	23.48	1.10	47	215	59	14.78	67.66	17.55	1.00	1.91
Itapema	136	52	2	71.43	27.32	1.25	28	129	51	13.95	63.95	22.11	1.10	2.19
LBV	66	18	0	78.54	21.46	0.00	10	56	5	13.35	76.27	10.37	0.90	1.69
IBV	25	5	0	83.23	16.77	0.00	6	20	2	19.88	71.28	8.84	0.75	1.88
UBV	27	4	1	83.54	12.35	4.12	3	10	1	23.25	68.20	8.55	0.78	0.86
RADIAL														
All Horizons	71	26	1	72.65	26.60	0.75	9	42	10	12.68	71.01	16.32	1.07	1.25
IBV	43	12	1	77.15	21.53	1.32	5	25	4	11.10	77.46	11.43	0.95	1.22
UBV	28	14	0	66.67	33.33	0.00	4	17	6	13.14	69.13	17.73	1.20	1.29

In general, the horizons show a higher number of I-type nodes, ranging from 71.57% to 84.53%, followed by Y-type nodes (14.34% to 27.45%) and, to a lesser extent, X-type nodes, with occurrences around 1%. Regarding branches, the predominant connection type is

I-C (63.95% to 69.38%), followed by C-C (15.07% to 20%), with the lowest percentage corresponding to I-I (10.63% to 20.35%). Based on the CB parameter, the highest connectivity is found in the UBV horizon (1.09), while the lowest connectivity is in the IBV horizon (0.72). As for the D parameter, the highest degree of connectivity is observed in the UBV horizon (1.57), while the lowest is in the Itapema horizon (1.47).

Evaluating the results for connectivity types, we find that the Splay connectivity zones are primarily composed of isolated nodes and branches, while connected nodes and branches are more prominent in the IBV and UBV horizons. Additionally, the UBV horizon has the highest overall connectivity, with a high degree of integration (D = 2.45) and an intermediate connection per branch (CB = 1.04), as well as a high proportion of I-C (79.19%) and C-C (16.48%) connections.

The Linkage connectivity zones exhibit a connectivity per branch (CB <1) across all horizons. The highest CB value is observed in the LBV horizon (0.93), while the lowest is recorded in the Itapema horizon (0.73). However, the Itapema horizon demonstrates the highest average degree (D = 2.31), in contrast to the IBV horizon, which has the lowest overall connectivity (D = 0.36).

Based on the results for the relay ramp connectivity zones, the connectivity per branch across all horizons is 1.00, with Itapema showing the highest value (CB = 1.10) and IBV the lowest (CB = 0.78). The degree of connectivity decreases from the base to the top, with the highest degree of connectivity found in Itapema (D = 2.19) and the lowest in UBV (D = 0.86). Similarly, the number of connected nodes and branches is greater in the lower horizons.

The radial connectivity zone is observed exclusively in the IBV and UBV horizons. Compared to other connectivity zones, this zone exhibits a significantly higher percentage of connected nodes and branches, with Y-type nodes accounting for 23.53% to 33.33% and the sum of C-I and C-C branch types reaching 87% to 89%. The UBV horizon demonstrates the highest connectivity per branch (CB = 1.20), surpassing IBV (CB = 0.95). Furthermore, the degree of connectivity (D) is slightly higher in UBV (D = 1.29) compared to IBV (D = 1.22) (**Figure 24**).

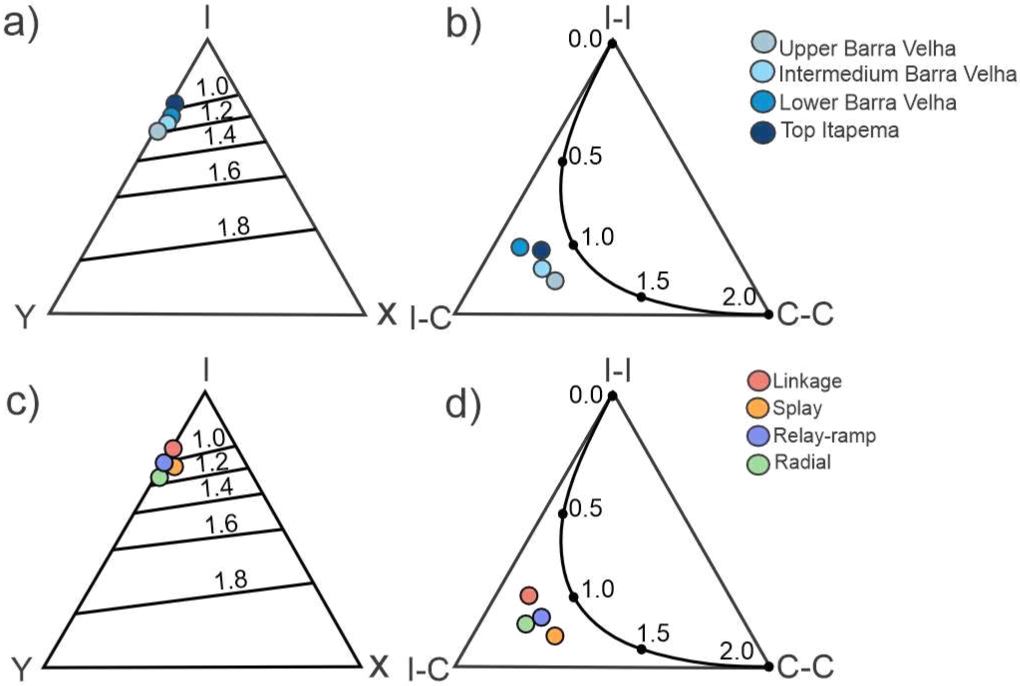

Figure 24: Triangle plots of topology parameters for each horizon and connectivity type. (a) Node proportion diagram and connections per branch (CB) for the Itapema, LBV, IBV, and UBV horizons. (b) Branch proportion diagram and connections per branch (CB) curve for the Itapema, LBV, IBV, and UBV horizons. (c) Node proportion diagram and connections per branch (CB) for the splay, linkage, relay ramp, and radial connectivity types. (d) Branch proportion diagram and connections per branch (CB) curve for the splay, linkage, relay ramp, and radial connectivity types.

5.6. 3D connectivity model

Following the NW-SE structural orientation and integrating the results from the structural model, connectivity type classification, and topology analysis for each identified class, a 3D connectivity model was developed for the Barra Velha reservoir. This model categorizes the 3d structural framework into five distinct connectivity domains, comprehensively representing fault connectivity within the reservoir (**Figure 25.b**).

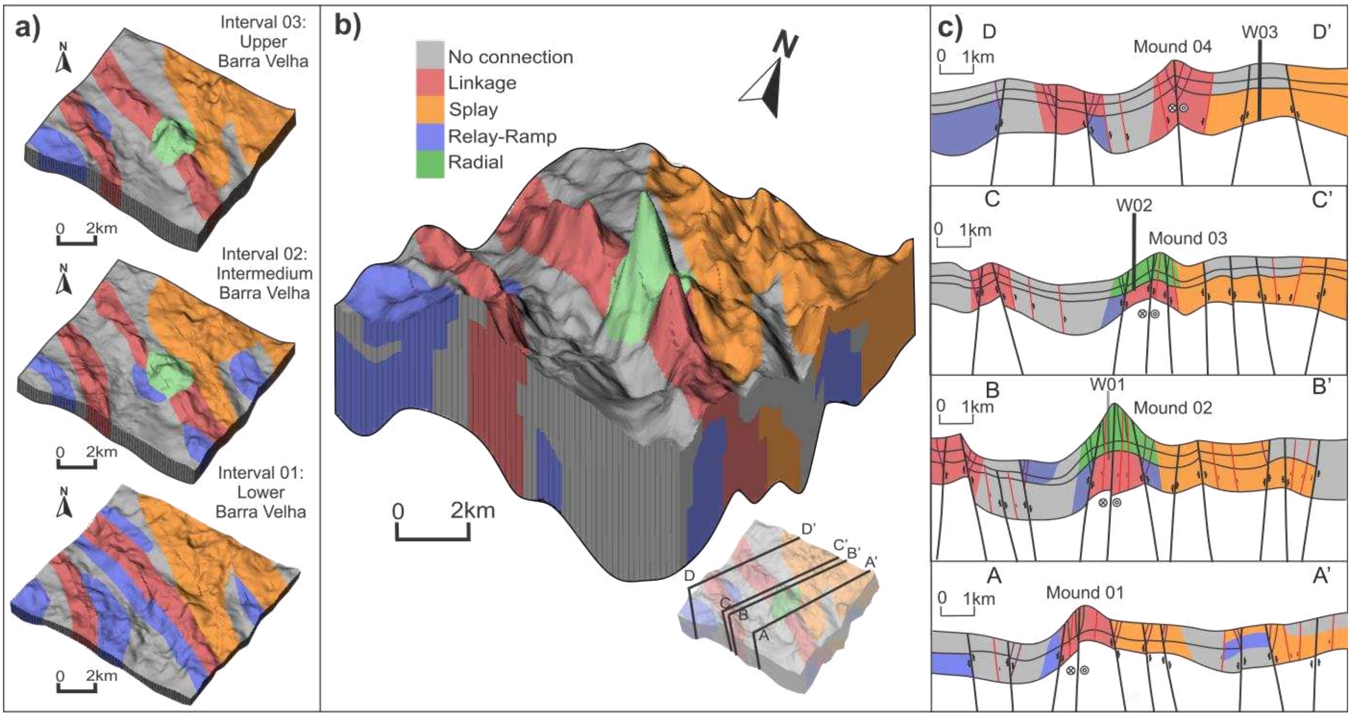

Figure 25: (a) Stratigraphic intervals of the Lower Barra Velha, Intermediate Barra Velha, and Upper Barra Velha. (b) 3D model combining connectivity zones, illustrating the horizontal and vertical distribution of connectivity types. (c) Mound profiles showing the different connectivity types within the mound structures.

Connectivity zones were analyzed within three successive stratigraphic intervals bounded, respectively, by the Itapema, LBV, IBV and UBV horizons. In the first interval, between the Top Itapema and LBV horizons, four distinct connectivity domains were mapped. The splay connectivity zone is the most extensive, occupying 30.23% of the study area and forming an NNE-SSW-trending structure defined by two converging eastern flanks dominated by acute-angle splay faults.

Surrounding this domain, the no-connection zone covers 26.12% of the area and coincides with structural lows where fault intensity is negligible, acting as a buffer that isolates fault-controlled networks. The relay-ramp zone, with 23.51% areal extent, trends NW–SE and is fragmented into three discrete corridors positioned between the linkage and no-connection domains. Finally, the linkage zone accounts for 20.14% of the interval and forms two NW–SE elongated corridors that inherit the geometry of coalescing faults, traversing the entire study area.

In the second interval, bounded by the LBV and IBV horizons, the structural pattern evolves markedly. The no-connection zone expands to 38.24% of the stratigraphic unit, becoming the dominant domain. Conversely, the splay connectivity zone diminishes to 26.17%, particularly in the south-eastern extremity, where it is pinched out between the linkage and no-connection domains. The linkage zone contracts to 19.64% and loses its former continuity, splitting into two shorter, discontinuous corridors separated by the emergence of a radial zone. The relay-ramp zone is reduced to 10.68% of the area and is uninterrupted only as a narrow NW-striking strip adjacent to the linkage corridors. The new radial zone occupies 5.28 % of the study area, forming a concentric, topographically positive feature in the central sector.

The third interval, between the IBV and UBV horizons, accentuates these trends. The no-connection zone reaches its maximum extent, covering 39.63% of the area. The splay connectivity zone stabilizes at 27.48%, waning towards the northeast but remaining prominent over eastern structural highs and regaining dominance near the southeastern margin. The linkage zone maintains the segmented configuration established in the preceding interval and now represents 21.36 % of the study area. The relay-ramp zone undergoes the most significant reduction, shrinking to 6.14 % and persisting only west of the main linkage corridor, while the radial zone contracts slightly to 5.39 %.

Taken together, the observations across successive stratigraphic intervals reveal a progressive shift from structurally controlled connectivity domains at the base to increasingly extensive no-connection areas higher in the section.

Four cross-sections (**Figure 25c**) were generated to intersect the main carbonate mounds and illustrate their vertical structural architecture.

- **Section A–A′** transects Mound 1, where a relay-ramp zone flanks a vertically continuous linkage zone located at the southwest (SW) and a splay zone to the northeast (NE). The vertical limits of these connectivity zones are defined by normal faults along the mound's margins.

- **Section B–B′** cuts Mound 2. Although lateral variations in connectivity are evident, vertical continuity persists: a basal dextral strike-slip fault delineates the linkage zone, which is flanked on both sides by relay-ramp zones terminated against normal faults. At the summit of the mound, a radial zone overlies the underlying linkage and relay-ramp domains.

- **Section C–C′** crosses Mound 3 and again reveals multiple connectivity domains. The basal linkage zone follows the strike-slip trend but abuts a relay-ramp zone to the SW and a normal-fault-bounded splay zone to the northwest (NW); a radial zone caps the mound.

- **Section D–D′** intersects Mound 4, whose structural style resembles that of Mound 1. A dextral strike-slip fault sustains vertical linkage continuity, the SW flank grades into a no-connection zone, and a normal fault on the NE side confines the basal contact with the splay zone.

Together, these sections highlight the systematic vertical persistence of linkage zones within the mounds and the contrasting lateral transitions to relay-ramp, splay, radial, and no-connection domains.

6. DISCUSSIONS

This chapter comprehensively analyzes the structural-tectonic evolution and fault connectivity within the study area, focusing on their implications for reservoir compartmentalization and fluid flow.

6.1. Structural conceptual model

The rifting process that gives rise to sedimentary basins such as the Santos Basin undergoes dynamic tensional and deformational stages, resulting in more or less complex structural configurations. Hierarchically, the regional structures formed during the initial opening of the basin continue to influence the organization and deposition of the overlying structural and stratigraphic units. These structures are referred to as inherited fabrics, which compose the structural framework of the basement.

The structural framework of the study area is characterized by NW-trending horsts and grabens, associated with the regional F1 fault set, which plays a key role in the transition between structural highs and lows. The F1 faults originated during the Rift Phase, aligning with the regional structural trend established during the opening of the basin. These faults exhibit kilometric lengths ranging from 2 to 4 km, with throw values varying between approximately 50 and 200 meters, which coincides with the LBV unit's stratigraphic thickness, at the reservoir's base.

Nevertheless, attributing the F1 fault set exclusively to an inherited basement fabric presumes a purely passive influence on basin evolution. Although the F1 faults nucleated during the rift phase, their persistence into the post-rift (UBV) interval probably reflects not only structural inheritance but also episodic reactivation driven by later, localized stress fields. Furthermore, the progressive reduction in displacement from the base to the top of the reservoir, evident in D–L plots, indicates that peak throw was achieved early in the fault’s history, after which deformation became progressively redistributed along the fault plane. This reduction suggests a decrease in vertical compartmentalization over time within the F1 fault zone.

In the seismic profiles, the F2 fault set is organized in a domino-style fault configuration, typical of extensional environments, where deformation is distributed among multiple smaller fault blocks that rotate to accommodate stretching and adjust to the newly created space (Axen, 1988; Geng et al., 2007; Naliboff et al., 2017). This structural configuration may generate multiple smaller compartments, potentially hydraulically isolated.

Another example of subsidiary structures formed during oblique-orthogonal rift opening is release faults. These faults are characterized as smaller normal faults that develop within the hanging wall block of a major fault, accommodating differential vertical movements within the same block without connecting separate fault segments (Destro, 1995). The F3 set occurs abutting the main normal fault planes in the extension relief direction. This set is associated with the late-stage rift stresses, acting as a mechanism to relieve local stresses during the deposition of the post-rift units.

As the primary fault evolves, stress rotation can increase the differential stress (σ_1-σ_3) until secondary faults become mechanically favorable, accommodating deformation (Perrin et al., 2015). Seismic profiles reveal that the F3 set branches from the top of F1, where stratigraphic blocks undergo displacement relative to the normal fault plane —a pattern observed in synthetic and antithetic branches, as described by Choi et al. (2016) and Nixon et al. (2020). As a result, these structures may either create preferential pathways for vertical migration or establish connectivity between distinct stratigraphic units.

Although the Santos Basin was primarily formed through oblique-extensional rifting, during the transition from rifting to post-rift phases in the Aptian, some areas of the basin exhibit signs of structural inversion. Studies such as those by Mendes et al. (2022) and Siqueira et al. (2024) describe how some regional normal faults may have been reactivated as reverse faults in reservoir fields within the central pre-salt polygon. This reactivation could have been driven by changes in the stress regime, including the introduction of local compressional or transtensional stresses. The F4 fault set, identified within the UBV interval, comprises subvertical, localized faults with an average length of approximately 500 meters, forming concentric and multidirectional geometries associated with the M02 and M03 mounds.

Structural inversion in the pre-salt has been well-documented, with evidence of syn-rift normal fault reactivation into strike-slip structures with transpressive and transtensional characteristics, particularly where N- and NE-trending faults converge (Alves et al., 2016). In these areas, normal faults from the syn-rift stage were inverted into low- and high-angle reverse faults, sometimes forming pop-up anticlines. These structures often crosscut syn-rift units, the main reservoir, and the base salt horizon, indicating that reactivation occurred after the reservoir was deposited. Additionally, significant erosion at the reservoir top suggests that tectonic inversion influenced sedimentation and structural evolution in this region.

These reactivation processes are consistent with global analogs of rift inversion. Studies show that larger normal faults (>25 m displacement) tend to accumulate fault gouge, which reduces friction and makes them more susceptible to reactivation than smaller faults. Moreover, fault connectivity plays a crucial role, as connected fault networks are more likely to be reactivated, whereas isolated faults tend to remain inactive (Kelly et al., 1999). Over time, these reverse-reactivated normal faults may begin to overlap, leading to the development of strike-slip faults to further accommodate displacement.

The structural evolution of the pre-salt reservoir in the study area results from the complex interplay between inherited rift structures, the development of subsidiary faults (F2, F3), and, critically, episodes of tectonic reactivation and inversion (F4) during the post-rift phase. These processes have generated a dynamic compartmentalization, where inherited faults may act as flow conduits or barriers, and reactivated or post-rift structures significantly alter connectivity and trap geometry.

6.2. Structural sectors

In the western portion of the study area, regional normal faults define a typical half-graben structure. The structural high is prominent, characterized by a continuous horst extending from the reservoir base to its top. This sector exhibits characteristics consistent with an orthogonal extensional rift aligned with the classical pure shear model. Additionally, the regional fault set has a significant influence on the reservoir's topographic transition, exhibiting relay ramp geometries. Stratigraphic thickness analyses reveal substantially thicker sedimentary layers adjacent to the western faults of the F1 set, with a progressive thinning from west to east.

In the central sector, the F1 fault set exhibits a subvertical orientation, with sedimentary onlap terminations defining a distinct structural high. Stratigraphic layers in this area are notably thinner compared to the western sector, suggesting a more complex deformation history where fault evolution extends beyond simple extensional processes. D-L plots further highlight a dextral strike-slip component, indicating additional oblique stress influences superimposed on extensional deformation.

This structural complexity is consistent with the presence of transfer zones, which mediate deformation between differently oriented rift segments. Such zones function as shear corridors during basin development, influencing both fault kinematics and regional stress distribution (Cooper & Warren, 2020). Within the Santos Basin, the Iracema Transfer Zone notably influenced stress redistribution during South Atlantic rifting and subsequent tectonic events, shaping the structural evolution of the study area.

In the eastern sector, fault orientations shift from NW-SE to N-S, accompanied by subsidiary NE-SW-oriented splay faults that branch at acute angles from the main faults. These splay faults significantly redistribute stresses within the fault systems (Scholz et al., 2009; 2011). Similar structural configurations are observed in the Iara-Iracema Transfer Zone (ZTI), which represents a structural inflection transitioning from NNE-trending faults to NNW trends. This shift highlights rift obliquity and the influence on fault system development. Eastern sector splay faults likely accommodated strike-slip displacement along NW-SE-oriented faults, effectively partitioning stress during oblique rifting (Araújo et al., 2024).

Aptian-aged structural inversions within the ZTI, characterized by dextral strike-slip movements (Araújo et al., 2024), correlate with NE-SW-oriented splay faults, which function as stress-relief structures that redistribute strain during phases of increased rift obliquity. These structures enhanced kinematic accommodation by forming step-overs, facilitating displacement transfer between major fault segments, and explaining localized uplift and subsidence, including sediment thinning atop inverted structural highs.

The vertical propagation observed in these splay faults suggests a multiphase deformation history within the ZTI, involving early normal faulting, subsequent strike-slip reactivation, and structural inversion. The F3 fault set likely preserves this tectonic evolution, recording the progressive influence of oblique stresses on the overall fault network.

Given the tectonic context involving strike-slip reactivation and structural inversions in the Aptian, the F4 fault set is unlikely to be a purely tectonic radial system. Instead, these faults may have served as conduits for hydrothermal fluid migration, thereby significantly contributing to the formation of carbonate mounds. Radial fault geometries appear strongly associated with hydrothermal and late volcanic processes driven by thermal gradients and fluid overpressure, rather than solely by tectonic reactivation.

The observed concentric and radial fault geometries align closely with hydrothermal venting mechanisms, where magmatic fluids migrate vertically through fault-controlled conduits. Such processes typically produce dome-shaped features characterized by chaotic seismic reflectors, a signature indicative of hydrothermal systems (Plank et al., 2005; Hanssen et al., 2006; Alvarenga et al., 2016).

Synthesizing these sector-specific structural characteristics, the proposed structural-tectonic model delineates a multiphase evolutionary history, beginning with the development of early normal faults, which are subsequently overprinted by strike-slip deformation and structural inversion (**Figure 26**).

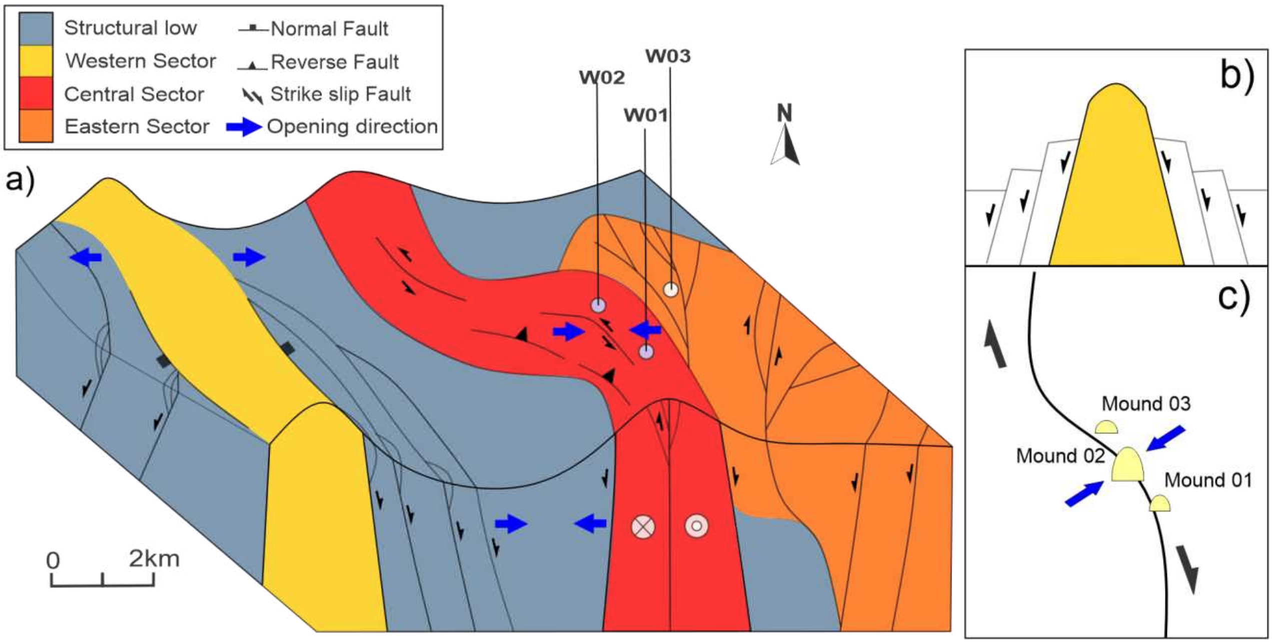

Figure 26: (a) Structural-tectonic model of the study area, subdivided into Western, Central, and Eastern sectors. Fault orientations and kinematics indicate interactions among extensional, strike-slip, and inversion tectonics, controlling the structural framework. (b) Orthogonal extensional half-graben structure in the western sector, analogous to the pure shear model proposed by McKenzie (1978). (c) Diagram illustrating the transpressional structure in the central sector. The dextral displacement along the smoothed "S"-shaped structure induces stress concentration, generating transpressional deformation along its curvature, where the primary carbonate mounds (Mound 01; Mound 02, and Mound 03) are situated. Blue arrows highlight areas of intensified compression and mound formation.

The western sector is predominantly characterized by normal faulting and relay transfer zones, with pronounced variations in sedimentary thickness. The central sector displays clear evidence of tectonic inversion and strike-slip reactivation associated with the ZTI and subsequent Neogene compressional events, resulting in reverse-reactivated normal faults and pop-up structures. The eastern sector exhibits oblique rifting dynamics, with splay faults accommodating stress and significantly influencing the sedimentary architecture, which may facilitate the migration of hydrothermal fluids.

Throughout the entire study area, the ZTI emerges as critical in redistributing stresses, shaping fault segmentation, facilitating relay ramp formation, and mediating interactions between transpressional and extensional regimes. Furthermore, the integration of splay faults and hydrothermal conduits underscores a complex deformation history, highlighting fault connectivity as essential in controlling fluid flow, sediment deposition patterns, and structural evolution within the pre-salt reservoirs of the Santos Basin.

6.3. Fault connectivity and reservoir implications

The four connectivity types (splay, linkage, relay-ramp, and radial) reflect dynamic fault interaction patterns correlated with the structural evolution of the study area. The classification based on geometry, orientation, and topology (e.g., CB and D parameters) demonstrates that fault system complexity varies across stratigraphic horizons (Itapema, LBV, IBV, UBV) and stratigraphic units, suggesting differentiated tectonic and lithological controls.

- **Splay Connectivity**:

The splay connectivity zones in the study area reflect an evolving structural system where splay faults (secondary branches) develop due to stress redistribution around major faults (F1), particularly in transtensional regimes that combine shear and extensional deformation. As the main fault accumulates displacement, the adjacent rock undergoes strain localization, forming zones of weakness that facilitate the propagation of secondary faults at acute angles (10°–45°). This phenomenon is well-documented in shear zones and rift systems (Fossen et al., 2010), where splay faults accommodate deformation by dispersing stress away from the primary fault plane.

The observed propagation of secondary faults (F2/F3) at acute angles results in Y-shaped patterns and branching fault geometries, commonly described as tree-like structures. These splays influence fault connectivity by creating relay zones, where deformation is distributed across multiple fault segments, thereby enhancing the overall fault connectivity.

In the eastern sector, the transition to NNE-SSW fault orientations and the parallelism between primary and secondary faults suggest that localized heterogeneities or stress field rotations play a role in controlling splay fault development. This is particularly relevant in areas influenced by transfer zones, where pre-existing basement structures guide the propagation of faults.

- **Linkage Connectivity**:

The classification of the linkage connectivity type illustrates the process of fault segment growth and connection as they propagate and begin to interact with the stress fields of neighboring faults (Peacock & Sanderson, 1991; Peacock, 2002). Fault linkage is a gradual process that does not always result in a single, continuous fault plane. In many cases, fault segments may remain partially independent after linkage, resulting in non-linear D-L profiles characterized by displacement minima coinciding with the former segment boundaries (Cartwright et al., 1995; Mansfield & Cartwright, 2001).

The high fault density at connection points reinforces the idea that these regions act as critical zones for the nucleation of larger faults, serving as focal points for stress concentration. Additionally, *en-échelon* patterns are characteristic of faults in intermediate growth stages, where mechanical interaction between segments modifies displacement gradients and promotes progressive linkage. The low connectivity values (CB < 1) suggest incomplete fault coalescence, a common phenomenon in progressive deformation regimes (Fossen & Rotevatn, 2016; Peacock et al., 2017).

- **Relay-ramp Connectivity**:

The relay-ramp fault network plays a crucial role in maintaining vertical fault connectivity. These zones serve as primary connections between the base of the reservoir and the overlying structural units due to their high fault and fracture density, varied structural orientations, and increased complexity, which facilitates interaction between different subsurface compartments (Fossen & Rotevatn, 2016).

Therefore, relay ramps are of great importance in the study of economically significant accumulations of oil and gas, hydrothermal solutions, and geomechanics since they can compromise reservoir sealing or lead to potential fluid leakage (Gartrell et al., 2004; Kristiansen, 2011). Furthermore, due to their control over fluid flow, relay ramps also influence diagenetic processes, affecting the distribution of cement along faults (Eichhubl et al., 2009) and structurally controlled dolomitization (Sharp et al., 2010).

In the proposed model, relay-ramp zones, characterized by high fault density and branching angles of 40°–90°, are observed adjacent to linkage and splay connectivity types, forming a transitional zone within the fault network. However, toward the top of the reservoir, the occurrence of relay-ramp structures diminishes, primarily due to their lower natural structural occurrence and the increased compartmentalization of the fault framework into specific connectivity zones.

- **Radial Connectivity**:

Radial connectivity zones are confined to the IBV and UBV horizons, where the variation in fault orientations (predominantly NW-SE with subsidiary segments in multiple directions) between the mounds at W01/W02 suggests localized deformation. This is likely driven by fluid pressure and thermal expansion associated with hydrothermal vents. The injection of high-pressure fluids from these vents can induce radial fracturing through hydraulic fracturing, independent of the regional stress field. Additionally, the heat from hydrothermal fluids causes differential rock dilation around the mounds, generating tangential stresses and promoting thermo-fracturing (Planke et al., 2005; Hansen et al., 2016; Alvarenga et al., 2016).

Hydrothermal activity in the pre-salt is commonly associated with post-rift or late-rift stages (Alves et al., 2016), while evidence of transpressive tectonics suggests it may have also occurred during rifting. The persistence of radial connectivity at the UBV horizon indicates ongoing hydrothermal processes in later stages of deformation.

The connectivity analysis of radial zones supports a hydraulic fracturing and fluid ascension process, where hydrothermal fluids migrate along preexisting NW-SE faults, forming mounds. Fluid pressure generates radial fractures at mound edges, which, as they propagate and interconnect, form rectilinear Y-shaped networks. Additionally, strike-slip reactivation enhances fault connectivity ($D = 1.22$ to 1.29). These findings underscore the pivotal role of hydrothermal processes in shaping fault evolution, connectivity, and reservoir compartmentalization, thereby influencing potential hydrocarbon migration pathways.

The interaction between these connectivity types determines the degree of vertical and horizontal compartmentalization within the reservoir. Splay and linkage zones primarily enhance horizontal connectivity, promoting possible lateral fluid pathways along fault corridors. Relay-ramp zones provide critical vertical pathways, linking deeper and shallower units, while radial connectivity, driven by hydrothermal processes, introduces additional structural complexity that modulates both vertical and horizontal connections. Understanding these connectivity patterns is essential for predicting fluid flow behavior, identifying high-permeability pathways, and assessing potential compartmentalization within the reservoir.

However, it is essential to note that the interpretations presented are primarily based on seismic-scale and structural evidence. Geomechanical behavior, fluid properties, and reservoir matrix characteristics are critical for validating and corroborating the connectivity patterns observed in each zone. Despite the apparent structural connections identified in the seismic data, these zones may be cemented, experience permeability reduction due to diagenetic alterations, or be affected by stress-related sealing mechanisms. Moreover, factors such as mineral precipitation, pressure and temperature regimes, or variations in fracture aperture and infill can significantly impair effective hydraulic connectivity. Therefore, the integration of core analysis, well log data, and geomechanical modeling is essential to confirm the functional role of these fault-related zones as either conduits or barriers to fluid flow.

6.3. 3D connectivity modeling and further steps

The next step of this study will involve developing a Discrete Fracture Network (DFN) model based on the defined connectivity zones. These connectivity domains will guide the discretization of the simulation grid, ensuring higher resolution in homologous faulted regions while disregarding areas where no fault evidence is observed in the study area. This approach aims to optimize computational efficiency while maintaining geological accuracy in fracture modeling.

Additionally, the methodology will be validated through comparison with dynamic reservoir simulations and production data, assessing its performance against the classical approach commonly used in fractured reservoir modeling. This validation will highlight the advantages of the connectivity-based framework in capturing structural complexity and improving flow predictions. Furthermore, potential limitations will be identified and addressed, refining the methodology to enhance its applicability to different geological settings.

Future work will also explore the integration of geomechanical and permeability analyses to refine fault transmissibility predictions and evaluate the impact of fault-related compartmentalization. Machine learning techniques may be incorporated to automate fault detection and connectivity classification, further improving efficiency and reducing interpretation bias. By systematically comparing the proposed method with conventional reservoir modeling approaches, this study aims to provide a robust, scalable framework for enhancing fracture network representation and optimizing hydrocarbon recovery strategies.

7. CONCLUSIONS

The study highlights the critical role of fault connectivity in the structural complexity and flow dynamics of pre-salt reservoirs. By analyzing faults in the Barra Velha Formation, four primary connectivity types were identified: splay, linkage, relay-ramp, and radial, each influencing reservoir compartmentalization and fluid flow in distinct ways.

These connectivity zones help justify and refine our structural interpretation by revealing how fault interactions influence both horizontal and vertical fluid pathways. Splay and linkage zones, for example, are critical in promoting lateral connectivity, which can facilitate rapid pressure communication and potential cross-flow between compartments. In contrast, relay-ramp zones play a crucial role in providing vertical connections, enabling fluids to migrate between deeper and shallower units. The radial zones, often associated with hydrothermal activity, introduce additional complexity by enabling localized vertical conduits that may bypass otherwise isolated compartments.

In practical terms, incorporating these zones into reservoir models improves the representation of fault networks and reduces uncertainties related to fault transmissibility and compartmentalization. By defining areas with high connectivity, modelers can implement refined grid discretization strategies, focusing on higher resolution where fluid flow is most sensitive to structural architecture. Conversely, no-connection zones can be simplified, optimizing computational resources without compromising geological accuracy.

Furthermore, these connectivity zones provide a robust framework for calibrating transmissibility multipliers and defining dynamic flow barriers or conduits in simulation models. This directly supports more accurate predictions of pressure behavior, sweep efficiency, and overall production performance. The connectivity-based approach also enhances the design of well placement strategies, aiding in the identification of optimal targets while avoiding zones prone to premature breakthrough or poor drainage.

However, some limitations should be recognized. The identification and classification of connectivity zones are primarily based on seismic-scale data, which may overlook smaller-scale faults or fractures that can critically impact local fluid flow. Additionally, seismic interpretation is inherently limited by resolution and attribute uncertainties, which can affect the accuracy of mapped fault geometries and their connectivity patterns. The actual hydraulic behavior of faults is also influenced by factors not fully captured in structural models, such as cementation, diagenetic alterations, and variable fracture apertures, which may reduce effective permeability even in structurally connected zones.

Therefore, while connectivity zones offer a powerful tool to bridge detailed structural interpretation and dynamic simulation, their application should be complemented with core data, well log analyses, and geomechanical studies to validate their hydraulic significance. By acknowledging these limitations, future studies can further refine connectivity models and enhance their predictive reliability in reservoir management.

Regarding the key questions presented at the beginning of this study, the respective findings are described as follows:

1. **What are the primary connectivity patterns, and how do they influence horizontal and vertical connections that might impact potential fluid pathways?**

- Four major connectivity patterns were identified: splay, linkage, relay-ramp, and radial connectivity.
- Splay and linkage connectivity enhance horizontal connections, promoting lateral fluid pathways along fault corridors.
- Relay-ramp connectivity is crucial for vertical fluid movement, creating connections between different stratigraphic units.
- Radial connectivity, associated with hydrothermal processes, introduces localized structural complexity, influencing both vertical and horizontal connectivity.
- These patterns highlight that fault connectivity is highly dependent on structural positioning and fault interactions, directly impacting permeability and flow pathways.

2. **How do different fault sets interact within the reservoir to control fault connections and structural compartmentalization in the Barra Velha Formation?**

- The F1 fault set (regional normal faults) acts as the main structural control, defining horsts, grabens, and relay zones.
- The F2 fault set (secondary normal faults) parallel to F1 and typically confined to the reservoir interval, forms domino-style arrays that subdivide compartments horizontally and create smaller, potentially isolated blocks.
- The F3 fault set (splay and linking faults) serves to redistribute stresses and create relay zones, enhancing both vertical and lateral connectivity locally, but also introducing internal complexities that fragment compartments.

- The F4 fault set (radial faults) is linked to hydrothermal venting and stress redistribution, playing a role in mound formation and fault-related fluid migration.
- Fault reactivation and segmentation trends reveal that some normal faults experienced tectonic inversion, transitioning into strike-slip or transpressional features, which further modified the connectivity and compartmentalization within the reservoir.

3. How can connectivity zones be integrated into reservoir modeling to improve geological representation and simulation accuracy?

- A 3D connectivity model was developed, defining five distinct connectivity zones: Splay, Linkage, Relay-Ramp, Radial, and No Connection zones.
- These zones help refine the simulation grid, allowing for higher resolution where connectivity is high (e.g., splay or linkage zones) and lower resolution or simplified treatment in no-connection areas. This balances computational efficiency and geological accuracy.
- The model enables optimized upscaling and downscaling strategies, ensuring higher resolution in key connectivity areas while maintaining computational efficiency.
- Future work will involve incorporating the connectivity model into Discrete Fracture Network (DFN) simulations to validate its impact on flow predictions and production performance.
- The integration of machine learning techniques for fault detection and connectivity classification is a potential next step to improve efficiency further and reduce interpretation bias.

REFERENCES

1. Adriano, M. S., Figueiredo, J., Coelho, P. H. G. R., & Borghi, L. (2022). Tectonic and stratigraphic evolution of the Santos Basin rift phase: New insights from seismic interpretation on Tupi oil field area. In Journal of South American Earth Sciences (Vol. 116, p. 103842). Elsevier BV. https://doi.org/10.1016/j.jsames.2022.103842

2. Alvarenga, R. S., Iacopini, D., Küchle, J., Scherer, C. M. dos S., & Goldberg, K. (2016). Seismic characteristics and distribution of hydrothermal vent complexes in the Cretaceous offshore rift section of the Campos Basin, offshore Brazil. In Marine and Petroleum Geology (Vol. 74, p. 12). Elsevier BV. https://doi.org/10.1016/j.marpetgeo.2016.03.030

3. Alves, T. M., Fetter, M., Lima, C., Cartwright, J. A., Cosgrove, J., Gangá, A. O., Queiroz, C., & Strugale, M. (2016). An incomplete correlation between pre-salt topography, top reservoir erosion, and salt deformation in deep-water Santos Basin (SE Brazil). In Marine and Petroleum Geology (Vol. 79, p. 300). Elsevier BV. https://doi.org/10.1016/j.marpetgeo.2016.10.015

4. Araújo, M. N., Rigoti, C. A., Romeiro, M. A., Viana, A., & Szatmari, P. (2024). Evolução tectônica da margem rifteada sudeste do Brasil – Do Gondwana ao Atlântico Sul (p. 239). Copyright (c) 2024 Programa de Editoração de Livros Didáticos da Universidade Petrobras Detalhes sobre o formato disponível para publicação: PDF. https://publicacoesup.petrobras.com.br/peld/catalog/view/12/50/68

5. Araújo, C. C. de; Madrucci, V.; Moretti Júnior, P. A.; Silva Filho, R. P.; Spadini, A. R.; Homewood, P.; Mettraux, M.; Ramnani, C. W. Capitulo 8: Estratigrafia e modelos deposicionais carbonáticos do Pré-sal da Bacia de Santos. In: *Livro Didático da Universidade Petrobras*. Rio de Janeiro: Programa de Editoração de Livros Didáticos da Universidade Petrobras, 2024. ISBN 978-65-88763-25-4.

6. Axen, G. J. (1988). The geometry of planar domino-style normal faults above a dipping basal detachment. In Journal of Structural Geology (Vol. 10, Issue 4, p. 405). Elsevier BV. https://doi.org/10.1016/0191-8141(88)90018-1

7. Azeredo, A. C.; Duarte, L. V.; Silva, A. P.. The challenging carbonates from the Pre-Salt reservoirs offshore Brazil: facies, palaeoenvironment and diagenesis. **Journal Of South American Earth Sciences**, [S.L.], v. 108, p. 103202, jun. 2021. Elsevier BV. http://dx.doi.org/10.1016/j.jsames.2021.103202.

8. Babaei, M., & King, P. R. (2012). A Modified Nested-Gridding for Upscaling–Downscaling in Reservoir Simulation. In Transport in Porous Media (Vol. 93, Issue 3, p. 753). Springer Science+Business Media. https://doi.org/10.1007/s11242-012-9981-4

9. Barenblatt, G.I; Zheltov, Iu.P; Kochina, I.N. Basic concepts in the theory of seepage of homogeneous liquids in fissured rocks [strata]. **Journal Of Applied Mathematics And Mechanics**, [S.L.], v. 24, n. 5, p. 1286-1303, jan. 1960. Elsevier BV. http://dx.doi.org/10.1016/0021-8928(60)90107-6.

10. Barnett, A., Obermaier, M., Amthor, J. E., Sharafodin, M., Bolton, M., Clarke, D. B., & Câmara, R. (2021). Chapter 6: Origin and Significance of Thick Carbonate Grainstone Packages in Nonmarine Successions: A Case Study from the Barra Velha Formation, Santos Basin, Brazil (p. 155). https://doi.org/10.1306/13722318msb.6.1853

11. Biemiller, J., Gabriel, A., & Ulrich, T. (2023). Dueling dynamics of low-angle normal fault rupture with splay faulting and off-fault damage. In Nature Communications (Vol. 14, Issue 1). Nature Portfolio. https://doi.org/10.1038/s41467-023-37063-1

12. Bjørlykke, Knut (ed.). Petroleum Geoscience: from sedimentary environments to rock physic. **Springer Heidelberg New York Dordrecht London**, [S.L.], v. 2, p. 1-666, 2015. Springer Berlin Heidelberg. http://dx.doi.org/10.1007/978-3-642-34132-8.

13. Blaskovish, F. T.; Cain, G. M.; Sonier, Fernand; Waldren, David; Webb, S. J.. A Multicomponent Isothermal System for Efficient Reservoir Simulation. **Middle East Oil Technical Conference And Exhibition**, [S.L.], 14 mar. 1983. SPE. http://dx.doi.org/10.2118/11480-ms.

14. Buckley, J. P., Bosence, D., & Elders, C. (2015). Tectonic setting and stratigraphic architecture of an Early Cretaceous lacustrine carbonate platform, Sugar Loaf High, Santos Basin, Brazil. In Geological Society London Special Publications (Vol. 418, Issue 1, p. 175). Geological Society of London. https://doi.org/10.1144/sp418.13

15. Caine, J. S., Evans, J., & Forster, C. B. (1996). Fault zone architecture and permeability structure. *Geology*, *24*(11), 1025–1028. https://doi.org/10.1130/0091.

16. Carle, S.F., Fogg, G.E. Transition probability-based indicator geostatistics. *Math Geol* **28**, 453–476 (1996). https://doi.org/10.1007/BF02083656.

17. Carvalho, A. M. A.; Hamon, Y.; Souza Junior, O. G. de; Carramal, N. G.; CollardO, N. Facies and diagenesis distribution in an Aptian pre-salt carbonate reservoir of the Santos Basin, offshore Brazil: a comprehensive quantitative approach. **Marine And Petroleum Geology**, [S.L.], v. 141, p. 105708, jul. 2022. Elsevier BV. http://dx.doi.org/10.1016/j.marpetgeo.2022.105708.

18. Castro, R. D. de; Picolini, J. P. Main features of the Campos Basin regional geology. **Geology And Geomorphology**, [S.L.], p. 1-12, 2016. Elsevier. http://dx.doi.org/10.1016/b978-85-352-8444-7.50008-1.

19. Celini, N.; Pichat, A.; Ringenbach, J. C. Salt tectonics synchronous with salt deposition in the Santos Basin (Ariri Formation, Brazil). **Earth And Planetary Science Letters**, [S.L.], v. 641, p. 118853, set. 2024. Elsevier BV. http://dx.doi.org/10.1016/j.epsl.2024.118853.

20. Cherpeau, Nicolas, Caumon, Guillaume, and Bruno Lévy. "Stochastic Simulation of Fault Networks From 2D Seismic Lines." Paper presented at the 2010 SEG Annual Meeting, Denver, Colorado, October 2010.

21. Choi, J., Edwards, P., Ko, K., & Kim, Y. (2015). Definition and classification of fault damage zones: A review and a new methodological approach [Review of Definition and classification of fault damage zones: A review and a new methodological approach]. Earth-Science Reviews, 152, 70. Elsevier BV. https://doi.org/10.1016/j.earscirev.2015.11.006

22. Coleman, A. J., Jackson, C., Duffy, O. B., & Nikolinakou, M. A. (2018). How, where, and when do radial faults grow near salt diapirs? In Geology (Vol. 46, Issue 7, p. 655). Geological Society of America. https://doi.org/10.1130/g40338.1

23. Cooper, M. A., & Warren, M. J. (2020). Inverted fault systems and inversion tectonic settings. In Elsevier eBooks (p. 169). Elsevier BV. https://doi.org/10.1016/b978-0-444-64134-2.00009-2

24. Cordero, Julio Alberto Rueda; Sanchez, Eleazar C Mejia; Roehl, Deane. Integrated discrete fracture and dual porosity - Dual permeability models for fluid flow in deformable fractured media. **Journal Of Petroleum Science And Engineering**, [S.L.], v. 175, p. 644-653, abr. 2019. Elsevier BV. http://dx.doi.org/10.1016/j.petrol.2018.12.053.

25. Dehler, N., Yamato, A. A., Cruz, F. E., & Moretti Júnior, P. A. (2024). (p. 395). Copyright (c) 2024 Programa de Editoração de Livros Didáticos da Universidade Petrobras Detalhes sobre o

formato disponível para publicação: PDF. https://publicacoesup.petrobras.com.br/peld/catalog/view/12/44/61

26. Destro, Nivaldo. Release fault: a variety of cross fault in linked extensional fault systems, in the sergipe-alagoas basin, ne brazil. **Journal Of Structural Geology**, [S.L.], v. 17, n. 5, p. 615-629, maio 1995. Elsevier BV. http://dx.doi.org/10.1016/0191-8141(94)00088-h.

27. Deutsch, C.V. and Journel, A.G., (1998). GSLIB Geostatistical Software Library and User's Guide, Oxford University Press, New York, second edition. 369 pages.

28. Deutsch, C. V. (2005). Geostatistical Reservoir Modeling. In Technometrics (Vol. 47, Issue 4, p. 527). Taylor & Francis. https://doi.org/10.1198/tech.2005.s339

29. Ding, Y., and P. Lemonnier. "Use of Corner Point Geometry in Reservoir Simulation." Paper presented at the International Meeting on Petroleum Engineering, Beijing, China, November 1995. doi: https://doi.org/10.2118/29933-MS

30. Duffy, O. B., Nixon, C. W., Bell, R., Jackson, C., Gawthorpe, R. L., Sanderson, D. J., & Whipp, P. S. (2017). The topology of evolving rift fault networks: Single-phase vs multi-phase rifts. In Journal of Structural Geology (Vol. 96, p. 192). Elsevier BV. https://doi.org/10.1016/j.jsg.2017.02.001

31. Elmo D, Stead D, Rogers S (2015) Guidelines for the quantitative description of discontinuities for use in discrete fracture network modelling. In: ISRM congress, ISRM-13CONGRESS.

32. Elmo D, Stead D (2010) An integrated numerical modelling–discrete fracture network approach applied to the characterisation of rock mass strength of naturally fractured pillars. Rock Mech Rock Eng 43:3–19.

33. Ellis, M. A., & Dunlap, W. J. (1988). Displacement variation along thrust faults: implications for the development of large faults. In Journal of Structural Geology (Vol. 10, Issue 2, p. 183). Elsevier BV. https://doi.org/10.1016/0191-8141(88)90115-0

34. Farias, F., Szatmári, P., Bahniuk, A. M., & França, A. B. (2019). Evaporitic carbonates in the pre-salt of Santos Basin – Genesis and tectonic implications. In Marine and Petroleum Geology (Vol. 105, p. 251). Elsevier BV. https://doi.org/10.1016/j.marpetgeo.2019.04.020

35. Fernandes, L. A. F.; Santos, F. A. M. Bacias de Santos e de Campos: estratigrafia, estrutura e evolução. In: ARAÚJO, D. F.; HIRSCH, F. R.; VIANNA, R. H. M. (Org.). Geologia do Brasil. Brasília, DF: CPRM, 2017. p. 377-394.

36. Fernández-Ibáñez, F., Nolting, A., Breithaupt, C., Darby, B. J., Mimoun, J. G., & Henares, S. (2022). The properties of faults in the Brazil pre-salt: A reservoir characterization perspective. In Marine and Petroleum Geology (Vol. 146, p. 105955). Elsevier BV. https://doi.org/10.1016/j.marpetgeo.2022.105955

37. Ferrill, D. A., Stamatakos, J., & Sims, D. W. (1999). Normal fault corrugation: implications for growth and seismicity of active normal faults. In Journal of Structural Geology (Vol. 21, Issue 8, p. 1027). Elsevier BV. https://doi.org/10.1016/s0191-8141(99)00017-6

38. Fossen, H., Johansen, T. E. S., Hesthammer, J., & Rotevatn, A. (2005). Fault interaction in porous sandstone and implications for reservoir management; examples from southern Utah. In AAPG Bulletin (Vol. 89, Issue 12, p. 1593). American Association of Petroleum Geologists. https://doi.org/10.1306/07290505041

39. Fossen, H. (2010). Faults. In Cambridge University Press eBooks (p. 151). Cambridge University Press. https://doi.org/10.1017/cbo9780511777806.010

40. Fossen, H., & Rotevatn, A. (2015). Fault linkage and relay structures in extensional settings—A review. In Earth-Science Reviews (Vol. 154, p. 14). Elsevier BV. https://doi.org/10.1016/j.earscirev.2015.11.014

41. Fossen, H. (2020). Fault classification, fault growth and displacement. In Elsevier eBooks (p. 119). Elsevier BV. https://doi.org/10.1016/b978-0-444-64134-2.00007-9

42. Gardner, G. H. F.; Gardner, L. W.; Gregory, A. R.. Formation velocity and density – The diagnostic basics for stratigraphic traps. **Geophysics**, [S.L.], v. 39, n. 6, p. 770-780, dez. 1974. Society of Exploration Geophysicists. http://dx.doi.org/10.1190/1.1440465.

43. Garcia, S., Letouzey, J., Rudkiewicz, J. L., Danderfer, A., & Lamotte, D. F. de. (2011). Structural Modeling of Salt Tectonics in Central Portion of Santos Basin, Brazil. In Proceedings. https://doi.org/10.3997/2214-4609.20149110

44. Geng, C., Tong, H., Yu-dan, H., & Chunguang, W. (2007). Sandbox modeling of the fault-increment pattern in extensional basins. In Petroleum Science (Vol. 4, Issue 2, p. 29). Elsevier BV. https://doi.org/10.1007/bf03187438

45. Gomes, J. P., Bunevich, R. B., Tedeschi, L. R., Tucker, M. E., & Whitaker, F. F. (2020). Facies classification and patterns of lacustrine carbonate deposition of the Barra Velha Formation, Santos Basin, Brazilian Pre-salt. *Marine and petroleum geology*, *113*, 104176.

46. Guardado, L. R., Gamboa, L. A. P., & Lucchesi, C. F. (1989). Petroleum geology of the Campos Basin Brazil, a model for a producing Atlantic type Basin.

47. Guardiano, F.B., Srivastava, R.M. (1993). Multivariate Geostatistics: Beyond Bivariate Moments. In: Soares, A. (eds) Geostatistics Tróia '92. Quantitative Geology and Geostatistics, vol 5. Springer, Dordrecht. https://doi.org/10.1007/978-94-011-1739-5_12

48. Gudmundsson, Agust; Guidi, Giorgio de; Scudero, Salvatore. Length–displacement scaling and fault growth. **Tectonophysics**, [S.L.], v. 608, p. 1298-1309, nov. 2013. Elsevier BV. http://dx.doi.org/10.1016/j.tecto.2013.06.012.

49. Hansen, D. M. (2006). The morphology of intrusion-related vent structures and their implications for constraining the timing of intrusive events along the NE Atlantic margin. In Journal of the Geological Society (Vol. 163, Issue 5, p. 789). Geological Society of London. https://doi.org/10.1144/0016-76492004-167

50. Henaish, A., & Attwa, M. (2018). Internal structural architecture of a soft-linkage transfer zone using outcrop and DC resistivity data: Implications for preliminary engineering assessment. In Engineering Geology (Vol. 244, p. 1). Elsevier BV. https://doi.org/10.1016/j.enggeo.2018.07.018

51. Hill, A. C.; Thomas, G. W.. A New Approach for Simulating Complex Fractured Reservoirs. **Middle East Oil Technical Conference And Exhibition**, [S.L.], p. 0-50, 11 mar. 1985. SPE. http://dx.doi.org/10.2118/13537-ms.

52. Hoffman, K. S., Neave, J. W., & Nilsen, E. H. (2008). Building a Reservoir Model with Problematic Faults. In All Days. https://doi.org/10.2118/110367-ms

53. Hong, L., Yu, H., Cao, N., Tian, H., & Cheng, S. (2020). Applications of Artificial Intelligence in Oil and Gas Development. In Archives of Computational Methods in Engineering (Vol. 28, Issue 3, p. 937). Springer Science+Business Media. https://doi.org/10.1007/s11831-020-09402-8

54. Jahns, H.O. (1966) A Rapid Method for Obtaining a Two-Dimensional Reservoir Description from Well Pressure Response Data. Society of Petroleum Engineers Journal, 6, 315-327. http://dx.doi.org/10.2118/1473-PA

55. Jing, Lanru; Stephansson, Ove. Discrete Fracture Network (DFN) Method. **Developments In Geotechnical Engineering**, [S.L.], p. 365-398, 2007. Elsevier. http://dx.doi.org/10.1016/s0165-1250(07)85010-3.

56. Karam, M., Porto, R., & Saito, M. (2007). Tenth International Congress of the Brazilian Geophysical Society Seismic Stratigraphy of Pre-Salt in the Southernmost of Santos Basin (p. 426). https://doi.org/10.1190/sbgf2007-085

57. Karatalov, N. ., Stefaniak, A., & Vaughan, L. (2017). DFN Modeling Aided Reservoir Characterization. In Day 3 Wed, November 17, 2021. https://doi.org/10.2118/188641-ms

58. Karner, G. D., & Gamboa, L. A. P. (2007). Timing and origin of the South Atlantic pre-salt sag basins and their capping evaporites. In Geological Society London Special Publications (Vol. 285, Issue 1, p. 15). Geological Society of London. https://doi.org/10.1144/sp285.2

59. Kelly, P., Peacock, D., Sanderson, D. J., & MCGURK, A. C. (1999). Selective reverse-reactivation of normal faults, and deformation around reverse-reactivated faults in the Mesozoic of the Somerset coast. In Journal of Structural Geology (Vol. 21, Issue 5, p. 493). Elsevier BV. https://doi.org/10.1016/s0191-8141(99)00041-3

60. Kiang, C. H., Kowsmann, R. O., Figueiredo, A. M. F. de, & Bender, A. (1992). Tectonics and stratigraphy of the East Brazil Rift system: an overview. In Tectonophysics (Vol. 213, p. 97). Elsevier BV. https://doi.org/10.1016/0040-1951(92)90253-3

61. Kim, Y., & Sanderson, D. J. (2004). The relationship between displacement and length of faults: a review [Review of The relationship between displacement and length of faults: a review]. Earth-Science Reviews, 68(3), 317. Elsevier BV. https://doi.org/10.1016/j.earscirev.2004.06.003

62. Kim, Y., Peacock, D., & Sanderson, D. J. (2003). Fault damage zones. In Journal of Structural Geology (Vol. 26, Issue 3, p. 503). Elsevier BV. https://doi.org/10.1016/j.jsg.2003.08.002

63. Kompanik, G. S., HEIL, R., Al-Shammari, Z. A., & Al-Shammery, M. J. (1993). Geologic Modelling for Reservoir Simulation: Hanifa Reservoir, Berri Field, Saudi Arabia. In Middle East Oil Show. https://doi.org/10.2118/25580-ms

64. Krige, D.G. (1951) A Statistical Approaches to Some Basic Mine Valuation Problems on the Witwatersrand. Journal of the Chemical, Metallurgical and Mining Society of South Africa, 52, 119-139.

65. Kuang, L., Liu, H., Ren, Y., Luo, K., Shi, M., Su, J., & Li, X. (2021). Application and development trend of artificial intelligence in petroleum exploration and development. In Petroleum Exploration and Development (Vol. 48, Issue 1, p. 1). Elsevier BV. https://doi.org/10.1016/s1876-3804(21)60001-0.

66. Lee, Jeongwoo; Choi, Sung-Uk; Cho, Woncheol. A comparative study of dual-porosity model and discrete fracture network model. **Ksce Journal Of Civil Engineering**, [S.L.], v. 3, n. 2, p. 171-180, jun. 1999. Elsevier BV. http://dx.doi.org/10.1007/bf02829057.

67. Li, J. X., Zhang, T., Zhu, Y., & Chen, Z. (2024). Artificial General Intelligence (AGI) for the oil and gas industry: a review [Review of Artificial General Intelligence (AGI) for the oil and gas industry: a review]. arXiv (Cornell University). Cornell University. https://doi.org/10.48550/arXiv.2406.

68. Lima, B. E. M., Tedeschi, L., Pestilho, A. L. S., Santos, R. V., Vazquez, J. C., Guzzo, J. V. P., & Ros, L. F. D. (2019). Deep-burial hydrothermal alteration of the Pre-Salt carbonate reservoirs from northern Campos Basin, offshore Brazil: Evidence from petrography, fluid inclusions, Sr, C and O isotopes. In Marine and Petroleum Geology (Vol. 113, p. 104143). Elsevier BV. https://doi.org/10.1016/j.marpetgeo.2019.104143

69. Lima, A. de, Fourno, A., Nøetinger, B., & Schiozer, D. J. (2019). Characterization and Modeling of the Fault Network of a Brazilian Pre-Salt Reservoir and Upscaling Results. In SPE Annual Technical Conference and Exhibition. https://doi.org/10.2118/195999-ms

70. Lindseth, R. O.. Synthetic sonic logs—a process for stratigraphic interpretation. **Geophysics**, [S.L.], v. 44, n. 1, p. 3-26, jan. 1979. Society of Exploration Geophysicists. http://dx.doi.org/10.1190/1.1440922.

71. Magnavita, L. P. (coord.). Arcabouço tectônico e cinemática do pré-sal do sudeste brasileiro. PETROBRAS, E&P--EXP, Rio de Janeiro, 2010a, 161 p

72. Manighetti, I., King, G. C. P., Gaudemer, Y., Scholz, C. H., & Doubre, C. (2001). Slip accumulation and lateral propagation of active normal faults in Afar. In Journal of Geophysical Research Atmospheres (Vol. 106, p. 13667). American Geophysical Union. https://doi.org/10.1029/2000jb900471

73. Maschio, C., & Schiozer, D. J. (2003). A new upscaling technique based on Dykstra–Parsons coefficient: evaluation with streamline reservoir simulation. In Journal of Petroleum Science and Engineering (Vol. 40, p. 27). Elsevier BV. https://doi.org/10.1016/s0920-4105(03)00060-3

74. Matheron, G. (1963). Principles of geostatistics. *Economic Geology*, *58*(8), 1246–1266. https://doi.org/10.2113/GSECONGEO.58.8.1246

75. Matos, R. M. D. de, Fernandes, F., Norton, I. O., & Fetter, M. (2021). Oblique Core-Complex Type Detachment Systems in the Santos Basin. In SSRN Electronic Journal. RELX Group (Netherlands). https://doi.org/10.2139/ssrn.3985363

76. Mattos, N. H., & Alves, T. M. (2018). Corridors of crestal and radial faults linking salt diapirs in the Espírito Santo Basin, SE Brazil. In Tectonophysics (Vol. 728, p. 55). Elsevier BV. https://doi.org/10.1016/j.tecto.2017.12.025

77. Mendes, L. de C., Correia, U. M. da C., Cunha, O. R., Oliveira, F. M., & Vidal, A. C. (2022). Topological analysis of fault network in naturally fractured reservoirs: A case study from the pre-salt section of the Santos Basin, Brazil. In Journal of Structural Geology (Vol. 159, p. 104597). Elsevier BV. https://doi.org/10.1016/j.jsg.2022.104597

78. Minzoni, M., Cantelli, A., Thornton, J. A., & Wignall, B. (2020). Seismic-scale geometries and sequence-stratigraphic architecture of Early Cretaceous syn-post rift carbonate systems, Presalt Section, Brazil. In Geological Society London Special Publications (Vol. 509, Issue 1, p. 105). Geological Society of London. https://doi.org/10.1144/sp509-2019-78

79. Mohriak, W. U., & Paula, O. B. de. (2005). Major Tectonic Features In The Southeastern Brazilian Margin (Vol. 65, p. 886). https://doi.org/10.1190/sbgf2005-177

80. Moreira, J., Madeira, C., Gil, J. A., & Machado, M. A. (2007). Bacia de Santos (Vol. 15, Issue 2, p. 531). https://bgp.petrobras.com.br/bgp/article/view/354/272

81. Moulin, M., Aslanian, D., Rabineau, M., Patriat, M., & Matias, L. (2012). Kinematic keys of the Santos–Namibe basins. In Geological Society London Special Publications (Vol. 369, Issue 1, p. 91). Geological Society of London. https://doi.org/10.1144/sp369.3

82. Moustafa, A. R., & Khalil, S. (2016). Control of compressional transfer zones on syntectonic and post-tectonic sedimentation: implications for hydrocarbon exploration. In Journal of the

Geological Society (Vol. 174, Issue 2, p. 336). Geological Society of London. https://doi.org/10.1144/jgs2016-030

83. Naliboff, J., Buiter, S., Péron-Pinvidic, G., Osmundsen, P. T., & Tetreault, J. (2017). Complex fault interaction controls continental rifting. In Nature Communications (Vol. 8, Issue 1). Nature Portfolio. https://doi.org/10.1038/s41467-017-00904-x

84. Neves, I. de A., Lupinacci, W. M., Ferreira, D. J. A., Zambrini, J. P. R., Oliveira, L. O. A., Azul, M. O., Ferrari, A. L., & Gambôa, L. A. P. (2019). Presalt reservoirs of the Santos Basin: Cyclicity, electrofacies, and tectonic-sedimentary evolution. In Interpretation (Vol. 7, Issue 4). Society of Exploration Geophysicists. https://doi.org/10.1190/int-2018-0237.1

85. Nicol, A., Walsh, J. J., Villamor, P., Seebeck, H., & Berryman, K. (2010). Normal fault interactions, paleoearthquakes and growth in an active rift. In Journal of Structural Geology (Vol. 32, Issue 8, p. 1101). Elsevier BV. https://doi.org/10.1016/j.jsg.2010.06.018

86. Nixon, C. W., Sanderson, D. J., Dee, S. J., Bull, J. M., Humphreys, R. J., & Swanson, M. H. (2014). Fault interactions and reactivation within a normal-fault network at Milne Point, Alaska. In AAPG Bulletin (Vol. 98, Issue 10, p. 2081). American Association of Petroleum Geologists. https://doi.org/10.1306/04301413177

87. Nixon, C. W., Nærland, K., Rotevatn, A., Dimmen, V., Sanderson, D. J., & Kristensen, T. B. (2020). Connectivity and network development of carbonate-hosted fault damage zones from western Malta. In Journal of Structural Geology (Vol. 141, p. 104212). Elsevier BV. https://doi.org/10.1016/j.jsg.2020.104212

88. Nunna, K. C., & King, M. J. (2017). Dynamic Downscaling and Upscaling in High Contrast Systems. In SPE Reservoir Simulation Conference. https://doi.org/10.2118/182689-ms

89. Nyberg, B., Nixon, C. W., & Sanderson, D. J. (2018). NetworkGT: A GIS tool for geometric and topological analysis of two-dimensional fracture networks. In Geosphere (Vol. 14, Issue 4, p. 1618). Geological Society of America. https://doi.org/10.1130/ges01595.1

90. Oliveira, L. C. de, Rancan, C. C., Sartorato, A. C. L., Farias, F., & Pereira, E. (2021). Drowning unconformities on presalt carbonate platforms – Examples from the Itapema Formation (Lower Cretaceous), Santos Basin, offshore Brazil. In Palaeogeography Palaeoclimatology Palaeoecology (Vol. 577, p. 110570). Elsevier BV. https://doi.org/10.1016/j.palaeo.2021.110570

91. Omosanya, K. O., Eruteya, O. E., Siregar, E. S. A., Zięba, K. J., Johansen, S. E., Alves, T. M., & Waldmann, N. (2018). Three-dimensional (3-D) seismic imaging of conduits and radial faults associated with hydrothermal vent complexes (Vøring Basin, Offshore Norway). In Marine Geology (Vol. 399, p. 115). Elsevier BV. https://doi.org/10.1016/j.margeo.2018.02.007

92. OpendTect. (2015). https://github.com/OpendTect/OpendTect

93. Peacock, D., & Sanderson, D. J. (1991). Displacements, segment linkage and relay ramps in normal fault zones. In Journal of Structural Geology (Vol. 13, Issue 6, p. 721). Elsevier BV. https://doi.org/10.1016/0191-8141(91)90033-f

94. Peacock, D., & Sanderson, D. J. (1994). Geometry and Development of Relay Ramps in Normal Fault Systems. In AAPG Bulletin (Vol. 78). American Association of Petroleum Geologists. https://doi.org/10.1306/bdff9046-1718-11d7-8645000102c1865d

95. Peacock, D., Knipe, R. J., & Sanderson, D. J. (2000). Glossary of normal faults. In Journal of Structural Geology (Vol. 22, Issue 3, p. 291). Elsevier BV. https://doi.org/10.1016/s0191-8141(00)80102-9

96. Peacock, D. (2002). Propagation, interaction and linkage in normal fault systems. In Earth-Science Reviews (Vol. 58, Issue 1, p. 121). Elsevier BV. https://doi.org/10.1016/s0012-8252(01)00085-x

97. Peacock, D., Nixon, C. W., Rotevatn, A., Sanderson, D. J., & Zuluaga, L. F. (2016). Glossary of fault and other fracture networks. In Journal of Structural Geology (Vol. 92, p. 12). Elsevier BV. https://doi.org/10.1016/j.jsg.2016.09.008

98. Peacock, D., Dimmen, V., Rotevatn, A., & Sanderson, D. J. (2017). A broader classification of damage zones. In Journal of Structural Geology (Vol. 102, p. 179). Elsevier BV. https://doi.org/10.1016/j.jsg.2017.08.004

99. Péron-Pinvidic, G., & Manatschal, G. (2019). Rifted Margins: State of the Art and Future Challenges. In Frontiers in Earth Science (Vol. 7). Frontiers Media. https://doi.org/10.3389/feart.2019.00218

100. Perrin, C., Manighetti, I., & Gaudemer, Y. (2015). Off-fault tip splay networks: A genetic and generic property of faults indicative of their long-term propagation. In Comptes

Rendus Géoscience (Vol. 348, Issue 1, p. 52). Elsevier BV. https://doi.org/10.1016/j.crte.2015.05.002

101. Pietzsch, R., Oliveira, D. M. de, Tedeschi, L., Neto, J. V. Q., Figueiredo, M. F., Vazquez, J. C., & Souza, R. S. (2018). Palaeohydrology of the Lower Cretaceous pre-salt lacustrine system, from rift to post-rift phase, Santos Basin, Brazil. In Palaeogeography Palaeoclimatology Palaeoecology (Vol. 507, p. 60). Elsevier BV. https://doi.org/10.1016/j.palaeo.2018.06.043

102. Planke, S., Rasmussen, T. M., Rey, S., & Myklebust, R. (2005). Seismic characteristics and distribution of volcanic intrusions and hydrothermal vent complexes in the Vøring and Møre basins. In Geological Society London Petroleum Geology Conference series (Vol. 6, Issue 1, p. 833). Zoological Society of London. https://doi.org/10.1144/0060833

103. Pollard, David D.; Aydin, Atilla. Progress in understanding jointing over the past century. **Geological Society of America Bulletin**, v. 100, n. 8, p. 1181-1204, 1988.

104. Qi, D., & Hesketh, T. (2005). An Analysis of Upscaling Techniques for Reservoir Simulation. In Petroleum Science and Technology (Vol. 23, p. 827). Taylor & Francis. https://doi.org/10.1081/lft-200033132

105. Ren, K., Oliveira, M. J., Zhao, J., Zhao, J., Oliveira, L. C. de, Rancan, C. C., Carmo, I. O., & Deng, Q. (2019). Using Wireline Logging and Thin Sections to Identify Igneous Contact Metamorphism and Hydrothermal Influence on Presalt Limestone Reservoirs in Libra Block, Santos Basin. In Day 3 Wed, October 05, 2022. https://doi.org/10.4043/29818-ms

106. Renaut, R. W., & Tiercelin, J.-J. (1993). Lake Bogoria, Kenya: soda, hot springs and about a million flamingoes. In Geology Today (Vol. 9, Issue 2, p. 56). Wiley. https://doi.org/10.1111/j.1365-2451.1993.tb00981.x

107. Renaut, R. W., Owen, R. B., Jones, B., Tiercelin, J.-J., Tarits, C., Ego, J. K., & Konhauser, K. O. (2012). Impact of lake-level changes on the formation of thermogene travertine in continental rifts: Evidence from Lake Bogoria, Kenya Rift Valley. In Sedimentology (Vol. 60, Issue 2, p. 428). Wiley. https://doi.org/10.1111/j.1365-3091.2012.01347.x

108. Richard, P., Pattnaik, C., Ajmi, N. . A., Kidambi, V. K., Narhari, R. ., LeVarlet, X. ., Guit, F., & Dashti, Q. (2015). Detailed Discrete Fracture Network in Support of Drilling

Activities in North Kuwait Carbonate Reservoirs. In Day 4 Thu, November 18, 2021. https://doi.org/10.2118/177766-ms

109. Rigoti, C. A. (2015). Tectonic Evolution of Santos Basin with emphasis on crustal geometry: Integrated interpretation of seismic reflection and refraction, gravity and magnetic data (p. 0). http://www.bdtd.uerj.br/handle/1/7131

110. Ringrose, Philip; Bentley, Mark. Reservoir Model Design: a practitioner′s guide. **Springer**, [S.L.], v. 2, p. 1-333, 2021. Springer International Publishing. http://dx.doi.org/10.1007/978-3-030-70163-5.

111. Rodriguez, C., Jackson, C., Bell, R., Rotevatn, A., & Francis, M. (2021). Deep-water reservoir distribution on a salt-influenced slope, Santos Basin, offshore Brazil. In AAPG Bulletin (Vol. 105, Issue 8, p. 1679). American Association of Petroleum Geologists. https://doi.org/10.1306/11182017340

112. Rowan, M. G., Muñoz, J. A., Giles, K. A., Roca, E., Hearon, T. E., Fiduk, J. C., Ferrer, O., & Fischer, M. P. (2020). Folding and fracturing of rocks adjacent to salt diapirs. In Journal of Structural Geology (Vol. 141, p. 104187). Elsevier BV. https://doi.org/10.1016/j.jsg.2020.104187

113. Sanderson, D. J., & Nixon, C. W. (2015). The use of topology in fracture network characterization. In Journal of Structural Geology (Vol. 72, p. 55). Elsevier BV. https://doi.org/10.1016/j.jsg.2015.01.005

114. Sanderson, D. J., & Nixon, C. W. (2018). Topology, connectivity and percolation in fracture networks. In Journal of Structural Geology (Vol. 115, p. 167). Elsevier BV. https://doi.org/10.1016/j.jsg.2018.07.011

115. Santos, A., Scanavini, H. F. Á., Pedrini, H., Schiozer, D. J., Munerato, F. P., & Barreto, C. E. A. G. (2022). An artificial intelligence method for improving upscaling in complex reservoirs. In Journal of Petroleum Science and Engineering (Vol. 211, p. 110071). Elsevier BV. https://doi.org/10.1016/j.petrol.2021.110071

116. Schlische, R. W., & Withjack, M. O. (2008). Origin of fault domains and fault-domain boundaries (transfer zones and accommodation zones) in extensional provinces: Result of random nucleation and self-organized fault growth. In Journal of Structural Geology (Vol. 31, Issue 9, p. 910). Elsevier BV. https://doi.org/10.1016/j.jsg.2008.09.005

117. Scholz, C. H., Ando, R., & Shaw, B. E. (2009). The mechanics of first order splay faulting: The strike-slip case. In Journal of Structural Geology (Vol. 32, Issue 1, p. 118). Elsevier BV. https://doi.org/10.1016/j.jsg.2009.10.007

118. Scholz, C. H. (2011). First-order splay faults: dip-slip examples. In Geological Society London Special Publications (Vol. 359, Issue 1, p. 313). Geological Society of London. https://doi.org/10.1144/sp359.17

119. Seismic Interpretation Solutions. (2024). https://www.eliis-geo.com/

120. Siqueira, Raissa; Fetter, Marcos; Cetale, Marco. Structural geology and deformation analysis in the Búzios-Itapu area, Santos Basin — offshore Brazil. **Journal Of South American Earth Sciences**, [S.L.], v. 134, p. 104779, fev. 2024. Elsevier BV. http://dx.doi.org/10.1016/j.jsames.2024.104779.

121. Soliva, R., & Benedicto, A. (2004). A linkage criterion for segmented normal faults. In Journal of Structural Geology (Vol. 26, Issue 12, p. 2251). Elsevier BV. https://doi.org/10.1016/j.jsg.2004.06.008

122. Souza, I. (2008). Falhas de transferência da porção norte da Bacia de Santos interpretadas a partir de dados sísmicos: sua influência na evolução e deformação da bacia. (p. 0). http://repositorio.unesp.br/handle/11449/102986

123. Stanton, N., Ponte-Neto, C. F., Bijani, R., Masini, E., Fontes, S. L., & Flexor, J. M. (2014). A geophysical view of the Southeastern Brazilian margin at Santos Basin: Insights into rifting evolution. In Journal of South American Earth Sciences (Vol. 55, p. 141). Elsevier BV. https://doi.org/10.1016/j.jsames.2014.07.003

124. Surguchev, L. M., Золотухин, А. Б., & Bratvold, R. B. (1992). Reservoir Characterization and Modeling Supported by Expert Knowledge Systems. https://doi.org/10.2523/24279-ms

125. Szatmári, P., & Milani, E. J. (2016). Tectonic control of the oil-rich large igneous-carbonate-salt province of the South Atlantic rift. In Marine and Petroleum Geology (Vol. 77, p. 567). Elsevier BV. https://doi.org/10.1016/j.marpetgeo.2016.06.004

126. Tang, M., Liu, Y., & Durlofsky, L. J. (2020). A deep-learning-based surrogate model for data assimilation in dynamic subsurface flow problems. In Journal of Computational Physics (Vol. 413, p. 109456). Elsevier BV. https://doi.org/10.1016/j.jcp.2020.109456

127. Tariq, M., Bizarro, P., Sousa, A. de, & Ribeiro, M. T. (2012). Reservoir Characterization and Modeling of a Carbonate Reservoir - Case Study. In Abu Dhabi International Petroleum Conference and Exhibition. https://doi.org/10.2118/161039-ms

128. Tariq, Z., Aljawad, M. S., Hasan, A., Murtaza, M., Mohammed, E. A., El-Husseiny, A., Alarifi, S. A., Mahmoud, M., & Abdulraheem, A. (2021). A systematic review of data science and machine learning applications to the oil and gas industry [Review of A systematic review of data science and machine learning applications to the oil and gas industry]. Journal of Petroleum Exploration and Production Technology, 11(12), 4339. Springer Nature. https://doi.org/10.1007/s13202-021-01302-2

129. Torabi, A., Alaei, B., & Libak, A. (2018). Normal fault 3D geometry and displacement revisited: Insights from faults in the Norwegian Barents Sea. In Marine and Petroleum Geology (Vol. 99, p. 135). Elsevier BV. https://doi.org/10.1016/j.marpetgeo.2018.09.032

130. Torsvik, T. H., Rousse, S., Labails, C., & Smethurst, M. A. (2009). A new scheme for the opening of the South Atlantic Ocean and the dissection of an Aptian salt basin. In Geophysical Journal International (Vol. 177, Issue 3, p. 1315). Oxford University Press. https://doi.org/10.1111/j.1365-246x.2009.04137.x

131. Treffeisen, T., & Henk, A. (2019). Representation of faults in reservoir-scale geomechanical finite element models – A comparison of different modelling approaches. In Journal of Structural Geology (Vol. 131, p. 103931). Elsevier BV. https://doi.org/10.1016/j.jsg.2019.103931

132. Trudgill, B. D., & Cartwright, J. A. (1994). Relay-ramp forms and normal-fault linkages, Canyonlands National Park, Utah. In Geological Society of America Bulletin (Vol. 106, Issue 9, p. 1143). Geological Society of America. https://doi.org/10.1130/0016-7606(1994)106<1143:rrfanf>2.3.co;2

133. Taner, M. T., Sheriff, R. E. 1977. Application of Amplitude, Frequency, and Other Attributes to Stratigraphic and Hydrocarbon Determination, Seismic Stratigraphy — Applications to Hydrocarbon Exploration, Charles E. Payton. https://doi.org/10.1306/M26490C17

134. Twiss, Robert J.; Moores, Eldridge M. *Structural geology*. Ilustrada, reimpressão. New York: W. H. Freeman, 1992. 532 p. ISBN 9780716722526.

135. Vital, J. C. dos S., Ade, M. V. B., Morelatto, R., & Lupinacci, W. M. (2023). Compartmentalization and stratigraphic-structural trapping in pre-salt carbonate reservoirs of the Santos Basin: A case study in the Iara complex. In Marine and Petroleum Geology (Vol. 151, p. 106163). Elsevier BV. https://doi.org/10.1016/j.marpetgeo.2023.106163

136. Wadsley, W. A. Modelling reservoir geometry with non-rectangular coordinate grids. In: **SPE Annual Technical Conference and Exhibition?**. SPE, 1980. p. SPE-9369-MS.

137. Walsh, J. J., Bailey, W. R., Childs, C., Nicol, A., & Bonson, C. G. (2003). Formation of segmented normal faults: a 3-D perspective. In Journal of Structural Geology (Vol. 25, Issue 8, p. 1251). Elsevier BV. https://doi.org/10.1016/s0191-8141(02)00161-x

138. Wibberley, C., Yielding, G., & Toro, G. D. (2008). Recent advances in the understanding of fault zone internal structure: a review [Review of Recent advances in the understanding of fault zone internal structure: a review]. Geological Society London Special Publications, 299(1), 5. Geological Society of London. https://doi.org/10.1144/sp299.2

139. Wibberley, C., & Shipton, Z. K. (2010). Fault zones: A complex issue. In Journal of Structural Geology (Vol. 32, Issue 11, p. 1554). Elsevier BV. https://doi.org/10.1016/j.jsg.2010.10.006

140. Williams, B., & Hubbard, R. J. (1984). Seismic stratigraphic framework and depositional sequences in the Santos Basin, Brazil. In Marine and Petroleum Geology (Vol. 1, Issue 2, p. 90). Elsevier BV. https://doi.org/10.1016/0264-8172(84)90079-5

141. Wright, V. P., & Barnett, A. J. (2020). The textural evolution and ghost matrices of the Cretaceous Barra Velha Formation carbonates from the Santos Basin, offshore Brazil. *Facies*, *66*(1), 7.

142. Yang, A., & Eacmen, J. C. (2003). Fault Identification and Modeling for Production Enhancement. In All Days. https://doi.org/10.2118/83495-ms

143. Zhang, P., Pickup, G. E., & Christie, M. A. (2005). A New Upscaling Approach for Highly Heterogeneous Reservoirs. In All Days. https://doi.org/10.2118/93339-ms

144. Zwaan, F., & Schreurs, G. (2017). How oblique extension and structural inheritance influence rift segment interaction: Insights from 4D analog models. In Interpretation (Vol. 5, Issue 1). Society of Exploration Geophysicists. https://doi.org/10.1190/int-2016-0063.1